Techniques for Quantum Simulation with Ultracold Gases, Paraxial Optics and Electric Circuits

by

Christopher Oliver

A thesis submitted to the
University of Birmingham
for the degree of
DOCTOR OF PHILOSOPHY

School of Physics and Astronomy
College of Engineering and Physical Sciences
University of Birmingham
September 2, 2023

ABSTRACT

Quantum simulation refers to the use of controllable physical systems to simulate quantum mechanical models. Since the concept was proposed in the early 1980s, quantum simulation has grown into a major field, with important applications both within physics and in the wider world. In this thesis, we present three works of quantum simulation. Firstly, in an ultracold atom setting, we present the experimental realisation of a synthetic dimension formed from the energy eigenstates of a harmonic trap when the system is driven with a time-periodic potential. We characterise the scheme using Bloch oscillations of the cloud up-and-down the ladder of trap states, and demonstrate a long synthetic dimension of several tens of sites. Secondly, we theoretically propose the use of the temporal dynamics of an optical pulse in a 1D array of waveguides to engineer quantum Hall physics. We show that the photonic band structure of a realistic model of a waveguide array can be engineered to share some key features of a relevant quantum Hall model, and then highlight a number of specific effects that could be observed in experiment, namely a controllable optical delay and the steering of a wavepacket back-and-forth across the array. Finally, we propose the use of lattices formed from commercially-available coaxial cables as a quantum simulator. We calculate the dispersion of Bloch waves in a 2D brick wall lattice of identical cables and three-port connector elements, and show that we find dispersive bands that touch at Dirac points, and a flat band that is not isolated. The lower dispersive band is conical for small momenta, suggesting we are in the nearly-free-photon limit. We then show that we can control the location and gap of the Dirac points, suggesting connections with the theory of artificial magnetic fields in strained graphene. We

further show that we can introduce energetically-isolated flat bands. These works have many interesting future research directions, including the realisation of quantum Hall physics using our shaken trap synthetic dimension scheme; the investigation of the interplay between photon-photon interactions and topology using the optical pulse/waveguide array techniques, and the exploration of interacting physics in the coaxial cable lattice.

DEDICATION

To my biological and physics families

ACKNOWLEDGEMENTS

This PhD took $4\frac{1}{2}$ years, so that means that I have a lot of people to thank. My deepest thanks must, of course, go to my supervisor, Dr. Hannah Price, for her endless supply of time, advice on all things physics and academia and fascinating physical insight. I am incredibly grateful also to Iacopo Carusotto and everybody at my second home for physics, Trento, for the hospitality during my visit and exposure to both some fun new ideas and the beautiful Italian mountains. None of the work would have been possible without everybody I have collaborated with, so thank you to Aaron Smith, Denis Nabari, Giovanni Barontini, Grazia Salerno, Leo Ricci, Mikael Rechtsman, Nathan Goldman, Seba Mukherjee, Tom Easton and Vera Guarrera. I also wish to acknowledge the Royal Society for funding this work, particularly the generous funding for conferences and summer schools. This is also a good moment to thank all my other physics friends far and wide, especially Gerard Valentí i Rojas and Luke Fernley.

Returning to Birmingham, I am deeply grateful to everybody in the Birmingham Theory Group for providing such a wonderful, stimulating and fun environment to do physics. I particularly want to highlight PhD Office Number 1 for some of the best times of my life, and all your friendship and support over the years. This will be a long list, but thank you to Ben McCanna, Carlos Borges Camacho, David Reid (Chris v 2.0), Dave Perkins, Dylan Edwards, Enrico Martello, Ewan McCulloch, Gabriele Pinna, George McArdle, Jacob Spink, James Pallister, Joe Jones, Kerr Maxwell, Lewis Madden, Manny Kainth, Michael Clark, Rob Stanyon, Rory Whelan, Rose Davies, Tim Denys, Tom Young and Yasser Bezzaz. Thanks also to all the staff in the group for teaching me so much,

right from the start of my undergraduate days to now.

Moving down one floor, I want to thank all the staff in the Birmingham Nuclear Physics Group and the students in PhD Office Number 2. I am particularly grateful to Angus Hollands, Ellie Rowe, Mark Griffiths, Ross Allen, Stephen Maple, Stuart Pirrie and Suzie Freer for all your friendship and support, both during the PhD and in the future.

I am deeply thankful for the enduring support from Alex Coates, Beckie Trinder, Eloïse Brown, Emily Aveyard, Harriet Snell, Kristian Zarębski, Lorena Vineusa, Miles Toon, Nathan Adams, Peter Carpenter and Rhiann Canavan right from the start of my physics career and throughout. Thank you also to all my other friends from Birmingham, particularly Juraj and family, and my running, climbing and cycling friends for giving my something physics-orthogonal to keep me going. And, of course, none of this would have been possible without the endless love and support of my family, so ppecial thanks go to them and to Beckie Trinder (again) for being there for me, particularly during the ups and downs of the pandemic.

Last but not least, thank you to all of my teaching and outreach colleagues for making my PhD experience a full one, and to several people already mentioned for the porofreading.

CONTENTS

OVERVIEW OF THESIS STRUCTURE

This thesis is comprised of five chapters covering three pieces of work in the field of quantum simulation, with Chapters 2 and 3 being manuscripts ready for publication, and Chapter 4 reporting on some recently completed work. As the first author on both manuscripts, I performed all analytical and numerical calculations, and some data analysis in Chapter 2. I was also responsible for the majority of the writing in each manuscript. My supervisor, Dr. Hannah Price, advised on the direction of the projects and assisted with the writing and editing. Other co-authors on the papers were responsible for experimental work, advice on the project direction and some writing and editing. More precisely:

- Chapter 1 is a review of the field of quantum simulation, with a particular focus on the physics of 2D topological systems

- Chapter 2 consists of the manuscript: C. Oliver et al, "Artificial gauge fields in the t-z mapping for optical pulses: spatiotemporal wavepacket control and quantum Hall physics", In preparation (2023), and additional introductory material relevant to the experimental platform considered there

- Chapter 3 consists of the manuscript: C. Oliver et al, "Bloch Oscillations Along a Synthetic Dimension of Atomic Trap States", In: arXiv:2112.10648 [cond-mat.quant-gas] (2021), and additional introductory material relevant to the experimental platform considered there

- Chapter 4 is a reports on recent results in the third project in this thesis

- Chapter 5 is a conclusion summarising the work and future research directions.

CHAPTER 1

INTRODUCTION

Quantum simulation refers to the use of controllable physical systems to simulate quantum mechanical models [1]. We begin this introduction by reviewing this approach to quantum mechanics, and we then focus on the essential physics of topological systems, which are a class of system particularly well-suited to quantum simulation. In this thesis, we present three different examples of quantum simulation in three different experimental platforms. Each chapter contains additional introductory material that is specific to each platform. Note also that Chapters 2 and 3 are comprised of two scientific paper manuscripts, and, as such, there is introductory material to be found there too.

1.1 Introduction to Quantum Simulation

In general, quantum mechanical systems are extremely difficult to simulate on a classical computer, owing to the fact that the number of parameters needed to describe a state or operator grows exponentially with the number of degrees of freedom. This difficulty therefore limits our ability to study quantum mechanical systems theoretically. These exponentially-growing resource requirements can be circumvented by instead using a quantum computer, in which the elements comprising the machine are themselves quantum mechanical. A comparatively small number of resources can therefore be used to represent an exponentially-scaling amount of information.

The above could be achieved by using a digital quantum computer [2], in which a set of qubits (two-level systems) can be prepared, evolved in time with a set of gates, and finally measured. Such a device can be shown to be universal [2], loosely meaning that it can be used to tackle a wide variety of problems. However, a major drawback of this approach is that an enormous number of qubits is required to build a machine that is fault-tolerant, meaning that the computation is robust against sources of errors in the experimental platform. Therefore, there has been great interest in the more achievable, shorter-term goal of analogue quantum simulation. Here, rather than using collections of qubits and gates, a suitably-controllable analogue system is chosen whose Hamiltonian can be engineered to correspond to that of some target model of interest. The behaviour of the target model can then be studied by experimentally preparing the quantum simulator in some chosen initial state, which is then evolved under the engineered Hamiltonian before being measured.

To illustrate this general concept, we highlight a particularly well-established and celebrated example of quantum simulation, namely ultracold atomic gases in optical lattices [3, 4]. Without detouring into a detailed discussion of the physics, the general approach is to cool an atomic gas (of either fermionic or bosonic species) to very low temperatures, allowing one to focus on the quantum properties of the system without thermodynamic effects washing them out. The ultracold gas is then loaded into an optical lattice which, in the most modern experiments, can be either 1D, 2D or 3D and of almost arbitrary geometry. Provided the lattice is sufficiently deep in energy, the gas is well-described by a tight-binding Hamiltonian over the lattice, whose hopping energy can be tuned in experiment, as can the interactions between the atoms. All-in-all, the system therefore realises the notoriously computationally-difficult Hubbard model, which is the paradigmatic model of many-body quantum physics [5]. The physics of the Hubbard model, such as its quantum phase diagram or the dynamics generated by its Hamiltonian, can therefore be probed in this well-controlled experimental setting. This is in stark contrast to electrons in a solid-state setting, where the control over the particle statis-

tics, lattice geometry, hopping energy and interactions are either limited or non-existent, and where potentially unwanted effects such as disorder cannot be easily removed where desired.

Apart from ultracold atomic gases in optical lattices, several other platforms have emerged as powerful approaches to quantum simulation [6]. The major examples are: arrays of trapped ions [7], optical tweezer arrays of Rydberg atoms [8]; ultracold molecules [9]; arrays of photonic cavities [10, 11]; superconducting circuits [12] and linear optical systems [13]. A major category of model that is often investigated with quantum simulation, including in some of this thesis, is topological systems. Therefore, we next review the relevant aspects of these systems, with a particular focus on 2D models and the quantum Hall effect. The following section draws heavily from [14].

1.2 Introduction to Topological Physics

Since their discovery in the 1980s [15], topological phases of matter have become a major field of physics [16, 17] due to their unusual properties in comparison to phases falling under the usual Ginzburg-Landau description, with some of these properties having important implications for applications, as indicated shortly.

Usually, phase transitions are described using Ginzburg-Landau theory [18]. In this formalism, we describe the system using a local order parameter, where the change to a non-zero value of this order parameter signals the onset of a phase transition. Topological phase transitions cannot be described in this way. Instead, they need a global order parameter which is integer-valued. This integer-valued property gives rise to 'topological protection'; the integer-valued order parameter cannot be changed without a drastic change to the system, such as a band gap closing, meaning that physical observables also cannot change easily. One unusual consequence of this topological protection in some systems is the existence of chiral edge states, which are localised on the system edges and propagate robustly in one direction without scattering from corners or defects. These

unusual features are a major focus of applied research in topological physics; chiral edge states suggest ready application anywhere that robust or one-way propagation is required, such as some photonic devices like optical isolators [19] and topological lasers [20, 21].

The role of topology in the above description of topological phases is not immediately clear. More explicitly, two phases are topologically equivalent if we can change between them in a continuous way, without closing a band gap. This is analogous to the intuitive explanation of topology in a mathematical setting; two surfaces are topologically equivalent if they can be continuously deformed into each other without cutting or tearing [22]. Different integer-valued topological invariants can then be defined, where two topologically-inequivalent surfaces have different values of the invariant. Analogously, the aforementioned integer-valued global order parameter plays the role of a topological invariant, distinguishing distinct topological phases.

A major class of topological systems are 2D models with broken time-reversal symmetry [16, 17]. The first topological systems that were discovered experimentally [15], namely quantum Hall systems in which the symmetry breaking is provided by a magnetic field, fall into this class and, as mentioned below, such systems are still at the forefront of research. Therefore, we next summarise the physics of the quantum Hall effect, with a particular focus on the non-interacting integer case, before connecting this physics with quantum simulation.

1.2.1 The Quantum Hall Effect

The integer quantum Hall effect was discovered in 1980 [15, 17, 23, 24], and won the Nobel Prize in 1985. It was originally discovered in a solid state setting, but analogous quantum Hall effects have since been studied in other systems, as discussed below. The experiment works as follows. A two-dimensional electron gas (i.e. assuming no electron-electron interactions) is cooled to a very low temperature and a strong magnetic field is applied perpendicular to the plane containing the gas. A current is then driven through the sample, and the resistivity is measured in the perpendicular in-plane direction. The

key findings are shown in Fig. 1.1, from which we can make a number of observations.

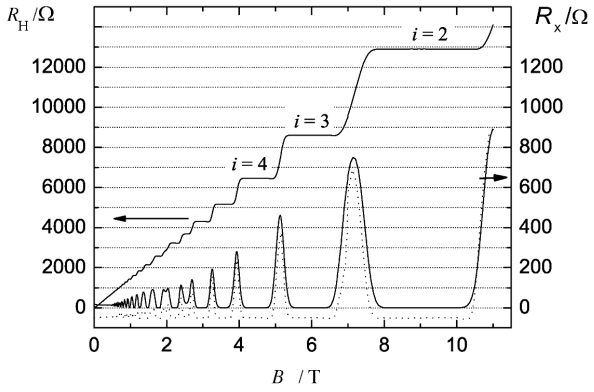

Figure 1.1: Plot showing a typical example of the integer quantum Hall effect measured in a solid state experiment. For small values of the magnetic field, the transverse resistance (upper line) is linear as expected in the classical Hall effect, and plateaus are visible in the quantum regime as the field is increased. Figure adapted from [25].

- For a small magnetic field, the resistivity becomes linear, as in the classical Hall effect.

- For a large magnetic field, we observe plateaus in the resistance. Their values are $\frac{h}{e}\frac{1}{\nu}$, where ν is an integer in the case of the integer quantum Hall effect. The case of ν being a rational fraction is the fractional quantum Hall effect, which is a very rich and complex problem that is associated with electron-electron interactions being strong.

- The quantisation effect is universal, and does not depend on the geometry, material type, disorder, etc. The physics displayed here is therefore very robust and can be measured with very high precision.

- Although disorder does not disrupt the quantisation, it does still have an important role to play. The length of the plateaus increases with increasing disorder, and in the limit of zero disorder, the resistivity is only quantised for specific values of the magnetic field.

The effect can be explained quantum mechanically using Landau levels. In short, these are the energy levels found when a charged quantum particle is subjected to a constant

perpendicular magnetic field. Roughly, the particle moves around in a cyclotron orbit as it would classically, but the particle's wave-like nature means that it interferes with itself when moving around the circle. Requiring constructive interference leads to quantised energy levels. The relation to the integer quantum Hall effect is that the filling of these Landau levels leads to quantised resistivity.

We can also understand some aspects of the integer quantum Hall effect using a simple semiclassical picture. Fig. 1.2 shows a semiclassical 'cartoon' of the motion we expect. In the bulk of the sample, far from any edges, the electrons move around in cyclotron orbits due to the magnetic field and do not carry any current (i.e. the bulk states have zero group velocity). The material is therefore an insulator in the bulk. Around the edges however, we see different behaviour. The electrons close to the edge cannot complete a full orbit because this would take them outside the sample. They instead elastically collide with the edge and reflect off, resulting in the chiral 'skipping' orbits shown in the figure. These are an example of the previously-mentioned chiral edge states that are found in many topological systems.

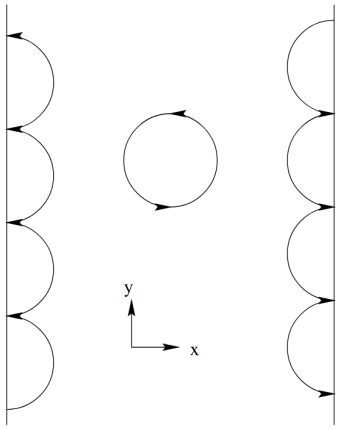

Figure 1.2: Sketch showing the semiclassical explanation of the integer quantum Hall effect. Electrons in the bulk move in cyclotron orbits and carry no current, whereas electrons at the system edge cannot complete a full orbit without leaving the system, so 'skip' along the edges. Figure adapted from [23].

Having outlined the phenomenology of the quantum Hall effect and given some intuition about its origin, we now explain the general formalism by which we describe topo-

logical phases in 2D, and illustrate how the integer quantum Hall effect can be explained topologically.

1.2.2 The Berry Phase, Berry Curvature, Chern Number and Integer Quantum Hall Effect

Ultimately, we want to talk about the aforementioned integer-valued global order parameter and show how it relates to observables in topological systems, such as those in the integer quantum Hall effect above. For 2D systems, this quantity is called the first Chern number. In order to get to this stage, we first need to define some related quantities. To be more precise, we are interested in the topological properties of Bloch bands in momentum space. As we will now show, we can describe the local geometrical properties of these bands using a pair of quantities, the Berry phase and Berry curvature [16, 17, 26]. These then lead us directly to the Chern number. The Berry phase and Berry curvature also have a structure that is deeply analogous with electromagnetism, which leads to a very elegant interpretation of the Chern number [17]. We therefore begin with a discussion of these two concepts. The argument in this section is based on that of [17].

The first quantity to define is the Berry phase. We consider the adiabatic time evolution of a quantum system. The time evolution comes from slowly varying a set of parameters $\mu = (\mu_1, \mu_2, ...)$ that the Hamiltonian H depends on. We can define the instantaneous eigenstates $|n(\mu)\rangle$ by

$$H(\mu)\,|n(\mu)\rangle = E_n(\mu)\,|n(\mu)\rangle\,, \tag{1.1}$$

with instantaneous eigenenergies $E_n(\mu)$. If we prepare the system in a state $|\psi_0\rangle = |n(\mu(0))\rangle$ and slowly vary the parameters, the system will remain in an eigenstate providing the evolution is sufficiently slow. This means that only the phase of the wavefunction $|\psi(t)\rangle = e^{-i\theta(t)}\,|n(\mu\rangle)$ can contain any details of the evolution. Substituting this into the

Schrödinger equation and integrating gives the phase θ as

$$\theta(t) = \frac{1}{\hbar}\int_0^t E_n(\mu(t'))dt' - i\int_0^t \langle n(\mu(t'))| \frac{\partial}{\partial t'} |n(\mu(t'))\rangle \, dt'. \tag{1.2}$$

The second term is the Berry phase, γ_n, which, when changing variables under the integral, has the form

$$\gamma_n = i\int_{\mathcal{C}} \langle n(\mu)| \nabla_\mu |n(\mu)\rangle \, d\mu, \tag{1.3}$$

where $\mathcal{C}$ denotes the contour in parameter space that the time evolution traces out. The Berry phase is an example of a geometrical phase, because it depends only on the contour in parameter space that the time evolution defines, and not on how quickly the contour is traversed.

Interestingly, although the Berry phase could have been discovered early-on [17, 27], its significance was not realised until the 1980s [26]. This is because one might expect that we could perform a gauge transformation and remove it. However, if the contour in parameter space is closed, this is not true. In this situation, the Berry phase is non-trivial and can give rise to topological properties. We can additionally define the Berry connection as the integrand in Eq. 1.3.

$$\mathbf{A}_n = i \langle n(\mu)| \nabla_\mu |n(\mu)\rangle . \tag{1.4}$$

This then puts the expression for the Berry phase in a very suggestive form when Stokes' theorem is applied in the case where μ is a 3D vector:

$$\gamma_n = \int_{\mathcal{S}} \mathbf{\Omega}_n(\mu) \cdot d\mathbf{S}, \tag{1.5}$$

where $\mathcal{S}$ is the surface enclosed by $\mathcal{C}$, and $\mathbf{\Omega}_n = \nabla_\mu \times \mathbf{A}_n$ is the Berry curvature.

At this stage we can start to see the analogy with electromagnetism. The Berry curvature acts like a magnetic field in parameter space with the Berry connection playing the role of the magnetic vector potential. The Berry phase is then the magnetic flux

through the surface defined by the contour that is swept out by the time evolution. Furthermore, one can show that degeneracy points in parameter space (i.e. points where two bands touch) act like magnetic monopoles, and hence are sources of Berry curvature.

We have thus set up the necessary formalism to describe the local geometry of bands in parameter space, and demonstrated an analogy with electromagnetism. But how do we get from this local geometry to global topology?

We can take inspiration from the link between geometry and topology in pure mathematics. The local geometry of some surface S can be described by its Gaussian curvature K. The Gauss-Bonnet theorem connects the Gaussian curvature to a global property of the surface, its genus g. The genus counts the number of holes the surface has (e.g. a torus has $g = 1$), and is hence clearly an integer. The theorem states

$$\int_S K dS = 4\pi(1 - g). \tag{1.6}$$

It therefore constructs a global integer-valued topological invariant by integrating an appropriate local quantity over a surface. The Chern number ν_n is calculated in an analogous way:

$$\nu_n = \frac{1}{2\pi} \int_{\mathcal{S}} \mathbf{\Omega}_n \cdot d\mathbf{S}, \tag{1.7}$$

where S denotes a closed surface in parameter space. Like the genus, it is an integer.

At first, it would appear that the Chern number must always be zero! Naively, we could use Stokes' theorem to convert the surface integral to a line integral over the surface boundary. But, for a closed surface, there is no boundary, so the integral must vanish. The resolution to this is that we can't apply Stokes' theorem if $\mathbf{A}_n$ has singularities on the surface. We can turn this statement around to say that the Chern number is only non-zero if the Berry connection has a singularity in the region of parameter space we are considering.

We can again draw an analogy with magnetism. In electromagnetism, the magnetic flux through a closed surface counts the number of magnetic monopoles enclosed within

that surface. From earlier, degeneracies in parameter space are analogous to magnetic monopoles. Therefore, the Chern number counts the number of degeneracies in the region of parameter space the surface encloses.

Finally, we can tie up our description by noting that, in practice, the parameter space is often taken to be momentum space, and the closed surface used to define the Chern number is the first Brillouin zone. The Chern numbers are calculated for each Bloch band in the system. This then leads to the topological explanation of the integer quantum Hall effect. The conductance can be expressed as the sum of the Chern numbers over all occupied bands, which is known as the TKNN formula [28].

1.2.3 The Quantum Hall Effect Outside of the Solid State

Whilst the quantum Hall effect was originally discovered in the context of 2D electron gases, 2D models with broken time-reversal symmetry have since been realised in a variety of quantum simulation platforms by engineering the key ingredients [13, 29], namely the 2D geometry and time-reversal symmetry breaking. One motivation in engineering the integer quantum Hall effect in these controllable artificial systems is as a stepping stone towards the fractional quantum Hall effect [24], which can be realised if sufficiently strong interactions can be engineered in the platform. Apart from the highly unusual properties of the fractional quantum Hall ground state and excitations, such as fractional charge and excitations, a controllable realisation of the effect is of great interest in topological quantum computing, in which the (2 + 1)D world lines of the anyonic excitations of the Hall liquid can be braided together and used to form gates for quantum computation [2, 24]. The key point is that the world-line braids are topologically protected, meaning that computations are particularly robust against errors, in contrast to other approaches to quantum computing.

We end this discussion on a practical note. In the solid-state quantum Hall effect, the necessary time-reversal symmetry breaking required comes from the magnetic field applied to the electrons. However, as discussed above, quantum simulators often use

neutral particles such as photons or neutral atoms, so applying a physical magnetic field will not have the desired effect. However, an effective artificial magnetic field can often be engineered. In the context of lattice models, this can be achieved via the Peierls phase. For a particle of charge q hopping on a 2D lattice threaded by a perpendicular magnetic field, each hop in the x direction with lattice spacing a leads to the wavefunction acquiring a phase:

$$\theta_x(y) = \frac{q}{\hbar} \int_x^{x+a} A_x(x', y) dx', \tag{1.8}$$

where $A_x(x, y)$ is the x-component of the magnetic vector potential, and where a similar expression holds for hops in the perpendicular y-direction. In many quantum simulation platforms for neutral particles, the phase acquired by the particle hopping can be directly engineered, and hence associated with some effective gauge field via analogy with the Peierls phase. In this way, effective magnetic fields for neutral particles can be designed. To illustrate the idea, consider our old example of neutral atoms hopping in an optical lattice, realising the Hubbard model. The strength of the hopping in the lattice can be controlled using modulation-assisted tunnelling, in which the lattice is shaken periodically [30, 31]. This periodic shaking causes corresponding oscillation in the atomic quasi-momentum, and, for a high-frequency driving, the average of the energies explored during the shaking leads to a renormalised hopping energy. Additionally using off-resonant driving then leads to a phase on the renormalised hoppings, which can then be exploited in the above way to engineer an artificial magnetic field.

Having defined and motivated quantum simulation in general, and given an overview of 2D topological physics in particular, we now turn to the new results of this thesis, in which we cover three different examples of quantum simulation in three different experimental platforms. In Chapter 2, we demonstrate the experimental realisation of a synthetic dimension for ultracold atomic gases, in which the energy eigenstates of a harmonic trap are interpreted as sites on a 1D lattice, coupled by an external driving potential. We then characterise this synthetic dimension by demonstrating Bloch oscillations up-and-down the ladder of trap states. In Chapter 3, we present a proposal to realise quantum Hall

physics in a 1D array of coupled optical waveguides, in which the propagation time of an optical pulse plays the role of a continuous spatial dimension. We also suggest some implications of this quantum Hall physics for optics. Finally, in Chapter 4, we present the results of a recent proposal to use lattices formed from commercial coaxial cables as a quantum simulator. We consider a particular 2D lattice, calculate the Bloch wave dispersion, and show how to exploit the parameters of the lattice to control interesting features such as Dirac points and flat bands. We now turn to the experimental realisation of a synthetic dimension scheme for ultracold atomic gases.

CHAPTER 2

BLOCH OSCILLATIONS ALONG A SYNTHETIC DIMENSION OF ATOMIC TRAP STATES

Chapter 2 consists of a manuscript demonstrating the experimental realisation of a synthetic dimension scheme for ultracold atomic gases, for future quantum simulation applications. Although the paper contains some introductory material, before presenting the manuscript itself we first provide a more detailed introduction. We begin by introducing the concept of a synthetic dimension and reviewing its history. We then demonstrate the idea with an example scheme that the new work in this chapter is based on. Finally, we briefly summarise the physics of Bloch oscillations, which we employ in the paper to demonstrate and characterise our synthetic dimension scheme. The manuscript itself then follows.

With reference to the author list on the manuscript, I performed all analytical and numerical calculations and some data analysis under the guidance and supervision of H.M.P., N.G. and G.S. All experimental work was carried out by A.S. and T.E. under the supervision and guidance of of G.B. and V.G. I initially drafted the manuscript and was responsible for the majority of the writing, with subsequent writing and editing by all authors.

2.1 Introduction to Synthetic Dimensions

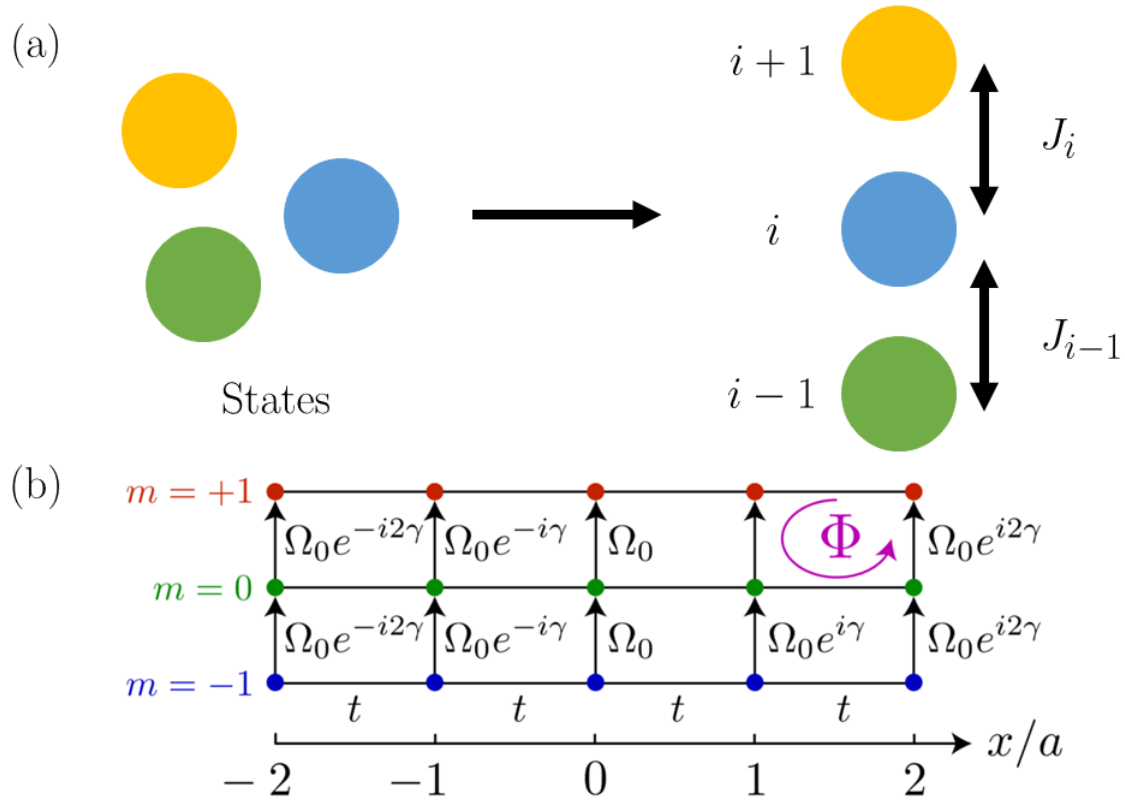

Figure 2.1: (a): Schematic of the concept of a synthetic dimension. A set of states is selected (coloured circles) and coupled together via e.g. an external drive, leading to a set of tight-binding hopping energies $\{J_i\}$. The coupled states are then re-interpreted as a 'synthetic' spatial dimension. (b): Schematic of the first proposed synthetic dimension scheme, in which three atomic states (coloured circles), labelled by the angular momentum quantum number m, are coupled together with a hopping energy Ω_0. The synthetic dimension is combined with motion along an optical lattice with lattice spacing a and hopping energy t. The synthetic dimension hops include a Peierls phase $x\gamma/a$ whose value depends on the position in the optical lattice x, which produces a net phase gain around a plaquette Φ, which leads to the interpretation as an artificial gauge field. (b) is adapted from [32].

Synthetic dimensions are a powerful quantum simulation tool [13], used mostly in ultracold atomic and photonic experimental platforms. The idea of most schemes is to identify a set of states of some physical system, and to then re-interpret them as forming a lattice along a 'synthetic' spatial dimension. The states are then coupled, for example by applying an external driving potential, which is then thought of as being analogous

to a tight binding hopping between the lattice sites. This situation is shown schematically in Fig. 2.1(a). The synthetic dimension can then be used to simulate 1D physics, or be combined with some number of real and/or synthetic dimensions to implement higher-dimensional models. Synthetic dimensions are useful for realising lattice physics generally, particularly topological models and, excitingly, higher-dimensional models such as the 4D quantum Hall effect [33–35]. They are a particularly useful technique to explore topological models because, as discussed in the Introduction, an important class of such models depends on breaking time-reversal symmetry via a magnetic field. Complex hoppings along a synthetic dimension often naturally occur as part of the scheme, and can usually be further engineered to depend on the position along some other dimension, leading directly to an effective magnetic field via the Peierls phase.

2.1.1 History of Synthetic Dimensions

The concept of a synthetic dimension in the context of topological physics was first introduced theoretically in 2014 in a proposal for ultracold atomic gases [32]. The proposal considered the engineering of a 2D magnetic lattice model, with one real spatial dimension provided by a 1D optical lattice, and with the second dimension being a synthetic dimension of internal atomic states. These states are laser-coupled, including a position-dependent phase factor which can be thought of as a Peierls phase, which is how the artificial magnetic field is introduced, as discussed previously. The setup is shown schematically in Fig. 2.1(b). This proposal was followed by two independent experimental realisations based on the use of hyperfine states [36, 37]. Whilst this atomic state scheme has certain advantages, such as the natural occurrence of sharp edges at both ends of the synthetic dimension, it does also have some drawbacks, with the major issue being the relatively small synthetic lattices, often consisting of only a few sites. This initial line of research has therefore spawned a number of other approaches to synthetic dimensions in ultracold gases, in which other types of state are used as lattice sites. This includes momentum states [38–43], which are particularly advantageous in that they can lead to relatively

large lattices (although scaling this up to higher dimensions is technically challenging), and each hopping can be controlled individually, giving a lot of tunability over the model that is realised. Otherwise, one can use the eigenstates of a harmonic trap [44–46] (more of which shortly), which is a relatively simple scheme that produces very long dimensions of several tens of sites. Finally, molecular states [47, 48] are another proposed approach which could have many of the same advantages as momentum state lattices, with control over individual hoppings and very long lattices, facilitated by the rich state structure of molecules. However, this approach is also technically challenging and is still under development. We also note that the original internal atomic state scheme was also further developed [35, 49–53], leading to the current state-of-the-art for this technique, in which the $J = 8$ manifold of ^{162}Dy is used, leading to a synthetic dimension of 17 sites [51]. Such a system is large enough to distinguish bulk and edge physics, but scaling it up to the size of momentum space or harmonic state lattices is still challenging.

Away from ultracold gases, the other major platform in which synthetic dimensions have been extensively studied is photonics [54, 55]. Whilst the photonic schemes are similarly important in simulating models for fundamental science, they also suggest device applications. For example, realising 2D topological models in photonic synthetic dimension schemes allows access to chiral, robust edge modes of photons. The one-way nature of these modes may have applications in optical isolation, of huge importance for integrated photonics [19], and the addition of gain elements may lead to lasing from the edge modes, allowing the laser to inherit the robustness of the edge states [56].

As with ultracold gases, the main approaches to synthetic dimensions are distinguished by the type of states that are coupled together, with the main candidates being orbital angular momentum modes, which can readily be engineered to include sharp edges; frequency modes [19, 57–61], which can be extended naturally towards high-dimensions, and spatial eigenmodes [62]. Curiously, photonic systems can also use time as a synthetic spatial dimension. Time can be used in a discrete way in a time-multiplexing scheme [63], in which the arrival times of two optical pulses travelling around two fibre loops of different

lengths can be thought of as a position along a 1D synthetic dimension, and this approach has since been used to investigate a variety of 1D effects. Time can also be thought of as a continuous synthetic dimension, as we discuss in Chapter 3 [64]. We note that there is one other continuous synthetic dimension scheme in photonics, namely the angular coordinate of a ring resonator [65].

2.1.2 A Synthetic Dimension of Atomic Trap States

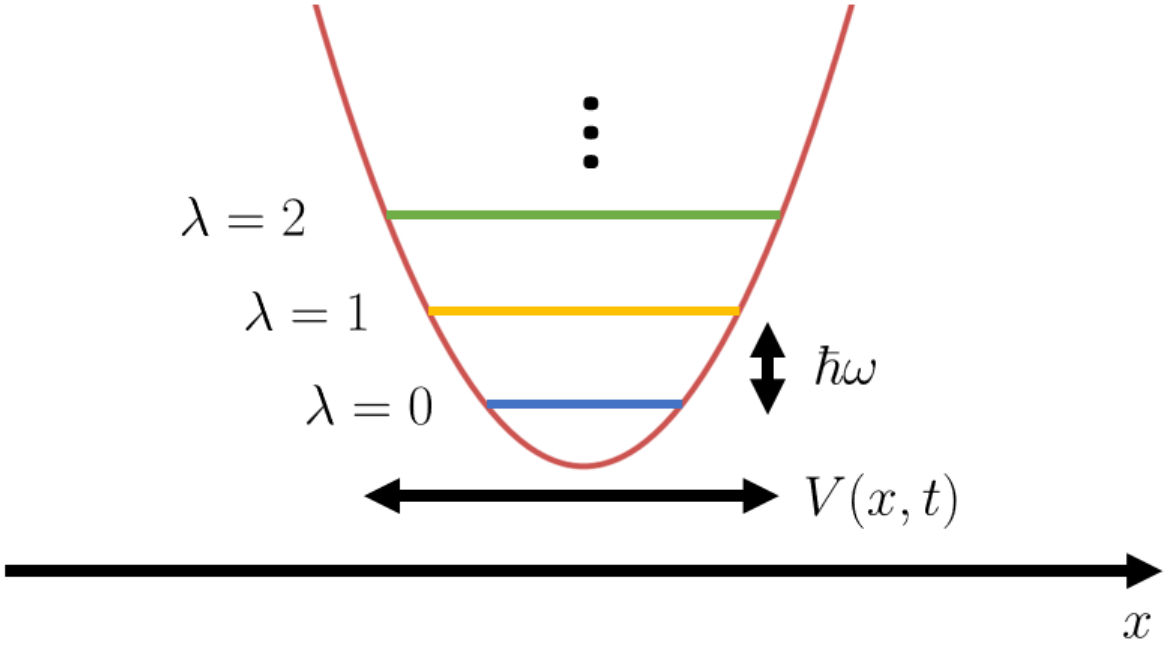

Figure 2.2: Schematic of the shaken trap synthetic dimension scheme. A 1D harmonic trap along the x-direction with energy level spacing $\hbar\omega$ and eigenstates indexed by $\lambda = 0, 1, 2...$ is driven with an external potential $V(x,t)$. The driving potential is chosen to couple neighbouring trap states together, forming a synthetic dimension.

Having reviewed the history of synthetic dimensions, we now consider a particular scheme in more detail. This example will serve to further illustrate the idea of a synthetic dimension, and will provide important background for the work presented in this chapter, where we experimentally demonstrate a synthetic dimension in which the lattice sites are the energy eigenstates of a harmonic trap confining a cloud of cold atoms, with the

states being coupled together by applying an external driving potential that shakes the harmonic trap. Such a synthetic dimension scheme was first proposed theoretically in 2017 [44]. We now review some of the results from that proposal. We consider particles of mass m confined in a 1D harmonic trap with frequency ω lying along the x-direction. We can write the Hamiltonian as:

$$\hat{H}_0 = \frac{\hat{p}_x^2}{2m} + \frac{1}{2}m\omega^2\hat{x}^2 = \omega\sum_{\lambda=0}^{\infty}\lambda\left|\lambda\right\rangle\left\langle\lambda\right|, \tag{2.1}$$

where we set $\hbar = 1$, and we write the Hamiltonian in the basis of trap eigenstates which we index with λ ($\lambda = 0, 1, 2...$). We can then apply a time-dependent potential to couple the trap states together. In particular, we apply the simple potential:

$$\hat{V}(x,t) = \kappa\hat{x}\cos(\omega_D t + \phi), \tag{2.2}$$

where we choose the driving frequency $\omega_D \equiv \omega - \Delta$, where Δ is a small detuning. κ is the driving potential strength and ϕ is an overall phase, which we return to later. The setup is shown schematically in Fig. 2.2. This driving potential gives the total Hamiltonian $\hat{H}(t) = \hat{H}_0 + \hat{V}(x,t)$. This complicated time-dependent Hamiltonian is then understood using the techniques of Floquet theory [66, 67]. In this approach, we take a time-periodic Hamiltonian and aim to understand its dynamics stroboscopically, up to a driving period. We define a static 'Floquet' Hamiltonian $\hat{H}_F$:

$$\hat{U}(0,T_D) \equiv e^{-iT_D\hat{H}_F}, \tag{2.3}$$

where $\hat{U}(0,T_D)$ is the unitary time evolution operator over a single period of the driving potential $T_D \equiv 2\pi/\omega_D$. This static Hamiltonian captures the dynamics each driving period, but any information within a period (known as micromotion) is averaged out. We can always evaluate the exact Floquet Hamiltonian numerically via Eq. 2.3, but in the case of the simple driving potential applied here (Eq. 2.2), we can analytically

approximate it by employing the rotating wave approximation (RWA), in which we take the high-driving-frequency limit $\omega_D \approx \omega \gg$ all other energy scales. In particular, we first transform the full Hamiltonian to a frame rotating with frequency ω_D using the unitary operator $\exp(it\omega_D\hat{\lambda})$, where $\hat{\lambda}$ is the 'position' operator along the ladder of trap states. We then make the RWA, neglecting terms that oscillate too quickly in the sense of the limit above. This procedure produces the Hamiltonian:

$$\hat{H}_{\mathrm{RWA}} = \Delta \sum_{\lambda=0}^{\infty} \lambda \left|\lambda\right\rangle \left\langle\lambda\right| + \sum_{\lambda=0}^{\infty} J_\lambda (e^{i\phi} \left|\lambda - 1\right\rangle \left\langle\lambda\right| + \mathrm{H.C.}) \approx \hat{H}_F, \tag{2.4}$$

where the position-dependent hopping energy $J_\lambda \equiv \kappa\sqrt{\lambda/8m\omega}$. Note that, in the paper presented later in this chapter, we actually project a different driving potential onto the atomic cloud that produces Floquet Hamiltonian hopping matrix elements that are nearly independent of λ, suggesting that this approach to synthetic dimensions offers significant control over the fine details of the effective Hamiltonian, provided that the applied shaking potential can be well-controlled. We also note that we will shortly demonstrate a particularly long synthetic dimension of several tens of trap states. Returning to the present problem, we therefore see the synthetic dimension emerge explicitly, with adjacent trap states being coupled with the position-dependent hopping energy. We also see that the detuning tilts the lattice, playing the role of a constant force along the synthetic dimension. We exploit this feature in this chapter to demonstrate and characterise the synthetic dimension. The overall driving phase ϕ appears as a unitary phase factor on the hoppings, meaning that, if the phase can be made to depend on the position along a perpendicular dimension, we find the natural emergence of a Peierls phase, as we return to shortly. One finds good agreement between this analytical RWA Hamiltonian and the Floquet Hamiltonian calculated numerically from the time evolution operator, provided that the rotating wave approximation is not violated by, for example, using too strong a driving potential.

As an aside, we note that there is much more to be said about the Floquet theory

approach [66, 67]. In particular, the eigenstates and eigenvalues of the 'Floquet operator' $\hat{U}(0, T_D)$ (Eq. 2.3) are, by the Floquet theorem, time-periodic with the same period as the driving, and form a complete basis for the problem. These states then give rise to a new Hamiltonian over an enlarged Hilbert space, whose spectrum consists of an infinite number of copies of the bands of the Floquet Hamiltonian, repeated periodically in multiples of the driving energy. The field of 'Floquet engineering' then consists of reverse-engineering the original time-dependent Hamiltonian to yield a desired Floquet Hamiltonian spectrum. The periodicity in the spectrum can also give rise to new physics of its own, such as anomalous Floquet topological phases [68].

Returning to the problem at hand, the 2017 proposal then goes on to demonstrate the use of this synthetic dimension to engineer the Harper-Hofstadter model [69, 70]. This is a paradigmatic model for magnetic physics in lattice systems, illustrating the physics of non-interacting particles moving on a 2D square lattice under the influence of a perpendicular magnetic field. The model contains very rich physics, including a fractal spectrum known as the Hofstadter butterfly. The model is proposed in the shaken trap synthetic dimension scheme by allowing the particles to also move in a 1D optical lattice, and by making the driving phase ϕ depend upon the position of the particle along that real space dimension, as indicated earlier. This allows for the interpretation of the phase as a Peierls phase, which can then be associated with an effective magnetic field. As discussed in the paper we present later in this chapter, we note that 2D physics could be achieved in an even more natural way by exploiting the motion of the atomic cloud within the trap that they are confined in anyway.

The aforementioned single-particle physics is also extended by considering how the usual contact interactions typical of atomic gases translate into the synthetic dimension. The interactions are complicated, and are being investigated in detail as part of on-going theoretical work. However, in general, they are long-range, and are quite different to both the usual very short-range real-space contact interactions, and to the infinite-range $SU(N)$ interactions found in some other atomic synthetic dimension schemes [32]. The

finite range of the interactions in this scheme is particularly interesting because they, once combined with the aforementioned quantum Hall physics, may be a route towards fractional quantum Hall states.

Having introduced the synthetic dimension scheme that we realise in experiment, we now review the physics of Bloch oscillations, which are exploited in the manuscript to demonstrate and characterise the synthetic dimension.

2.2 Bloch Oscillations

Bloch oscillations are a well-known piece of lattice physics, first proposed in the solid state context [71], and they have since been observed experimentally in a number of other systems also [72–87]. They have proven to be difficult to observe in a solid-state setting [88, 89], so most experiments have focused on other platforms, mainly ultracold gases in optical lattices and cavities. Bloch oscillations refer to the oscillation of a particle's position when it moves on a lattice under the influence of an applied force. This is a surprising result that emerges due to the presence of a lattice. For contrast, consider a free particle of mass m, with the dispersion $E(k) = \hbar^2 k^2/2m$ (i.e. moving in free space, without any lattice). The semiclassical equation of motion for the particle under a constant applied force F is:

$$\hbar \frac{dk}{dt} = F, \tag{2.5}$$

which yields, upon integration,

$$k(t) = k(t = 0) + Ft. \tag{2.6}$$

Note that the semiclassical approach we adopt here models the particle as a wavepacket with both a well-defined position and momentum. We also assume that the force is weak in comparison with the band gap, such that we only have translation of the initial state along a band, and not transitions into higher bands. We also know that the particle group

velocity is:

$$v(k) \equiv \frac{dE}{dk} = \frac{\hbar k}{m}. \tag{2.7}$$

Integrating the velocity to calculate the particle position, and combining with the result for the momentum increase as a function of time, yields:

$$x(t) = x(t=0) + \frac{\hbar F}{m} t^2. \tag{2.8}$$

Note that we assumed, for simplicity, that $k(0) = 0$. We therefore find that the particle position increases monotonically with t, as we would expect for a free particle under a constant applied force. However, if we instead place the particle on a tight-binding lattice with nearest-neighbour hoppings, we find very different behaviour. In this case, we instead have the dispersion $E(k) = -2J\cos(ka)$, where a is the lattice spacing and J is the hopping energy. Carrying out the same calculation as above now shows that the particle position is:

$$x(t) = x(t=0) - \frac{2J}{F} \cos\left(\frac{aFt}{\hbar}\right). \tag{2.9}$$

We therefore find sinusoidal oscillations with an amplitude and frequency set by the applied force F, in stark contrast to the free particle case. In the paper, we employ Bloch oscillations along the lattice of atomic trap states as a simple but non-trivial piece of physics to demonstrate and characterise our synthetic dimension.

Having introduced and motivated the physics behind this chapter, we now present the paper itself.

Bloch Oscillations Along a Synthetic Dimension of Atomic Trap States

Christopher Oliver,[1] Aaron Smith,[1] Thomas Easton,[1] Grazia Salerno,[2] Vera Guarrera,[1] Nathan Goldman,[3] Giovanni Barontini,[1] and Hannah M. Price[1]

[1] *School of Physics and Astronomy, University of Birmingham, Edgbaston, Birmingham B15 2TT, United Kingdom*
[2] *Department of Applied Physics, School of Science, Aalto University, Espoo, Finland*
[3] *Center for Nonlinear Phenomena and Complex Systems, Université Libre de Bruxelles (U.L.B.), B-1050 Brussels, Belgium*

Synthetic dimensions provide a powerful approach for simulating condensed matter physics in cold atoms and photonics, whereby a set of discrete degrees of freedom are coupled together and re-interpreted as lattice sites along an artificial spatial dimension. However, atomic experimental realisations have been limited so far by the number of artificial lattice sites that can be feasibly coupled along the synthetic dimension. Here, we experimentally realise for the first time a very long and controllable synthetic dimension of atomic harmonic trap states. To create this, we couple trap states by dynamically modulating the trapping potential of the atomic cloud with patterned light. By controlling the detuning between the frequency of the driving potential and the trapping frequency, we implement a controllable force in the synthetic dimension. This induces Bloch oscillations in which atoms move periodically up and down tens of atomic trap states. We experimentally observe the key characteristics of this behaviour in the real space dynamics of the cloud, and verify our observations with numerical simulations and semiclassical theory. The Bloch oscillations thus act as a smoking gun signature of the synthetic dimension, and allow us to characterise the effective band structure. Our methods provide an efficient approach for the manipulation and control of highly-excited trap states, and set the stage for the future exploration of topological physics in higher dimensions through the use of a tunable artificial gauge field and finite-range interactions.

I. INTRODUCTION

Synthetic dimensions provide a powerful approach for simulating condensed matter physics in cold atoms[1–14] and photonics[16–19], and they are opening up many new avenues for simulating and exploring exotic physics, including quantum Hall ladders[3,4,10], non-Hermitian topological bands[22], topological Anderson insulators[23], and even lattice physics in four dimensions or higher[1,11,24]. A key reason that this framework is so powerful is that it is very general, and can be applied to a wide-range of very different physical systems. For example, synthetic dimensions have so far been realised experimentally in cold atoms with hyperfine[1,3,4], magnetic[7], Rydberg[8,9], and clock states[5,6], as well as with momentum[10,11], orbital[14] and superradiant states[12]. However, in these experiments, the size of the synthetic dimension has been so far limited by the number of states that can feasibly be coupled. Indeed, the largest momentum state lattice[15] employed so far consists of a 1D lattice of 21 sites.

Notably, it has been recently realised that such limitations can be lifted if external degrees of freedom associated with trapping potentials are used to generate the synthetic dimensions[16,20,21]. Indeed, trapping potentials typically allow for tens or hundreds of trapped states in each direction, and by suitably coupling them one could implement very long synthetic dimensions, unleashing the full potential of this technique for quantum simulation. Additionally, this kind of synthetic dimension is extremely appealing because it provides a framework for the manipulation and control of trap states. A range of applications including quantum simulations in optical lattices[25–27], trapped and guided atom interferometry[28–30] and quantum thermodynamics[31–33] require the use of highly-excited trapped states, which are generally difficult to realise with a good degree of precision and control.

In this work, we experimentally engineer a very long synthetic dimension of many tens of atomic trap states by dynamically modulating the harmonic trap of an ultracold atomic sample[20,21]. By controlling the driving frequency we generate a force along the synthetic dimension that induces Bloch oscillations, which act as a smoking gun signature that the synthetic dimension behaves as expected. Bloch oscillations were first famously predicted for electrons moving in a crystal under an electric field, and have since been observed in various setups, including optical lattices for cold atoms[34], as well as synthetic dimensions of photonic frequency modes[35] and of room-temperate molecular angular momentum states[36]. However, Bloch oscillations in our experiment are physically very different from previous realizations, as they correspond to atoms periodically oscillating between low- and high-energy states of the harmonic trap. As such, another benefit of the synthetic dimension Bloch oscillations implemented here is that they allow us to explore highly-excited harmonic states, and thus can lead towards a novel approach for quantum engineering of external atomic states. More generally, this work paves the way for the exploration of higher-dimensional quantum Hall physics with artificial magnetic fields, and opens new opportunities in quantum simulations more widely. For example, a tunable artificial gauge field can be implemented by spatial modulation of the phase of the driving

potential, allowing access to 2D quantum Hall physics. Furthermore, mean-field interactions between the atoms in real space should give rise to exotic interactions that are long-range and decay with distance along the synthetic dimension[20], in contrast to the usual interactions in atomic gases and to the $SU(N)$ interactions in some other atomic synthetic dimension schemes. We therefore expect interesting ground state physics under the inclusion of interactions which will be of interest for future study.

II. OVERVIEW OF THE SCHEME

To introduce our scheme, let us consider an atomic cloud in a cigar-shaped harmonic trap with trap frequencies $\omega_x = \omega_z \gg \omega_y$. In order to realise the synthetic dimension, we couple together the atomic trap states of the strong trapping potential along x with the spatially- and temporally-varying driving potential given by:

$$V_D(x,t) = -V_0\Theta(x\sin(\omega_D t + \varphi)) \tag{1}$$

where V_0 is the driving amplitude, $\Theta(x)$ is the Heaviside step function, ω_D is the driving frequency and φ is the initial driving phase. Physically, this corresponds to illuminating the upper half of the atomic cloud with constant power for the first half of the period, $T_D = 2\pi/\omega_D$, before illuminating the lower half with the same constant power over the second half of the period (see Fig. 1(a)). Classically, the driving potential provides a force:

$$F_D = -\frac{\partial V_D}{\partial x} = V_0\delta(x)\mathrm{sgn}(\sin(\omega_D t + \varphi)), \tag{2}$$

which physically corresponds to a force localised on the origin whose direction changes every half-period. This driving protocol is chosen because it is simple to implement, robust and it leads to a simple Floquet Hamiltonian with near-constant nearest-neighbour hoppings, corresponding to a textbook 1D tight binding model, as discussed below. Combining Eq. 1 with the 1D harmonic oscillator Hamiltonian along x gives the time-dependent Hamiltonian:

$$\hat{H}(t) = \hbar\omega_x \sum_\lambda \lambda \left|\lambda\right\rangle\left\langle\lambda\right| + V_D(x,t), \tag{3}$$

written in the eigenstate basis of the "strong" trap along x, as indexed by $\lambda = 0, 1, 2....$ The stroboscopic dynamics of this system is captured by an effective time-independent Floquet Hamiltonian, which we can approximate over a large number of trap-states by (see Supplemental Material[37]):

$$\hat{\mathcal{H}} \approx \hbar\Delta \sum_\lambda \lambda \left|\lambda\right\rangle\left\langle\lambda\right| + J\sum_\lambda \left[ie^{i\varphi}\left|\lambda+1\right\rangle\left\langle\lambda\right| + \mathrm{h.c}\right] \tag{4}$$

where $\Delta \equiv \omega_x - \omega_D$ is the (small) drive detuning and J is a uniform hopping amplitude, which itself depends on V_0 and ω_x and is calculated using Floquet theory[37]. Note that this description is valid for near-resonant driving in a deep harmonic trap, i.e. such that $\omega_x \simeq \omega_D \gg \Delta, J/\hbar$. As depicted in Fig. 1(a), Eq. 4 describes a particle hopping between nearest-neighbour sites along a 1D tight-binding lattice with unit spacing in a synthetic dimension. The detuning plays the role of a constant force, $F \equiv -\hbar\Delta$, which therefore can induce Bloch oscillations. Note that the shaking phase φ appears in the effective Hamiltonian as a hopping phase, which we will exploit below to average over unwanted micromotion effects.

In the absence of a force along the synthetic dimension, i.e. when $\Delta = 0$, the effective model in Eq. 4 is translationally invariant along the synthetic dimension and has a single energy band in the Brillouin zone. Applying a nonzero force (i.e. $\Delta \neq 0$) accelerates a semiclassical wavepacket formed in the synthetic dimension bulk, such that it undergoes Bloch oscillations across the Brillouin zone, with a center-of-mass (COM) position along the synthetic dimension, λ_{com}, that varies as[20]:

$$\lambda_{\mathrm{com}}(t) = \lambda^0_{\mathrm{com}} + \frac{2J}{\hbar\Delta}(1 - \cos(2\pi f_B t)), \tag{5}$$

from the initial position $\lambda_{\mathrm{com}}(t=0) = \lambda^0_{\mathrm{com}}$ and where f_B is the Bloch oscillation frequency. As we can set the spacing between the fictitious synthetic lattice sites equal to one, the periodic Brillouin zone covers $[-\pi, \pi]$. The Bloch oscillation frequency is then set by the magnitude of the applied force divided by the length of this Brillouin zone, i.e. $f_B = |\Delta|/2\pi$, and so is entirely controlled by the detuning. Conversely, the amplitude of the Bloch oscillations is proportional to the bandwidth divided by the force, i.e. $4J/\hbar\Delta$, and so depends on the detuning but also, through J, on the trap frequency and shaking power[37]. The Bloch oscillations therefore provide a way to transport atoms between different trap states, with independent control over both the timescale and number of trap states explored. Experimentally, we use a thermal cloud of ^{87}Rb atoms in a harmonic trap with trapping frequencies $\omega_x = \omega_z \simeq 2\pi \times 160$ Hz and $\omega_y \simeq 2\pi \times 10$ Hz. The cloud was measured, both in-situ and with standard time-of-flight techniques, to have an initial temperature of $T \simeq 20$ nK. We used a rapid evaporation ramp to prevent the sample from condensing at this temperature, thus reducing the effect of mean-field interactions[20], which may complicate the dynamics and will be of interest in future investigations. To realise the driving potential of Eq. 1, we utilise a digital micromirror device (DMD) that allows us to dynamically and spatially control the intensity profile of a laser beam with wavelength 800 nm (see Appendix A). We verify that the trapping and driving potentials are aligned to within $\simeq 1\mu$m. Our driving potential was chosen because it was found to be the most effective and robust, in the sense of not being sensitive to misalignments and other imperfections. This is in addition to the favourable theoretical properties discussed above. We then perform absorption imaging of the atomic cloud in position space after a

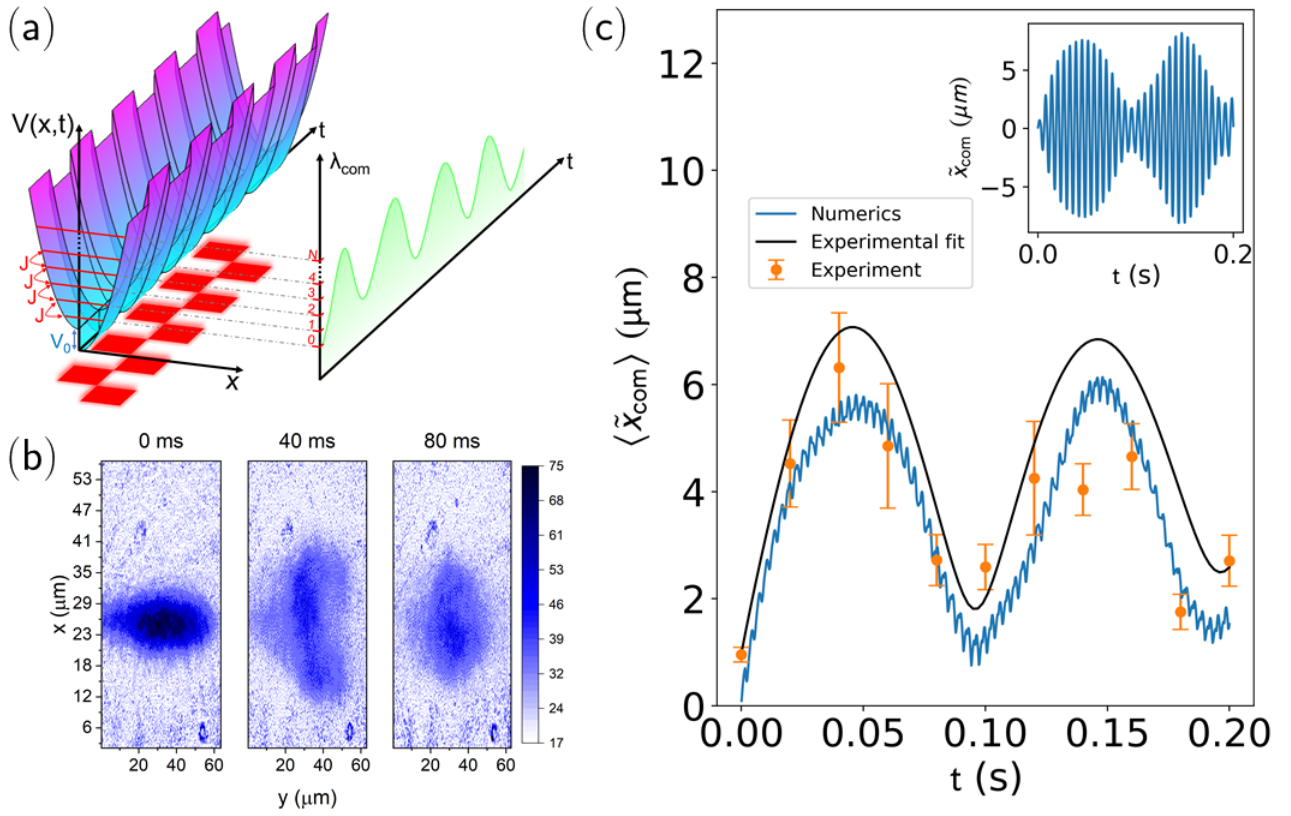

FIG. 1. **Schematic of the experiment and signatures of the synthetic-dimension Bloch oscillations in real space.** (a): Schematic of the DMD pattern (*red*), which shakes the harmonic trap (*blue/purple*) and couples together nearest-neighbour trap states with an approximately uniform hopping amplitude, J, in order to create the synthetic dimension. Bloch oscillations (*green*) can be driven along the synthetic dimension by applying a force along λ, corresponding to detuning the shaking frequency from the trap frequency. (b): Experimentally, the cloud is imaged after a short time-of-flight expansion, as demonstrated here for a detuning of $\Delta = 9.84 \times 2\pi$ Hz. The colour scale is the column density in arbitrary units. The full dynamics includes micromotion within each driving period, so the experimental data are averaged over several values of φ. This averaging procedure makes the cloud appear to widen, although the true cloud width is approximately constant. (c): The real-space center-of-mass position, x_{com}, of the atomic cloud is extracted, as shown here for the same data as in (b). The experimental data (*orange*) are fitted (*black*) with a function motivated by Bloch oscillations in the synthetic dimension (see Appendix B and Supplementary Material), which captures the real-space dynamics well. Also shown are numerical results (*blue*) with a suitable TOF correction, discussed in the Main Text. The micromotion within each driving period can be seen in the inset for an initial driving phase of $\varphi = 0$. To reduce these unwanted micromotion effects, we average both the experiment and numerics over several values of φ (e.g. $\varphi = 0$ and $\pi/2$) to obtain the results shown in the main panel. As can be seen numerically, the residual micromotion oscillations have a small amplitude, which can be further reduced by averaging over more initial driving phases. Panels (b) and (c) use experimental parameters of $V_0 = 4.16$ nK, $T = 20$ nK, $\omega_y = 10 \times 2\pi$ Hz, and $\omega_x = 166.5 \times 2\pi$ Hz, where the latter is determined experimentally by shifting the oscillation frequency data to pass through $(|\Delta|, f) = (0, 0)$. Experimental errorbars are 1σ statistical errors.

very short time-of-flight (TOF) expansion of $t_{\rm tof} = 5$ ms, chosen to increase the visibility of the dynamics. This is demonstrated in Fig. 1(b) for a detuning of 9.84 Hz, where we plot the real space cloud density as a function of time for an example Bloch oscillation, showing the cloud COM being displaced away from the origin. Note that the density is averaged over several values of φ in order to reduce the effect of micromotion. As such, the cloud appears to widen along x in time, although the cloud width is actually approximately constant. The initial temperature of $T \simeq 20$ nK, corresponds to $\lambda^0_{\rm com} \approx 2$ for an initial Maxwell-Boltzmann distribution of atomic energies. This means that, initially, the atoms start near one "edge" of the synthetic dimension (at $\lambda = 0$), and so atoms must move up the synthetic dimension, irrespective of the sign of the detuning, i.e. the direction of the force. The cloud also does not have a Gaussian distribution with respect to the synthetic dimension as the above semiclassical theory implicitly assumes; nevertheless, as we shall show, the prediction in Eq. 5 works well once

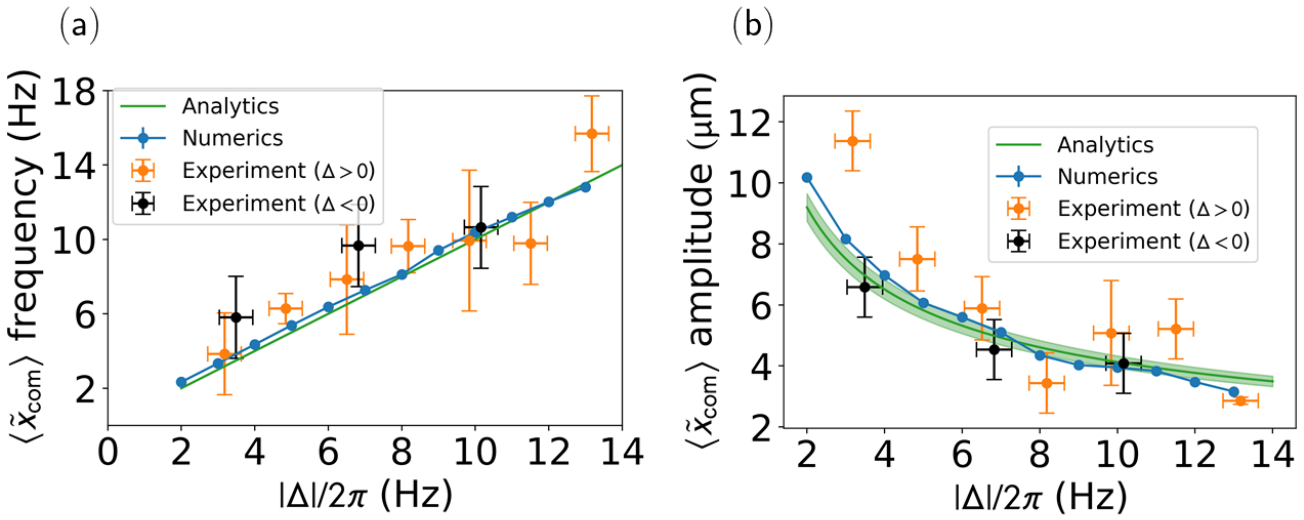

FIG. 2. **Bloch oscillation frequency and real space amplitude as a function of detuning** (a): Frequency of the Bloch oscillations for the experiment (*orange* for $\Delta > 0$ and *black* for $\Delta < 0$) and for numerics (*blue*). The observed trend is in agreement with the analytical prediction (*green*) of $f_B = |\Delta|/2\pi$ for Bloch oscillations. (b): Amplitude in real space of Bloch oscillations for the same data as plotted in panel (a). The analytical prediction (*green*) shows the expected real-space amplitude as calculated under appropriate approximations from the synthetic-dimension Bloch oscillations (see Appendix D and Supplementary Material), with the green error band calculated from the errors on J and other numerical parameters. The numerical results are obtained by fitting the same function as in experiment to the TOF-corrected, RMS-averaged results like in Fig. 1(c). Note that the numerical fit parameters also include error bars, but these are smaller than the datapoint size. We use the same parameters as Fig. 1. Experimental errorbars are 1σ statistical errors.

appropriate corrections are included (see Appendix D).

III. EXPERIMENTAL AND THEORETICAL RESULTS

Bloch oscillations in λ-space naturally translate into atomic motion along x in real space, as different harmonic oscillator eigenstates have different real-space profiles. The resulting motion can be seen in Fig. 1, where we report the measured dynamics of the real-space COM position under the action of the shaking potential, as a function of time. It is important to notice that the full dynamics also includes micromotion within each driving period[20]; for the real-space COM, as shown numerically in the inset of Fig. 1(c), the micromotion corresponds to large and fast oscillations as the atoms slosh backwards and forwards in the trap, while the stroboscopic Bloch oscillations translate into variations in the envelope of the dynamics. We are not able to reliably achieve the high time resolution to observe the micromotion in experiment, so we apply an averaging procedure to remove it. This is because of drifts in experimental parameters on a timescale of hours, which would make the large number of measurements required to reconstruct fast dynamics impractical. To overcome this, we root-mean-square (RMS) average over different experimental runs with suitably-chosen different initial driving phases, φ. The raw cloud images in Fig. 1(b) have themselves been averaged in this way. This has the effect of making the cloud appear to widen significantly over the oscillation, although in each single shot the width is approximately constant. Note that this averaging procedure slightly lowers the apparent amplitude of the motion. However, by reducing the micromotion effects, we can then clearly observe the real-space signatures of the synthetic-dimension Bloch oscillations, as reported in Fig. 1(c) for the same parameters as Fig. 1(b) (*orange*), where the experimental data is fitted by a function (*black*) motivated by synthetic-dimension Bloch oscillations (see Appendix B and Supplemental Material[37]):

$$x(t) = A\sqrt{1 - e^{-gt}\cos(2\pi f t + \phi)}, \tag{6}$$

where we fit to find the amplitude A and frequency f. We introduce the additional fit parameters g and ϕ to capture some details of the experimental data (see Appendix B and the Supplemental Material[37]). As can be seen, this fit captures the behaviour of the data very well, with agreement between the experiment and numerical simulations (*blue curve*) of a non-interacting 2D thermal cloud (see Appendix C and Supplemental Material[37]). Our numerical simulations use the time-dependent Hamiltonian to evolve an ensemble of states, each of which is a superposition over the eigenstates of the 2D trap with random phase factors to destroy the phase coherence. Physical observables such as the cloud density are found by av-

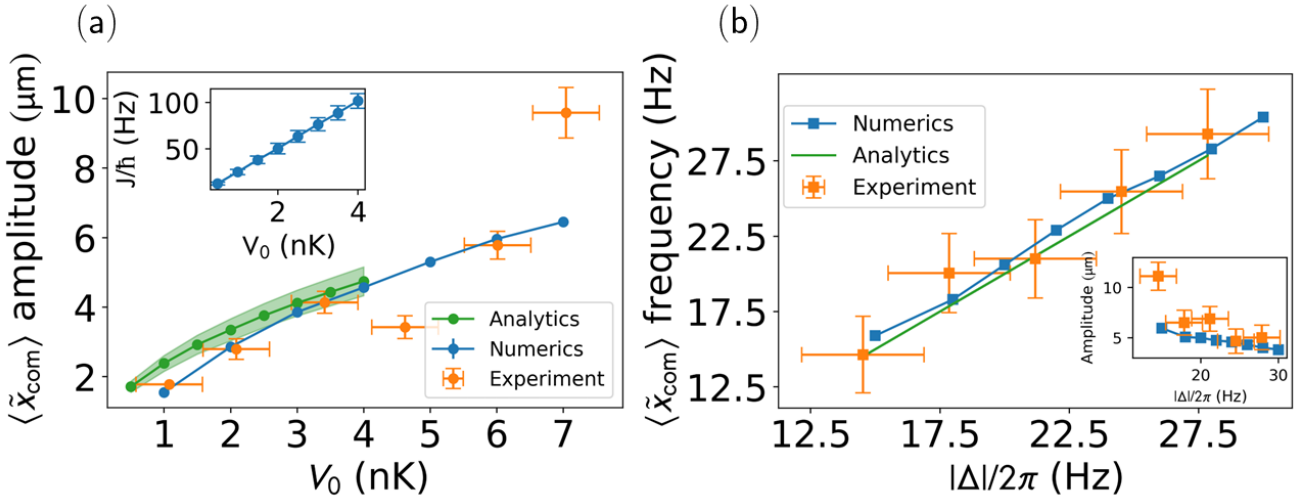

FIG. 3. **Varying the shaking power to control the dynamics.** (a): The real-space amplitude [c.f Fig. 2(b)] for different shaking powers at a fixed detuning of $\Delta = 8.3 \times 2\pi$ Hz, with $\omega_x = 162.6 \times 2\pi$ Hz. As can be seen, the experiment (*orange*), numerics (*blue*) and analytics (*green*) increase with the shaking power; this is because, as shown in the inset, the nearest-neighbour hopping amplitude, J, from Floquet theory (see Supplemental Material), increases with V_0 and hence the Bloch-oscillation amplitude along the synthetic dimension increases. Analytics are only shown up to $V_0 = 4$ nK, as at higher shaking potentials the simple nearest-neighbour tight-binding model in Eq. (4) is no longer a good description (see Supplemental Material), although the numerics and experiment still appear to exhibit Bloch-oscillation dynamics. This is shown further in (b), where we plot the amplitude fit parameter (inset) and the frequency fit parameter, for $V_0 = 11.96$ nK, with $\omega_x = 142.1 \times 2\pi$ Hz, $\Delta < 0$, and other parameters as in Fig. 1 and 2. Despite the large shaking power, we still observe similar trends to that at low power [c.f. Fig 2], and still with agreement in panel (b) to the $f_B = |\Delta|/2\pi$ analytical result from the simple tight-binding model. Experimental errorbars are 1σ statistical errors. Note that all numerical datapoints include error bars, but these are smaller than the datapoints. The green error band on the analytics is calculated from the errors on J and other numerical parameters.

eraging over these phases. To account for the fact that we do not measure the true position of the cloud due to the TOF expansion, we include an approximate TOF correction to the cloud centre-of-mass position in our numerical simulations. In particular, we use the simulated COM momentum p_{com} to find the semiclassical cloud velocity, and then shift the simulated cloud COM at each timestep[37].

To further characterise our experimental results, we plot in Fig. 2(a) the values of the oscillation frequency obtained by fitting our data for different detunings. As can be seen, for both experiment and numerics, the frequency increases linearly with detuning, as expected from the analytical Bloch-oscillation frequency (*green line*) given by $f_B = |\Delta|/2\pi$ in both real and synthetic space [c.f. Eq. 5]. The trapping frequency is determined by shifting a linear fit to the measured oscillation frequencies to pass through $(|\Delta|, f) = (0, 0)$. This provides a straightforward way to measure the trapping frequency, but does mean that any systematic uncertainty would not be detected.

In Fig. 2(b) we show how the amplitude of the real-space motion depends on the detuning by plotting the amplitude fitting parameters. As can be seen, the experiment (*orange/black*) and numerics (*blue*) both clearly show the expected growth in the real-space amplitude as the detuning decreases and higher-excited atomic trap states are explored. To make a quantitative comparison with semiclassical Bloch oscillations (Eq. 5), we have derived an analytical expression (see Appendix D and Supplemental Material[37]) that converts the expected Bloch oscillation amplitude from synthetic space to real space under appropriate assumptions, including a correction for the finite fraction of atoms participating in the dynamics, as discussed further below. The expression is based on the formula:

$$x_{\text{com}} = \sqrt{\lambda_{\text{com}} - \sigma_x^2 + \frac{1}{2}}, \tag{7}$$

which connects the real space cloud COM x_{com} and width σ_x to the synthetic space COM λ_{com} under certain assumptions. This result is derived in the Supplemental Material[37]. This analytical prediction is plotted in Fig. 2(b) (*green*), with errors calculated from our numerical parameters. As can be seen, there is agreement between the experiment, numerics and the analytics, demonstrating that we have achieved good control of the synthetic-dimension Bloch oscillations.

We can also independently increase the number of atomic trap states explored (i.e. the Bloch oscillation amplitude) while keeping the oscillation frequency constant, by increasing the shaking power, V_0, and hence

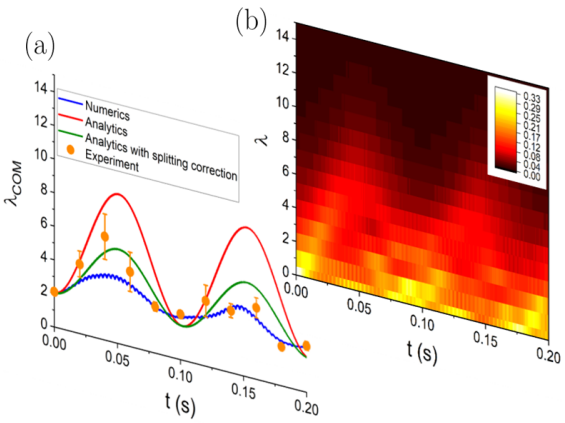

FIG. 4. **Example Bloch oscillation in synthetic space.** (a): Evolution of the COM, λ_{com}, and the numerical density distribution heatmap along the synthetic dimension (b) for the same data as Fig. 1(b), for $\varphi = 0$. Both Bloch oscillations and high-frequency micromotion are visible in the 2D numerics (*blue line*) for a non-interacting thermal cloud[37]. We also convert the corresponding real space experimental data to synthetic space under suitable assumptions (see Appendix E). The observed Bloch oscillation frequency is in good agreement with the 1D analytical semiclassics (Eq. 5, *red line*), albeit with a lower amplitude as only around half the atoms from the thermal cloud oscillate along the synthetic dimension [c.f. density distribution heatmap in (b)]. To correct for this, the analytical result is rescaled (*green line*) as discussed in the text. The heatmap shows the numerical atomic density (integrated along the y direction) with respect to λ over the oscillation, showing the cloud-splitting. Both panels use experimental parameters of $\omega_x = 166.5 \times 2\pi$ Hz, $\Delta = 2\pi \times 9.84$ Hz, $V_0 = 4.16$ nK, $T = 20$ nK, and $\omega_y = 10 \times 2\pi$ Hz. Experimental errorbars are 1σ statistical errors.

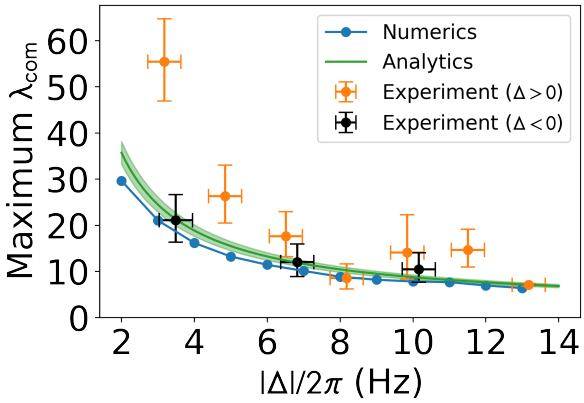

FIG. 5. **Bloch oscillation amplitude in synthetic space.** The extrapolated maximum value of λ reached by the oscillating part of the cloud as a function of Δ, demonstrating that we have a long, controllable synthetic dimension. As discussed in Appendix E, we convert the experimental fit parameters in Fig. 2(b) to synthetic space (*orange/black*), correcting for cloud splitting. We also plot our numerical maximum λ values (*blue*) for $\varphi = 0$, again corrected for cloud splitting. Furthermore, we derive appropriate analytics (*green*) for comparison (see Appendix D). Error bars on experimental points were calculated by converting the real space errors to synthetic space, while the error bars on the analytics were found by propagating errors on J and other numerical parameters. We use experimental parameters of $\omega_x = 166.5 \times 2\pi$ Hz, $V_0 = 4.16$ nK, $T = 20$ nK, and $\omega_y = 10 \times 2\pi$ Hz.

the hopping parameter J [c.f. Eq. 4]. The dependence of the real-space COM amplitude on V_0 is shown in Fig. 3(a) for a fixed detuning $\Delta = 8.3 \times 2\pi$ Hz, while the inset shows the variation of the hopping J, as calculated with Floquet theory[37]. As can be seen, the amplitude in experiment (*orange*), numerics (*blue*) and analytics (*green*) all increase as the hopping increases [c.f. Eq. 5]. Note that the analytical result is only plotted for $V_0 \leq 4$ nK, as at higher shaking powers, our simple analytical model (Eq. 4) breaks down (see Supplemental Material[37]). Despite this, we still observe clear Bloch oscillation dynamics at high power. This is further demonstrated in Fig. 3(b), where we use a very strong potential of $V_0 = 11.96$ nK, and still observe the same qualitative trends (i.e. the amplitude decreasing with the detuning and the frequency being equal to the detuning) as in the low power regime. Finally, we can visualise the Bloch oscillations along the synthetic dimension more directly, by translating our real-space experimental measurements [from Fig. 1(c)] into λ-space, under suitable approximations (see Appendix E). These experimental results are plotted in Fig. 4(a) (*orange*), along with numerical simulations (*blue curve*). Note that the latter is not averaged over different initial driving phases; however, in synthetic space, the micromotion is only a fraction of a "lattice spacing" and becomes negligible as the trapping frequency ω_x increases[20].

We also compare our experimental results directly with the semiclassical analytical predictions [Eq. 5] with (*green curve*) and without (*red curve*) multiplying by a constant numerical re-scaling factor to account for the fraction of atoms contributing to the dynamics[37]. This correction was also used in Fig. 2 and 3 and is necessary because the COM is skewed downwards by the thermal cloud splitting into two distinct parts, with approximately half of the atoms remaining in low λ-states during the oscillation, as can be seen in the numerical density distribution heatmap in Fig. 4(b). This effect is likely caused by small oscillations in the Floquet Hamiltonian matrix elements, and we discuss methods to reduce this splitting effect in the Supplemental Material[37].

Importantly, we can also convert our experimental amplitude fit parameters (Fig. 2(b)) to synthetic space and divide by the constant numerical cloud splitting factor in order to extrapolate how far up λ the oscillating part of the cloud is actually exploring (see Appendix E). This is plotted in Fig. 5 (*orange/black*), where we can see that the fraction of the cloud involved in the Bloch oscillations is moving up several tens of Bloch states, demonstrating

that we are creating a very long synthetic dimension. This is supported by our numerical (*blue*) and analytical results (*green*) (see Appendices C and D). Note that the number of sites along the synthetic dimension will eventually be limited experimentally by anharmonicities in the trapping potential[20]; however, in this experiment, this does not play an important role. We included the appropriate quartic anharmonic terms in our numerical simulations and found that they had no effect in the range of trap states that are relevant here. We discuss the properties of the excited states we create, and methods to improve their fidelity, in the Supplemental Material[37]. Finally, we note that our methods can be extended towards single-site resolution to on the order of or below $\hbar\omega_x/k_B$. That would start the dynamics with only the $\lambda = 0$ state populated. The subsequent dynamics would maintain the single λ-state character. This point is discussed further in the Supplemental Material[37].

IV. CONCLUSIONS

Our experimental results show that we have engineered a synthetic dimension of atomic trap states by projecting a time-dependent shaking potential onto an atomic cloud via a digital micro-mirror device. Through control of the shaking potential's detuning, we induced Bloch oscillations along the synthetic dimension, observing the key characteristics of these dynamics in the real-space motion of the cloud. Our experiment demonstrates that a long and controllable synthetic dimension can be created. This opens up the way towards the exploration of topological physics using a synthetic dimension of harmonic trap states[20,21] by introducing a controllable artificial gauge field using a spatially-varying shaking phase. The spatio-temporal control of the shaking potential can also allow for future investigations of phenomena such as magnetic barriers, as well as the controlled population of excited atomic trap states, including direct imaging of the states[38] and single-site resolution of our current methods[37]. Moreover, the addition of mean-field interactions in the cloud should lead to exotic interactions along the synthetic dimension[20] and, in turn, interesting ground state physics.

APPENDIX A: EXPERIMENT

In our experimental sequence we load ^{87}Rb atoms from a 3d MOT into a crossed optical dipole trap and then perform forced evaporative cooling[39]. The final trapping frequencies are $f_x = f_z \simeq 160$ Hz, and $f_y \simeq 10$ Hz, where z is the vertical axis, resulting in a cloud elongated along y, with $N \simeq 2 \times 10^4$ atoms at $\simeq$20 nK. We conclude a posteriori that the degeneracy of the x and z trapping directions does not affect the dynamics because of the good agreement between theory and experimental data. We also verified using horizontal imaging that there are no significant dynamics along the z-direction. The optical setup to realise the dynamical potential and high resolution imaging is described in detail in Ref. 40. In brief, the light produced by a 800 nm laser is reflected by a DMD and then sent onto the atoms along the vertical direction, using an optical setup that produces a demagnification of a factor 100. The DMD is an 2d array of 1920×1080 micromirrors, each with size 10.8 μm. Each micromirror can be individually tilted every 100 μs, allowing us to produce dynamical optical potentials. The atoms are imaged on a CCD mounted in the vertical direction using a 20$\times$ magnifying system with a resolution of $\simeq 2$ μm. The numerical aperture of our imaging system is 0.28. We verify the alignment between the driving and trapping potentials to a precision of $\simeq$1 μm by imaging both the cloud and the DMD pattern at once. This was done every 20 runs to avoid slow drifts. We also note that we do not observe significant heating of the cloud due to the driving potential. We determine this by observing the width of the cloud in the weak trapping direction after a short TOF expansion and finding that it does not change, as shown by experimental data in Fig. S11[37]. This is caused by any "heated" atom spilling out of the weak trap, leading to some atom loss but a fixed temperature.

APPENDIX B: REAL SPACE EXPERIMENTAL DATA ANALYSIS

To reduce micromotion effects, the experimental data for the real-space COM position is RMS-averaged over initial driving phases drawn randomly from $2\pi n/30$, with $n = 0, 1, ...30$. (The effects of RMS-averaging are discussed further in the Supplemental material[37].) The resulting data are then fitted to the function:

$$x(t) = A\sqrt{1 - e^{-gt}\cos(2\pi f t + \phi)}, \tag{8}$$

where A is the amplitude, f is the frequency, g is a damping factor and ϕ is a phase offset which accounts for random variation in the state preparation. The functional form of this fitting function is motivated by translating the semiclassical prediction for synthetic-dimension Bloch oscillations (Eq. 5) into real space. As shown in the Supplemental Material[37], under certain approximations, this conversion can be achieved by taking:

$$x_{\mathrm{com}} = \sqrt{\lambda_{\mathrm{com}} - \sigma_x^2 + \frac{1}{2}}, \tag{9}$$

where x_{com} and σ_x are, respectively, the COM and width of the cloud (in harmonic oscillator lengths) with respect to the real position coordinate, x. Note that in choosing the form of the fitting function, we assume that the cloud width σ_x is approximately constant as a function of time, as has also been verified numerically[37]. The fitting parameters f and A are then plotted, for example, in Fig. 2(a) and (b) respectively.

APPENDIX C: NUMERICAL SIMULATIONS AND DATA ANALYSIS

We perform our simulations by time-evolving an appropriate initial state using the time-dependent Hamiltonian in Eq. 3 in the main text, where we also include weak-trap dynamics (i.e. terms that depend on y). We simulate the dynamics of a non-interacting thermal cloud by using an initial state of the form $|\psi_\theta\rangle = A\sum_{i=0}^{N-1}\sqrt{p_i}\exp(i\theta_i)|\phi_i\rangle$, where A is a normalisation factor, $p_i = \exp(-\beta E_i)/Z$ is the Boltzmann weight for the i^{th} eigenstate of the 2D harmonic trap $|\phi_i\rangle$ with energy E_i, β is the inverse temperature, Z is the partition function for the 2D harmonic trap and θ_i is a random phase drawn from a uniform distribution between 0 and 2π. We choose the first N states of the 2D harmonic trap, and we check that the Boltzmann weight is small enough that this is a good approximation. We sequentially generate N' such states, each with a different set of random phases, and then time-evolve each separately. The resulting densities are then averaged together which, as we show in the Supplemental Material[37], reproduces the density of a thermal cloud at $t = 0$.

From our numerical simulations, we obtain the cloud density in either synthetic space $\rho(\lambda, y, t)$ or real-space $\rho(x, y, t)$. From these densities, we can then calculate the COM position as a function of time with respect to λ and x respectively. The former is plotted in Fig. 4(a), while the latter requires additional processing steps to be compared with experiment. Firstly, to account for the experimental TOF expansion of the cloud, we apply a correction as $\tilde{x}_{\text{com}} = x_{\text{com}} + v_{\text{com}}t_{\text{tof}}$, where the COM velocity v_{com} is calculated from the numerical momentum distribution. Secondly, we RMS average the M different corrected centres-of-mass together to remove the micromotion: $\langle\tilde{x}_{\text{com}}\rangle = \sqrt{\frac{1}{M}\sum_{i=1}^{M}(\tilde{x}_{\text{com}}^{(i)})^2}$. For the numerics shown in the main text, we take $M = 2$ with $\varphi = 0$ and $\varphi = \pi/2$, as justified further in the Supplemental Material[37]. Finally, we fit our data with the experimental fitting function [Eq. 8], although now with $\phi = 0$ as numerically there are no random variations in the state preparation. The corresponding fitting parameters f and A for the numerical data are then plotted, for example, in Fig. 2(a) and (b) respectively.

APPENDIX D: ANALYTICAL RESULTS

The semiclassical prediction for synthetic-dimension Bloch oscillations is given by Eq. 5 in the main text. In order to plot this analytical result, we independently calculate the nearest-neighbour hopping $J/\hbar = 106\pm8$Hz from Floquet theory[37]. When calculating this hopping, we observe that the hopping is independent of the detuning, and that each hopping is nearly independent of λ, except for small oscillations. We therefore calculate the error bar by adding the standard deviations of the hopping for each Δ in quadrature. Note that this value applies to our low-power data only; in the high-power case, we have significant long-range hoppings so we can no longer use this nearest-neighbour tight binding model. Note also that, in practice, only a fraction of atoms participates in the dynamics, which leads to a significant reduction in the apparent COM position in both synthetic and real space, as shown in Fig. 4. To account for this, we modify Eq. 5 to $\lambda_{\text{com}}(t) = \lambda_{\text{com}}^0 + r\frac{2J}{\hbar\Delta}(1-\cos(\Delta t))$. Here, $r = 0.52 \pm 0.03$ is the average cloud fraction that undergoes the oscillation, as calculated from our numerics for the low power data, where the error bar is the standard deviation of the different r values for different detunings. Note that we discuss methods to reduce the cloud splitting effect in the Supplemental Material[37].

To translate the analytical result from synthetic space to real space, we make use of the conversion formula [Eq. 9] under the assumption that the real-space cloud width stays constant as a function of time. This leads to the expression (see Supplemental Material[37]):

$$x_{\max} = \frac{1}{\sqrt{2}}\alpha_{\text{rms}}\alpha_{\text{tof}}\sqrt{\frac{\hbar}{m\omega_x}}\sqrt{\lambda_{\text{com}}^0 + r\frac{4J}{\hbar\Delta} - \sigma_x^2 + \frac{1}{2}}. \tag{10}$$

where we have included corrections for the reduction in amplitude due to RMS averaging, $\alpha_{\text{rms}} = 1/\sqrt{2}$, and for the TOF expansion, $\alpha_{\text{tof}} = 5.25\pm0.08$, as calculated from our low-power numerics with an error bar corresponding to the standard deviation across multiple detunings. Note that the cloud width σ_x is here measured in harmonic oscillator lengths $\sqrt{\hbar/m\omega_x}$. This result is then plotted, for example, in Fig. 2(b).

APPENDIX E: SYNTHETIC DIMENSION EXPERIMENTAL DATA ANALYSIS AND THEORETICAL RESULTS

To convert our real space experimental oscillation into synthetic space (Fig. 4(a)), we use our conversion formula (Eq. 9), assuming that the real space width σ_x (measured in harmonic oscillator lengths) remains constant in time and set by the trap frequency and initial temperature. We then obtain:

$$\lambda_{\text{com}}(t) = \left(\frac{x_{\text{com}}(t)}{\alpha_{\text{rms}}\alpha_{tof}}\right)^2 + \sigma_x^2 - \frac{1}{2}, \tag{11}$$

where $x_{\text{com}}(t)$ is the experimental real space COM measured in harmonic oscillator lengths. The conversion for the data in Fig. 5 is similar, but here we convert the experimental amplitude fitting parameters, so we use the conversion:

$$\lambda_{\text{com}} = \left(\left(\frac{x_{\text{com}}}{\alpha_{\text{rms}}\alpha_{tof}/\sqrt{2}}\right)^2 + \sigma_x^2 - \frac{1}{2}\right)/r, \tag{12}$$

This is then compared against the corresponding numerics, where we extract the maximum value of λ_{com}

and rescale by $1/r$ to account for the cloud splitting. We also compare against an analytical expression, $\lambda_{\rm com} = \lambda_0 + 4J/\hbar\Delta$, as shown in Fig. 5.

Note Added: We note that Bloch oscillations of driven dissipative solitons were recently detected in a photonics synthetic dimension[41].

ACKNOWLEDGMENTS

We would like to acknowledge helpful discussions with Bruno Peaudecerf, David Guéry-Odelin, Tilman Esslinger, Laura Corman and Jean-Philippe Brantut. We acknowledge financial support by the Royal Society via grants UF160112, RGF\EA\180121 and RGF\R1\180071, and the EPSRC via grant EP/R021236/1. N.G. is supported by the ERC Starting Grant TopoCold and the Fonds De La Recherche Scientifique (FRS-FNRS, Belgium). G.S. was supported by the ERC Starting Grant TopoCold, the Academy of Finland under project numbers 327293, and the European Union's Horizon 2020 research and innovation programme under the Marie Skłodowska-Curie grant agreement No 101025211 (TEBLA).

A.S. and T.E. carried out the experiment under the guidance and supervision of V.G. and G.B. The theoretical analysis was performed by C.O., under the guidance and supervision of G.S., N.G. and H.M.P. The project was conceived and designed by N.G., H.M.P and G.B. The manuscript was drafted by C.O. and then revised by all authors.

[1] O. Boada, A. Celi, J. I. Latorre, and M. Lewenstein, "Quantum simulation of an extra dimension," Phys. Rev. Lett. **108**, 133001 (2012).
[2] A. Celi, P. Massignan, J. Ruseckas, N. Goldman, I. B. Spielman, G. Juzeliūnas, and M. Lewenstein, "Synthetic gauge fields in synthetic dimensions," Phys. Rev. Lett. **112**, 043001 (2014).
[3] M. Mancini, G. Pagano, G. Cappellini, L. Livi, M. Rider, J. Catani, C. Sias, P. Zoller, M. Inguscio, M. Dalmonte, and L. Fallani, "Observation of chiral edge states with neutral fermions in synthetic Hall ribbons," Science **349**, 1510–1513 (2015).
[4] B. K. Stuhl, H.-I. Lu, L. M. Aycock, D. Genkina, and I. B. Spielman, "Visualizing edge states with an atomic Bose gas in the quantum Hall regime," Science **349**, 1514–1518 (2015).
[5] L. F. Livi, G. Cappellini, M. Diem, L. Franchi, C. Clivati, M. Frittelli, F. Levi, D. Calonico, J. Catani, M. Inguscio, and L. Fallani, "Synthetic dimensions and spin-orbit coupling with an optical clock transition," Phys. Rev. Lett. **117**, 220401 (2016).
[6] S. Kolkowitz, S. Bromley, T. Bothwell, M. L. Wall, G. E. Marti, A. P. Koller, X. Zhang, A. M. Rey, and J. Ye, "Spin–orbit-coupled fermions in an optical lattice clock," Nature **542**, 66 – 70 (2017).
[7] T. Chalopin, T. Satoor, A. Evrard, V. Mahkalov, J. Dalibard, R. Lopes, and S. Nascimbene, "Probing chiral edge dynamics and bulk topology of a synthetic hall system." Nat. Phys. **16**, 1017–1021 (2020).
[8] V. Lienhard, P. Scholl, S. Weber, D. Barredo, S. de Léséleuc, R. Bai, N. Lang, M. Fleischhauer, H.P. Büchler, T. Lahaye, and A. Browaeys, "Realization of a density-dependent Peierls phase in a synthetic, spin-orbit coupled Rydberg system," Phys. Rev. X **10**, 021031 (2020).
[9] S. K. Kanungo, J. D. Whalen, Y. Lu, M. Yuan, S. Dasgupta, F. B. Dunning, K. R. A. Hazzard, and T. C. Killian, "Realizing Su-Schrieffer-Heeger topological edge states in Rydberg-atom synthetic dimensions," (2021), arXiv:2101.02871 [physics.atom-ph].
[10] E. Meier, F. An, and B. Gadway, "Observation of the topological soliton state in the Su–Schrieffer–Heeger model," Nat. Commun. **7**, 13986 (2016).
[11] K. Viebahn, M. Sbroscia, E. Carter, J. Yu, and U. Schneider, "Matter-wave diffraction from a quasicrystalline optical lattice," Phys. Rev. Lett. **122**, 110404 (2019).
[12] H. Cai, J. Liu, J. Wu, Y. He, S. Zhu, J. Zhang, and D. Wang, "Experimental observation of momentum-space chiral edge currents in room-temperature atoms," Phys. Rev. Lett. **122**, 023601 (2019).
[13] B. Sundar, B. Gadway, and K.R.A. Hazzard, "Synthetic dimensions in ultracold polar molecules." Sci. Rep. **8**, 3422 (2018).
[14] Jin Hyoun Kang, Jeong Ho Han, and Yi Shin, "Creutz ladder in a resonantly shaken 1d optical lattice," New Journal of Physics **22**, 013023 (2020).
[15] Fangzhao Alex An, Bhuvanesh Sundar, Junpeng Hou, Xi-Wang Luo, Eric J. Meier, Chuanwei Zhang, Kaden R. A. Hazzard, and Bryce Gadway, "Nonlinear dynamics in a synthetic momentum-state lattice," Phys. Rev. Lett. **127**, 130401 (2021).
[16] E. Lustig, S. Weimann, Y. Plotnik, Y. Lumer, M.A. Bandres, A. Szameit, and M. Segev, "Photonic topological insulator in synthetic dimensions," Nature **567**, 356–360 (2019).
[17] A. Dutt, Q. Lin, L. Yuan, M. Minkov, M. Xiao, and S. Fan, "A single photonic cavity with two independent physical synthetic dimensions," Science **367**, 59–64 (2020).
[18] A. Balčytis, T. Ozawa, Y. Ota, S. Iwamoto, J. Maeda, and T. Baba, "Synthetic dimension band structures on a Si CMOS photonic platform," (2021), arXiv:2105.13742 [physics.optics].
[19] H. Chen, N. Yang, C. Qin, W. Li, B. Wang, T. Han, C. Zhang, W. Liu, K. Wang, H. Long, X. Zhang, and Lu. Peixiang, "Real-time observation of frequency Bloch oscillations with fibre loop modulation," Light Sci. Appl. **10**, 1–9 (2021).
[20] H.M. Price, T. Ozawa, and N. Goldman, "Synthetic dimensions for cold atoms from shaking a harmonic trap," Phys. Rev. A **95**, 023607 (2017).
[21] G. Salerno, H. M. Price, M. Lebrat, S. Häusler, T. Esslinger, L. Corman, J.-P. Brantut, and N. Goldman, "Quantized Hall conductance of a single atomic wire: A

proposal based on synthetic dimensions," Phys. Rev. X **9**, 041001 (2019).
[22] K. Wang, A. Dutt, Y.Y. Yang, C.C. Wojcik, J. Vučković, and S. Fan, "Generating arbitrary topological windings of a non-hermitian band," Science **371**, 6535 (2021).
[23] E.J. Meier, F.A. An, A. Dauphin, M. Maffei, P. Massignan, T.L. Hughes, and B. Gadway, "Observation of the topological Anderson insulator in disordered atomic wires," Science **362**, 929–933 (2018).
[24] H. M. Price, O. Zilberberg, T. Ozawa, I. Carusotto, and N. Goldman, "Four-dimensional quantum Hall effect with ultracold atoms," Phys. Rev. Lett. **115**, 195303 (2015).
[25] G. Wirth, M. Ölschläger, and A. Hemmerich, "Evidence for orbital superfluidity in the P-band of a bipartite optical square lattice," Nat. Phys. **7**, 147 (2011).
[26] T. Müller, S. Fölling, A. Widera, and I. Bloch, "State preparation and dynamics of ultracold atoms in higher lattice orbitals," Phys. Rev. Lett. **99**, 200405 (2007).
[27] X. Li and W.V. Liu, "Physics of higher orbital bands in optical lattices: a review," Rep. Prog. Phys. **79**, 116401 (2016).
[28] D. Hu, L. Niu, S. Jin, X. Chen, G. Dong, J. Schmiedmayer, and X. Zhou, "Ramsey interferometry with trapped motional quantum states," Commun. Phys. **1**, 29 (2018).
[29] S. van Frank, A. Negretti, T. Berrada, R. Bücker, S. Montangero, J.-F. Schaff, T. Schumm, T. Calarco, and J. Schmiedmayer, "Interferometry with non-classical motional states of a Bose–Einstein condensate," Nat. Commun. **5**, 4009 (2014).
[30] V Guarrera, R Szmuk, J Reichel, and P Rosenbusch, "Microwave-dressed state-selective potentials for atom interferometry," New J. Phys. **17**, 083022 (2015).
[31] S. Vinjanampathy and J. Anders, "Quantum thermodynamics," Contemp. Phys. **57**, 545–579 (2016).
[32] H. T. Quan, Yu-xi Liu, C. P. Sun, and Franco Nori, "Quantum thermodynamic cycles and quantum heat engines," Phys. Rev. E **76**, 031105 (2007).
[33] R. Uzdin, A. Levy, and R. Kosloff, "Equivalence of quantum heat machines, and quantum-thermodynamic signatures," Phys. Rev. X **5**, 031044 (2015).
[34] M. Ben Dahan, E. Peik, J. Reichel, Y. Castin, and C. Salomon, "Bloch oscillations of atoms in an optical potential," Phys. Rev. Lett. **76**, 4508–4511 (1996).
[35] C. Bersch, G. Onishchukov, and U. Peschel, "Experimental observation of spectral Bloch oscillations," Opt. Lett. **34**, 2372–2374 (2009).
[36] J. Floß, A. Kamalov, I. Sh. Averbukh, and P.H. Bucksbaum, "Observation of Bloch oscillations in molecular rotation," Phys. Rev. Lett. **115**, 203002 (2015).
[37] See Supplemental Material.
[38] M. Scherer, B. Lücke, J. Peise, O. Topic, G. Gebreyesus, F. Deuretzbacher, W. Ertmer, L. Santos, C. Klempt, and J. J. Arlt, "Spontaneous symmetry breaking in spinor Bose-Einstein condensates," Phys. Rev. A **88**, 053624 (2013).
[39] D.B. Orenes, A.U. Kowalczyk, E. Witkowska, and G. Barontini, "Exploring the thermodynamics of spin-1 Bose gases with synthetic magnetization," New J. Phys. **21**, 043024 (2019).
[40] A. Smith, T. Easton, V. Guarrera, and G. Barontini, "Generation of optical potentials for ultracold atoms using a superluminescent diode," Phys. Rev. Research **3**, 033241 (2021).
[41] N. Englebert, N. Goldman, M. Erkintalo, Mostaan N., S. Gorza, F. Leo, and J. Fatome, "Bloch oscillations of driven dissipative solitons in a synthetic dimension," (2021)
.

Supplemental Material for "Bloch Oscillations Along a Synthetic Dimension of Atomic Trap States"

Christopher Oliver,[1] Aaron Smith,[1] Thomas Easton,[1] Grazia Salerno,[2] Vera Guarrera,[1] Nathan Goldman,[3] Giovanni Barontini,[1] and Hannah M. Price[1]

[1] *School of Physics and Astronomy, University of Birmingham, Edgbaston, Birmingham B15 2TT, United Kingdom*
[2] *Department of Applied Physics, School of Science, Aalto University, Espoo, Finland*
[3] *Center for Nonlinear Phenomena and Complex Systems, Université Libre de Bruxelles (U.L.B.), B-1050 Brussels, Belgium*

(Dated: March 2, 2023)

In Section I, we discuss the details of our numerical results, covering the method used in our simulations. In Section II we describe the data analysis needed to extract the Bloch oscillation amplitude and frequency. We then discuss our analytical results: Section III shows the derivation of the conversion formula between synthetic and real space; Section IV shows how we arrive at the Floquet Hamiltonian in the main text by numerical calculation of its matrix elements; and in Section V we show how the analytical results used in the main text were obtained. Finally, in Section VI we report the experimental results concerning the creation of atomic samples in highly excited harmonic states, and comment on methods to improve the fidelity of these states.

I. DETAILS OF NUMERICAL SIMULATIONS

As shown in the main text, we numerically simulate the motion of a thermal cloud in two dimensions under the time-dependent Hamiltonian $\hat{H}(t)$ (Eq. 2 in the main text, with the y-terms restored). In so doing, we choose to work in the $\lambda - y$ basis; this avoids discretising the x-direction and hence reduces the size of the matrix representing the Hamiltonian in the numerics. From our numerical simulation of the wave-function, we then calculate the cloud density $\rho(\lambda, y, t)$, and convert this into real space to yield $\rho(x, y, t)$. The time evolution of the wave-function is done by numerically time-evolving an appropriate initial state as:

$$|\psi(t+dt)\rangle = \exp\left(-\frac{i\hat{H}(t)dt}{\hbar}\right)|\psi(t)\rangle\,, \tag{S1}$$

where dt is a sufficiently small timestep. In order to simulate the dynamics of a non-interacting thermal cloud (i.e. a non-interacting gas which is distributed over the levels of the trap according to a classical Boltzmann distribution), we choose an initial state of the form [S1, S2]:

$$|\psi_\theta\rangle = A\sum_{i=0}^{N-1}\sqrt{p_i}\exp\left(i\theta_i\right)|\phi_i\rangle\,, \tag{S2}$$

where A is a normalisation factor, $p_i = \exp\left(-\beta E_i\right)/Z$ is the Boltzmann weight for the i^{th} eigenstate of the 2D harmonic trap $|\phi_i\rangle$ with energy E_i, β is the inverse temperature, Z is the partition function for the 2D harmonic trap and θ_i is a random phase drawn from a uniform distribution between 0 and 2π. Note that a finite number, N, of harmonic trap states is used in this construction; in order to safely neglect higher-energy trap states, we check numerically that the Boltzmann weight has decayed to a sufficiently small value.

In the numerics, we then sequentially generate N' such random phase states, each with a different set of random phases. Each state is then time-evolved and the resultant densities are averaged together. By averaging over random phase factors, we destroy the phase coherence of the state; omitting this step would correspond to selecting a particular (and likely unphysical) coherent superposition of trap states. To further illustrate the importance of the random-phase averaging, we show how this can reproduce the expected density for a thermal cloud at $t = 0$. The latter can be found from the system's density matrix $\hat{\rho} = \sum_i p_i\,|\phi_i\rangle\langle\phi_i|$, as:

$$\rho(\mathbf{r}) = \langle\mathbf{r}|\,\hat{\rho}\,|\mathbf{r}\rangle = \sum_i p_i|\phi_i(\mathbf{r})|^2, \tag{S3}$$

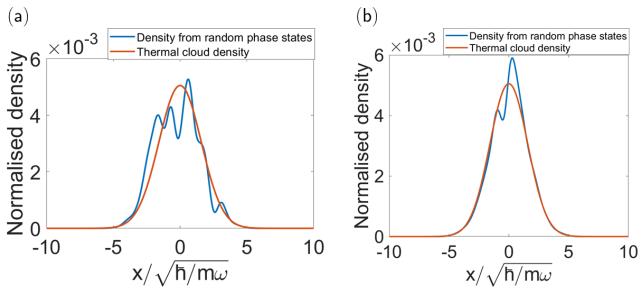

FIG. S1. The 1D atomic density obtained from random-phase-state averaging (*blue*) compared to the known density of a thermal cloud (*red*) (Eq. S7) with temperature $T = 20$nK in a harmonic trap of frequency $\omega_x = 2\pi \times 166.5$ Hz, and $N = 16$. In (a), we average over 5 random phase states, and in (b) over 100 states. As can be seen, (a) shows significant fluctuations which decrease with averaging over more states, as shown in (b).

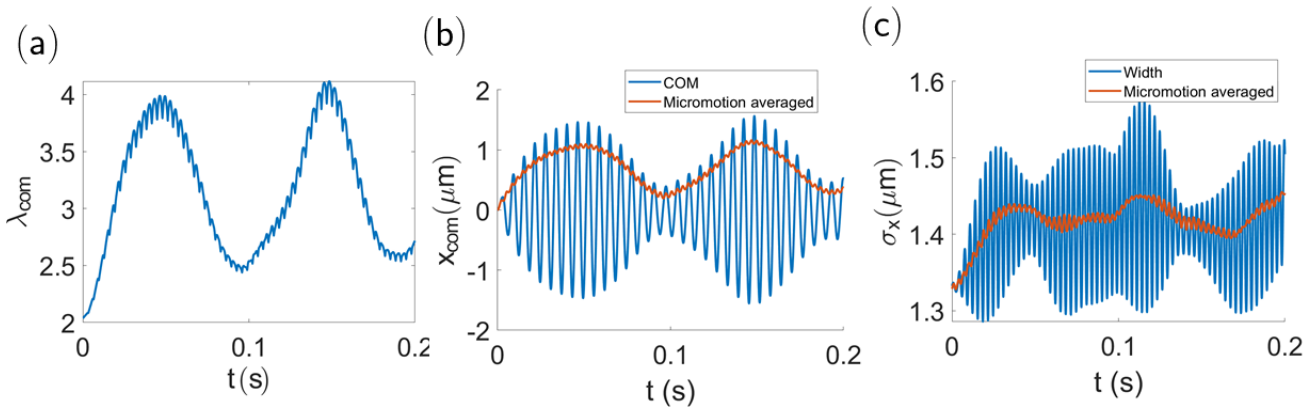

FIG. S2. Example unprocessed data from the numerical simulations corresponding to Fig. 1(b) and 3(a) and (b) in the main text. (a): synthetic dimension COM as a function of time for $\varphi = 0$, showing the Bloch oscillation and micromotion. (b): real space COM, also showing micromotion under the Bloch oscillation envelope (*blue*), together with the root-mean-square average over a pair of initial driving phases 0 and $\pi/2$ (*red*). (c): real space cloud width (*blue*) and its micromotion average (*red*), which is approximately constant in time to one decimal place. The phase-averages are used in Section V to verify the result derived there. We use the parameters: $V_0 = 4.16$ nK, $\omega_x = 166.5 \times 2\pi$ Hz, $\Delta = 9.84 \times 2\pi$ Hz, $\omega_y = 10 \times 2\pi$ Hz, $T = 20$ nK, as in Fig. 1, 2, 3 and 4 in the main text.

where $\phi_i(\mathbf{r}) = \langle \mathbf{r}|\phi_i\rangle$ [S3]. We can also calculate the density of the random phase state as:

$$\begin{aligned}\rho_\theta(\mathbf{r}) &= \langle\psi_\theta|\mathbf{r}\rangle\langle\mathbf{r}|\psi_\theta\rangle \\ &= \sum_{ij}\sqrt{p_i p_j}\exp\left(i(\theta_i-\theta_j)\right)\langle\phi_j|\mathbf{r}\rangle\langle\mathbf{r}|\phi_i\rangle. \end{aligned} \tag{S4}$$

which, as can be seen, involves a double sum over the harmonic trap states. However, averaging over the random phases gives:

$$\rho(\mathbf{r}) = \frac{1}{(2\pi)^{N'}}\int_0^{2\pi}\prod_{i=1}^{N'} d\theta_i \rho_\theta(\mathbf{r}) = \sum_i p_i|\phi(\mathbf{r})|^2, \tag{S5}$$

as desired, where we used the identity:

$$\int_0^{2\pi}\exp\left(i(\theta_i-\theta_j)\right)d\theta_i = 2\pi\delta_{ij}. \tag{S6}$$

The random phase state therefore reproduces the density for a thermal cloud at $t = 0$ under suitable averaging.

We can also demonstrate the effects of phase-averaging numerically as shown in Figure S1, where this technique is applied to a 1D harmonic trap for (a) only five random phase states and (b) for 100 random phase states. In both cases, the blue curve is the density calculated via the above method and the orange curve is the expected thermal cloud density calculated explicitly as:

$$\rho(x) = Ae^{-\frac{x^2}{2\sigma^2}}, \tag{S7}$$

where A is a normalisation constant and $\sigma = k_B T/m\omega_x^2$ is the cloud width, controlled by the trap frequency and temperature [S3]. For large enough numbers of random phases states included in the average (Fig. S1(b)), we see good agreement with the expected thermal cloud density. Note that in so doing, we have assumed that our cloud is non-interacting, because if interactions are present, we can no longer use a Boltzmann-weighted superposition over single-particle trap states. Throughout this work, we use 50 random phase states in our numerics.

II. DETAILS OF DATA ANALYSIS

Here we describe the data analysis steps carried out on the simulated cloud density (Section I) in order to extract the Bloch oscillation frequency and amplitude, which we have then compared to experiment and analytical results in the main text.

Firstly, the cloud center-of-mass (COM) and width are calculated from the real space cloud density $\rho(x, y, t)$, found using the method in Section I. An example is shown in Fig. S2, where we see oscillations in both the synthetic and real space COM ((a) and (b) respectively), including high-frequency micromotion, as discussed in the main text. Note that the λ-space COM is calculated as $\lambda_{\text{com}} = \sum_\lambda \lambda\rho(\lambda, t)$, where $\rho(\lambda, t)$ is the probability density with respect to the synthetic dimension, calculated numerically as in Section I, with the y-dependence integrated out. We also see that, although the cloud does visit higher harmonic oscillator states, the cloud width (panel (c)) is approximately constant in time. We use this observation in Section V to simplify our analysis. Throughout this section, we use the typical experimental parameters: $V_0 = 4.16$ nK, $\omega_x = 166.5 \times 2\pi$ Hz, $\Delta = 9.84 \times 2\pi$ Hz, $\omega_y = 10 \times 2\pi$ Hz, $T = 20$ nK and the initial driving phase $\varphi = 0$ for any data including micromotion and $\varphi = 0$ and $\pi/2$ for any data where micromotion has been averaged out, as discussed further below. These

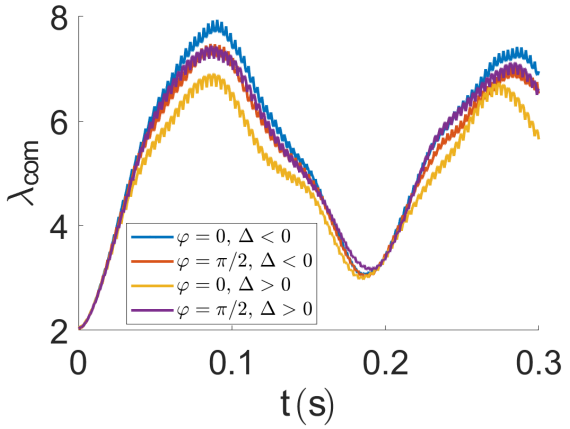

FIG. S3. The effect on the synthetic space dynamics of different signs of the detuning for the two initial driving phases used for all the numerics. For $\varphi = 0$ (*blue* and *yellow*), we see a small difference in oscillation amplitude of around 1 synthetic lattice site for different signs of Δ, whereas for $\varphi = \pi/2$ (*red* and *purple*) the amplitudes are unchanged. We use the same parameters as Fig. S2, but with $|\Delta| = 5 \times 2\pi$ Hz.

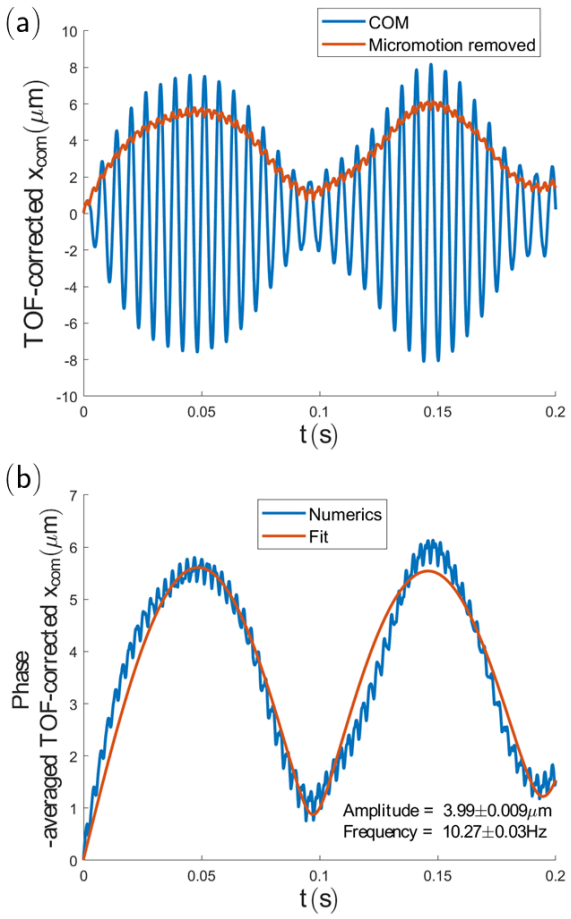

FIG. S4. Steps in the analysis of simulated real space COM data. (a): example real space COM with an applied TOF correction and $\varphi = 0$, showing a larger-magnitude oscillation (*blue*), together with its RMS average over driving phases (*red*), with $\varphi = 0, \pi/2$. The RMS-averaged curve shows a smaller amplitude than the full oscillation. (b): fit of Eq. S10 (*red*) to the TOF-corrected, RMS-averaged example oscillation (*blue*), showing that our fitting function captures the dynamics well. The error bars on the reported fitted amplitude and frequency are those provided by the least-squares fit. These results use identical parameters to Fig. S2, and to Fig. 1(c) and 3 in the main text.

are the same parameters as in Fig. 1, 2, 3 and 4 in the main text. As an aside, we mention the effect of different signs of detuning (i.e. different signs of the effective force) on the dynamics in synthetic space. In Fig. S3, we plot the synthetic space dynamics for both $\varphi = 0$ (*blue* and *yellow*) and $\pi/2$ (*red* and *purple*) for opposite detuning signs. We see that, for $\varphi = 0$, there is a small amplitude difference of around 1 synthetic lattice site, whereas for $\varphi = \pi/2$ the two amplitudes are the same. This means that we expect our oscillation amplitudes to be similar regardless of the sign of Δ, as we find in our results in the main text. Note that the presence of a hard wall boundary at $\lambda = 0$ makes this different to the expected result for a wavepacket prepared in the synthetic dimension bulk. In that case, we expect the wavepacket to move in opposite directions for opposite signs of Δ.

Secondly, we need to take into account the time-of-flight expansion (TOF) carried out in the experiment, as this is not included in the numerical method described in Section I. If this is not accounted for, then the experimental COM oscillations will be significantly larger than in the simulation. To correct for this in the numerics, we use the simulated momentum distribution to calculate the COM momentum in real space, p_{com}, and hence find the semiclassical cloud COM velocity $v_{\mathrm{com}} = p_{\mathrm{com}}/m$ at each time-step, such that we can correct the COM position from the numerics as:

$$\tilde{x}_{\mathrm{com}} = x_{\mathrm{com}} + v_{\mathrm{com}} t_{\mathrm{tof}}, \tag{S8}$$

where t_{tof} is the TOF expansion time, corresponding to 5ms in this experiment. This method applied to our example oscillation (Fig. S2) is shown in Fig. S4(a). We see the same qualitative form as Fig. S2(b), but with an amplitude around five times larger. Thirdly, as discussed above and in the main text, we need to remove the micromotion before we can extract the amplitude and frequency of the Bloch oscillation. Experimentally, this is done by repeating the experiment for multiple different starting phases φ of the driving potential, as discussed in Appendix B. The micromotion is approximately removed by taking the root-mean-square (RMS) average over the M chosen driving phases:

$$\langle \tilde{x}_{\mathrm{com}} \rangle = \sqrt{\frac{1}{M} \sum_{i=1}^{M} (\tilde{x}_{\mathrm{com}}^{(i)})^2}, \tag{S9}$$

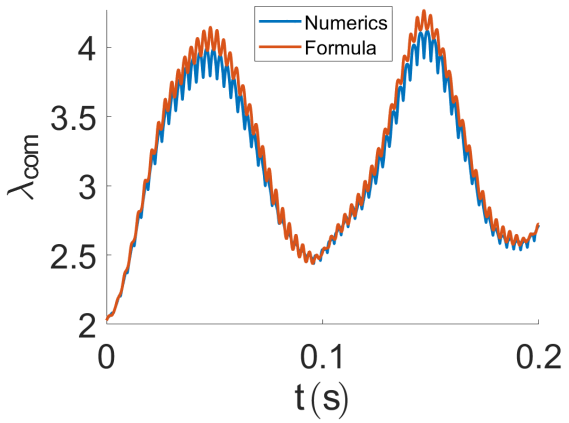

FIG. S5. Example of the conversion formula (Eq. S21, *red*) applied to the same numerical simulation as Fig. S2 (*blue*), showing agreement up to a small offset. The formula is applied using the RMS time-averaged data in Fig. S2(b) and (c).

where $\tilde{x}^{(i)}_{\rm com}$ is the COM for the i-th initial driving phase. Physically, the choice of φ controls the phase of the micromotion oscillations. This approach is applied directly to the experimental data, as well as to the simulated data after the TOF correction.

If the driving phases are chosen randomly or if the micromotion is very complicated, then we expect to take the large M limit in Eq. S9 and average over many experimental or numerical runs. However, if the micromotion were described by a perfectly sinusoidal function, such as e.g. $f(t) = \sin\omega_D t$, then we would in fact only need to average over any two values of φ that are separated by $(2k+1)\pi/2$, with $k = 0, 1, 2...$, using the property that $(f(t))^2 + (f(t+(2k+1)\pi/2))^2 = 1$.

In practice, our numerical simulations (Fig. S4(a) and S2) suggest that the micromotion is close to being sinusoidal and so we try averaging over only one pair of phases related by $(2k+1)\pi/2$. Indeed, Fig. S4(a) shows an example of this RMS-averaged oscillation (*red curve*) over two phases ($\varphi = 0, \pi/2$), together with the $\varphi = 0$ un-averaged data (*blue curve*). As can be seen, averaging over only two runs is already sufficient to remove the majority of the micromotion, with a small residual that could be removed by using more pairs of phases. However, the amplitude of the averaged curve is smaller than the un-averaged result, and we will return to this point later when discussing corrections to the analytical results in Section V. Finally, to extract the oscillation amplitude and frequency, we fit the function:

$$x(t) = A\sqrt{1 - e^{-gt}\cos(2\pi f t + \phi)}, \tag{S10}$$

to the real space COM in both simulation and experiment, as introduced in the main text. This functional form is motivated by the analytical results; if we convert the expected oscillation in synthetic space (Eq. 4 in the main text) to real space (using Eq. 6 in the main text which is derived in Section III below), we obtain:

$$x_{\rm com} = \sqrt{\lambda^0_{\rm com} - \sigma_x^2 + \frac{1}{2} + \frac{2J}{\hbar\Delta}(1 - \cos(\Delta t))}. \tag{S11}$$

Since, in our numerics, $x_{\rm com}(t = 0) = 0$, we have $\lambda^0_{\rm com} - \sigma_x^2 + 1/2 = 0$, where we assume that σ_x is constant in time as justified previously. This then suggests the functional form of the above fitting function (Eq. S10). By hand, we then add in the exponential damping factor, to capture wavepacket splitting effects (see below) and other sources of damping in experiment (e.g. heating), as well as the phase ϕ to account for random variation in the position of the cloud after state preparation in the experiment. (Note that for the numerics we have defined $x(t = 0) = 0$, and so we set $\phi = 0$ to reduce the number of fitting parameters.) Figure S4(b) shows an example fit (*red curve*) using Eq. S10 applied to our numerical data (*blue curve*) from Fig. S4(a). The error bars on the fit parameters are from the least-squares fit. The fitted amplitude A and frequency f are plotted in the main text for varying detuning and shaking power.

III. MAPPING FROM THE SYNTHETIC DIMENSION TO REAL SPACE

Analytical results for our synthetic dimension scheme are expressed in terms of the synthetic dimension λ, but the experiment naturally probes real space x. We therefore now derive a formula linking these, which is given as Eq. 6 in the Main Text, and which is used to justify the fitting function as discussed above, and to process the analytical results in Section V. Our aim is to link the COM of a state $|\psi\rangle$ with respect to the synthetic dimension, $\lambda_{\rm com}$, to the COM and width of the state in real space, $x_{\rm com}$ and σ_x respectively. To start, we will expand our state in the harmonic-trap basis as:

$$|\psi\rangle = \sum_\lambda c_\lambda |\lambda\rangle, \tag{S12}$$

where c_λ are complex coefficients with $\sum_\lambda |c_\lambda|^2 = 1$. In terms of the COM variables, it is straightforward to show that

$$\lambda_{\rm com} = |\alpha|^2, \ \alpha \equiv \frac{x_{\rm com} + i p_{\rm com}}{\sqrt{2}}, \tag{S13}$$

where:

$$x_{\rm com} = \langle\psi|\hat{x}|\psi\rangle, \tag{S14}$$
$$p_{\rm com} = \langle\psi|\hat{p}|\psi\rangle, \tag{S15}$$

are the COM in real and momentum space respectively. Here, $x_{\rm com}$ is measured in units of $\sqrt{\hbar/m\omega_x}$, and $p_{\rm com}$ in units of $\sqrt{\hbar m\omega_x}$. We can also write

$$\sigma_x^2 = \langle\psi|\hat{x}^2|\psi\rangle - x^2_{\rm com}, \tag{S16}$$

which follows from the usual expression for the variance of a random variable. Now writing $\hat{x} = \frac{1}{\sqrt{2}}(\hat{a}+\hat{a}^\dagger)$, where $\hat{a}^\dagger$ and $\hat{a}$ are the usual harmonic oscillator raising and lowering operators, and substituting into Eq. S16, yields:

$$\sigma_x^2 = \langle\psi| \left(\hat{a}^\dagger\hat{a} + \frac{1}{2}\right) |\psi\rangle + \frac{1}{2}(\langle\psi|\,\hat{a}^2\,|\psi\rangle + \langle\psi|\,\hat{a}^{\dagger 2}\,|\psi\rangle) - x_{\text{com}}^2, \tag{S17}$$

where we have used the commutator $[\hat{a}, \hat{a}^\dagger] = 1$. Now inserting our expansion of $|\psi\rangle$ (Eq. S12) produces:

$$\sigma_x^2 = \lambda_{\text{com}} + \frac{1}{2} + \frac{1}{2}(S + S^*) - x_{\text{com}}^2, \tag{S18}$$

where we identified $\lambda_{\text{com}} = \sum_\lambda |c_\lambda|^2 \lambda$ and where:

$$S = \sum_{\lambda=0}^{\infty} c_\lambda^* c_{\lambda+2} \sqrt{(\lambda+1)(\lambda+2)}. \tag{S19}$$

Finally, re-arranging for λ_{com} gives:

$$\lambda_{\text{com}} = x_{\text{com}}^2 + \sigma_x^2 - \frac{1}{2} - \frac{1}{2}(S + S^*). \tag{S20}$$

To gain some intuition for the S terms, consider the limit of preparing the system in a particular eigenstate of the harmonic trap $|\lambda_0\rangle$, so $c_\lambda = \delta_{\lambda,\lambda_0}$. This makes $S = 0$, and we have:

$$\lambda_{\text{com}} = x_{\text{com}}^2 + \sigma_x^2 - \frac{1}{2}. \tag{S21}$$

If, instead, the state is a semiclassical Gaussian wavepacket with $c_\lambda \sim \exp(-(\lambda-\lambda_0)^2/2\sigma_\lambda^2)$, we expect Eq. S21 to hold approximately when σ_λ is sufficiently small. Figure S5 shows an example of this result (*red curve*) compared against the COM calculated directly from a numerical simulation (*blue curve*), with agreement up to a small offset. The numerical curve displays small micromotion oscillations as expected, as does the curve calculated from our formula. The formula shows these oscillations because using only a single pair of phases during micromotion averaging does not perfectly remove the micromotion, as discussed in Section II. Note also that the example data and parameters used in this section are the same as the previous one, although the level of agreement is similar in all cases studied. This result demonstrates that the derived conversion formula still holds in the case of the thermal cloud. We can repeat the above calculation but working in terms of momentum rather than position to find:

$$\lambda_{\text{com}} = p_{\text{com}}^2 + \sigma_p^2 - \frac{1}{2}, \tag{S22}$$

where σ_p is the width of the state in momentum space, and the momenta are measured in units of $\sqrt{\hbar m \omega_x}$. An example of this formula applied to the oscillation in Fig. S5 is shown in Fig. S6, showing similar agreement to the real space result.

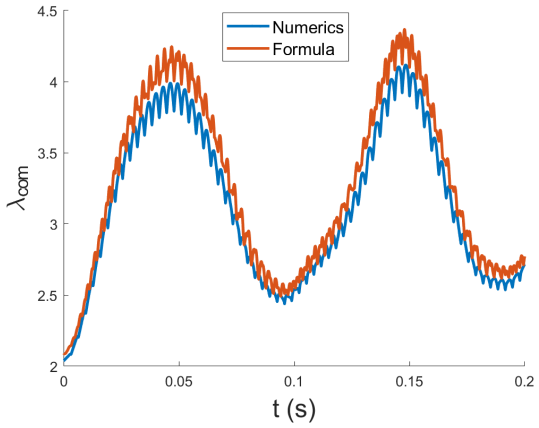

FIG. S6. The momentum space conversion formula (Eq. S22) applied to the same oscillation as Fig. S5. The result of applying Eq. S22 to the RMS phase-averaged momentum COM and width (*blue*) is compared to the synthetic space COM calculated numerically (*red*) and we see agreement up to a small offset.

IV. EFFECTIVE TIME-INDEPENDENT HAMILTONIAN DESCRIPTION

In this section, we show how we arrive at the effective time-independent Hamiltonian shown in the main text:

$$\hat{\mathcal{H}} = \hbar\Delta \sum_\lambda \lambda\,|\lambda\rangle\langle\lambda| + J\sum_\lambda \left[ie^{i\varphi}\,|\lambda+1\rangle\langle\lambda| + \text{h.c}\right] \tag{S23}$$

starting from the full time-dependent Hamiltonian (Eq. 2 in the main text). Note that this effective Hamiltonian is different to that of [S4] in the sense that we can assume that our nearest-neighbour hoppings are constant in λ, whereas those of [S4] scale as $\sqrt{\lambda}$; this is due to the choice of driving potential. As the Hamiltonian is periodic in time, we can use Floquet theory to define the Floquet Hamiltonian, $\hat{H}_F$, according to:

$$\hat{H}_F = \frac{i\hbar}{T_D}\log(\hat{U}(T_D;0)) \tag{S24}$$

where $\hat{U}(T_D;0)$ is the time-evolution operator over a full period of the driving, $T_D = 2\pi/\omega_D$, where ω_D is the driving frequency [S5]. This Hamiltonian can be calculated numerically by splitting the time-evolution operator (Eq. S24) into sufficiently many small timesteps dt. For simplicity, we have neglected terms in the Hamiltonian that depend on the y - direction to work with a 1D Hamiltonian in the λ - basis.

We first investigate the matrix elements of Eq. S24 for the low-V_0 case ($V_0 = 4.16$ nK), as considered in Fig. 1, 2, 3 and 4 in the main text. The Floquet Hamiltonian matrix elements are plotted in Fig. S7 for several detunings and for parameters listed in the caption. More precisely, we plot the real (top row) and imaginary (middle row) parts of the first five diagonals of $\hat{H}_F$, as well as

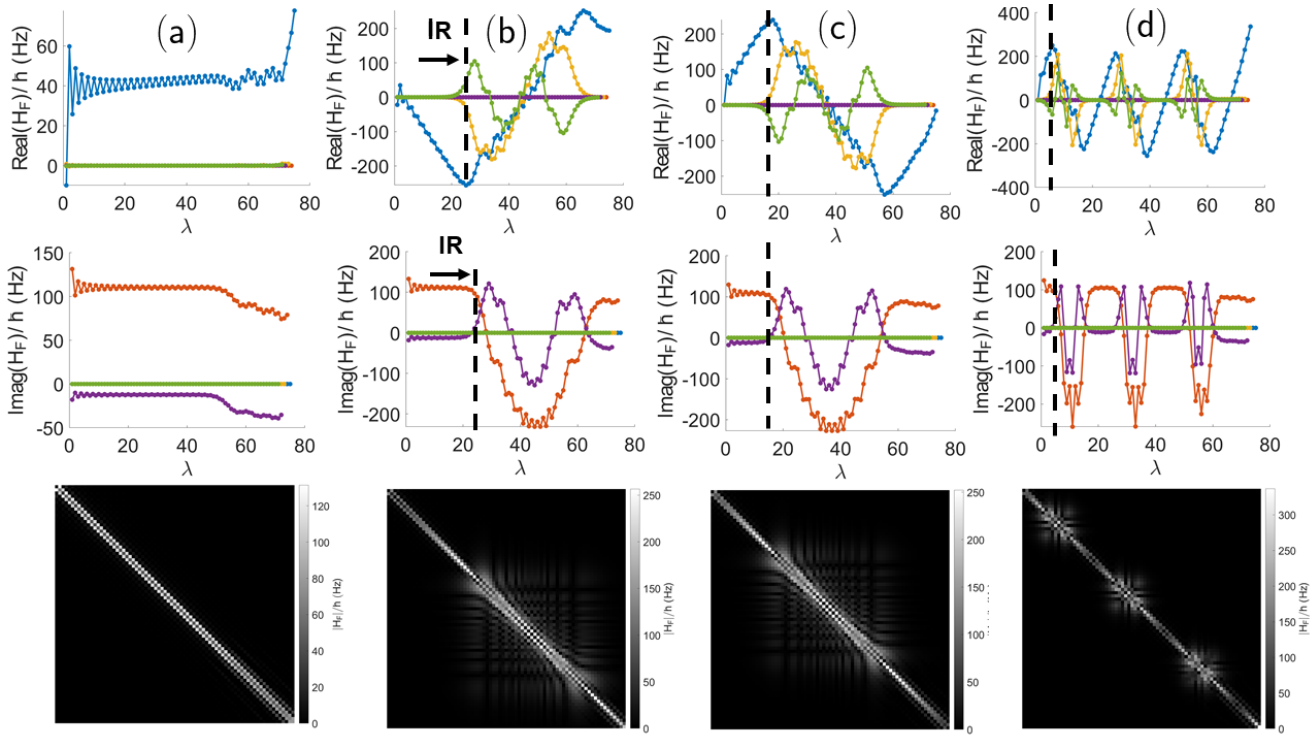

FIG. S7. Numerically-calculated matrix elements of the Floquet Hamiltonian (Eq. S24) for $\omega_x = 2\pi \times 166.5$ Hz, $V_0 = 4.16$ nK and $\varphi = 0$, for $\Delta = 2\pi \times 0, -2, 2$ and 7 Hz in columns (a), (b), (c) and (d) respectively. These parameters correspond to the low-power data shown in Fig. 1, 2, 3 and 4 in the main text. The top row shows the real part of the first five diagonals, the middle row shows the imaginary part, and the final row shows a heat map of $|\hat{H}_F|$. The on-site terms are in blue, the NN hoppings in red and longer-range hoppings in other colours. We see that we can approximate $\hat{H}_F$ by a nearest-neighbour tight-binding model where Δ plays the role of a force along the synthetic dimension. The onset of instability regions (IR), marked by the black dotted lines, show long-range hoppings for some λ and are a numerical artifact and are not physical.

$|\hat{H}_F|$ as a heat map to show the longer-range structure of the Hamiltonian (bottom row). For all figures in this section, the on-site terms are in blue, the nearest-neighbour (NN) hoppings are in red, and longer-range hoppings in other colours. For this low-power figure, we have applied a constant offset to the time-dependent Hamiltonian to ensure that the on-site matrix elements are zero for $\lambda = 0$. This shifts the location of the instability regions (see below) and allows the behaviour for $\Delta < 0$ to be seen more clearly.

As can be seen, for many values of λ, the Hamiltonian can be approximated by the form used in the main text. Firstly, the detuning induces a tilt on the on-site matrix elements (*blue curve*) $\sim \Delta\lambda$, which allows us to interpret this detuning as a constant force along the synthetic dimension (see e.g. Fig. S7 columns (b), (c) between $\lambda \approx 0$ and $\lambda \approx 20$). Note that we verified that the slope of the on-site terms is equal to the detuning by fitting a straight line to these plots. Secondly, across the same regions, we also find nearly-flat NN hoppings (*red curve*), such that the NN hopping energy J can be calculated by taking the average of the NN matrix elements up to the onset of the instability region (see below). This hopping energy does not vary significantly as a function of detuning, and we find the value $J/\hbar = 106 \pm 8$Hz for $V_0 = 4.16$nK. To calculate this error bar on J, we add the standard deviations of the NN hoppings for each of the N_Δ detunings in quadrature to obtain σ, and then use the error bar $\sigma/\sqrt{N_\Delta}$. Thirdly, we also see that we have a small long-range hopping (*purple curve*) which we neglect. Note that all the matrix elements show small oscillations with respect to λ, which may act as a potential minimum around $\lambda = 0$ and be the cause of the cloud splitting effects discussed in the main text and below. This is discussed further in Section VI. Finally, we see the "odd" diagonals of the Hamiltonian (nearest-neighbour, NNNN, etc.) are purely imaginary and the others are purely real, which is caused by the initial driving phase φ playing the role of a Peierls phase in the effective model.

For non-zero detuning in Fig. S7, there also appear to be regions of λ where we no longer have linear on-site terms and flat NN hoppings, but instead have significant long-range hoppings (e.g. between $\lambda \approx 20$ and $\lambda \approx 60$ in column (b)). However, these are an artifact of our numerics and should not be physical. These regions arise because the Floquet Hamiltonian is not unique, but depends on the branch of the matrix logarithm (Eq. S24). In the numerics, the principal branch is always taken,

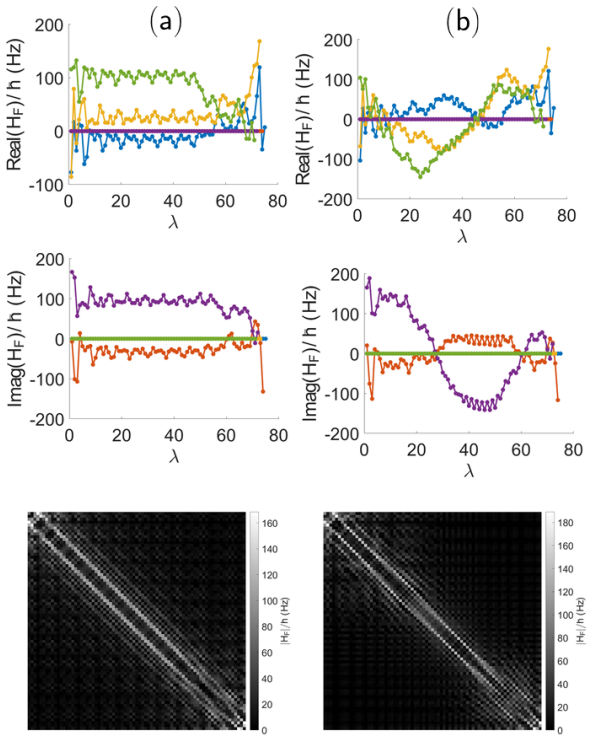

FIG. S8. Floquet Hamiltonian matrix elements for a higher shaking power than Fig. S7. We have $\omega_x = 2\pi \times 142.1$ Hz, $V_0 = 11.96$ nK and $\varphi = 0$, and $\Delta = 2\pi \times 0$ and -2 Hz in columns (a) and (b) respectively. These parameters correspond to the high-power data shown in Fig. 3(a) in the main text. Unlike the low-power case, we find significant long-range hoppings for all λ, and that a detuning does not simply induce a slope on the on-site terms. This is not a numerical artifact, but a result of the failure of the rotating-wave approximation, and precludes building a simple effective Hamiltonian. We use the same layout and colour schemes as Fig. S7.

meaning that the Floquet Hamiltonian is constructed to have eigenvalues that only lie between $-\pi/T_D$ and π/T_D. This leads to the apparent "wrapping around" of onsite terms and an associated variation in off-diagonal terms when the on-site shift due to the detuning becomes large. This can be seen by noting that for larger detuning (column (d)), the apparent breakdown happens earlier and more frequently, and between these regions, the matrix elements look regular and well-behaved. We have also checked our interpretation numerically by adding a constant offset to the time-dependent Hamiltonian $\hat{H}(t)$ that changes the size and location of the apparent breakdown regions while leaving the on-site slope and NN hoppings otherwise unchanged. Finally, we also do not observe any qualitative change in behaviour of our numerical simulations (Section I) when the cloud moves in the instability regions, further confirming that these are not a physical effect.

It is important to distinguish between the above numerical artifact and a genuine breakdown of the effective Hamiltonian employed in the low-V_0 case, caused by the failure of the rotating-wave approximation. This is apparent e.g. in Fig. S7 (a) above $\lambda \approx 55$, where we observe that the matrix elements begin to deviate from their previous values.

For larger values of V_0 (such as considered in Fig. 2 in the main text), we also observe numerically that the matrix elements become less uniform and more long-ranged. This is shown in Figure S8, where we plot the Floquet Hamiltonian matrix elements for $V_0 = 11.96$ nK for two detunings, with parameters as listed in the figure caption. As can be seen, in this case, we find significant long-range hoppings for all λ, and a non-zero detuning does not simply add a slope to the on-site terms. This therefore precludes building a simple analytical model for this behaviour, although we still find that our numerical simulations agree well with experimental results, as in Fig. 3 in the main text.

V. DETAILS OF ANALYTICAL RESULTS

Here we describe in detail how the analytical results for Bloch oscillations in both real and synthetic space are obtained, including corrections to make them comparable to numerical and experimental data, as plotted and discussed in the main text.

As stated in the main text, we expect the cloud COM to oscillate with respect to the synthetic dimension as:

$$\lambda_{\mathrm{com}}(t) = \lambda^0_{\mathrm{com}} + \frac{2J}{\hbar\Delta}(1 - \cos(\Delta t)). \tag{S25}$$

We therefore expect an oscillation frequency of $\Delta/2\pi$ and a maximum λ of $\lambda_{\max} = \lambda^0_{\mathrm{com}} + 4J/\hbar\Delta$. We can then use our result connecting the real and synthetic dimension, Eq. S21, to calculate the maximum displacement of the cloud from $x = 0$. This gives:

$$x_{\max} = \sqrt{\lambda_{\max} - \sigma_x^2 + \frac{1}{2}}, \tag{S26}$$

as discussed in the main text, and where we measure $x_{\max}$ and σ_x in units of $\sqrt{\hbar/m\omega_x}$. We can analytically calculate the width for a thermal cloud $\sigma_x = \sqrt{k_B T/m\omega_x^2}$ [S3], and approximate the cloud width as constant in time, as justified in Section II.

We now take into account cloud splitting, as described in the main text. Note that we discuss methods to reduce this effect in Section VI. The COM with respect to the synthetic dimension is calculated as:

$$\lambda_{\mathrm{com}}(t) = \sum_{\lambda} \lambda \rho(\lambda, t), \tag{S27}$$

where $\rho(\lambda, t)$ is the synthetic space density, calculated numerically as in Section I, where we have integrated out the y-dependence. The presence of a split wavepacket

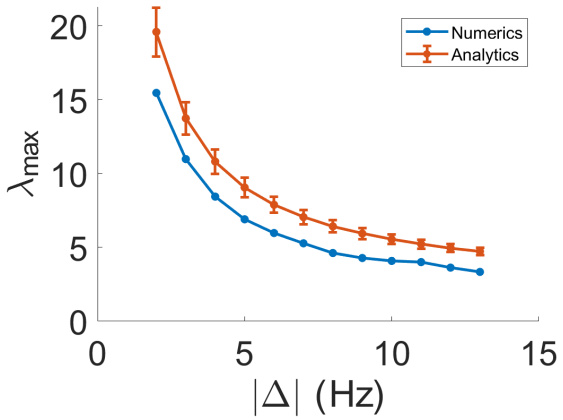

FIG. S9. Cloud-splitting corrected analytical synthetic space amplitude (*red*) compared to the maximum $\lambda_{\rm com}$ obtained numerically (*blue*). We see good agreement, up to a constant offset of around two synthetic lattice sites. Error bars on analytical results are calculated by propagating errors on numerical parameters. Lines are a guide to the eye. Here, we use parameters for the low-power data, as in, for example, Fig. S4.

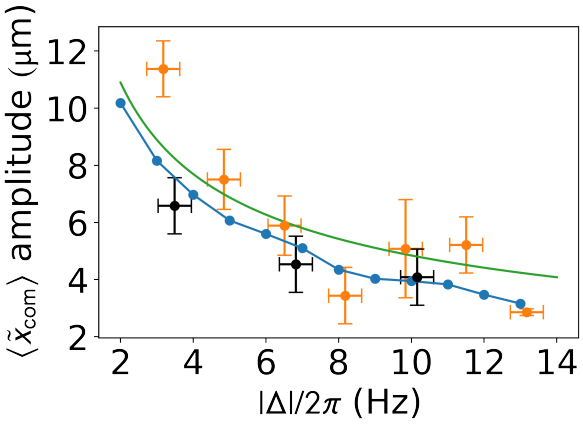

FIG. S10. Bloch oscillation amplitude for variable detuning as in Fig. 2(b) in the main text. The experimental amplitude fit parameter (*orange*) is compared to the fit parameter for the numerics (*blue*) and the analytical result (*green*), where the TOF correction in the analytics is analytically estimated (Eq. S33). We see that this TOF correction also produces good agreement between the anayltics, experiment and numerics, although it overestimates the size of TOF effects. Three experimental datapoints (*black*) are have their driving frequency above the trap frequency, whereas all others are below. Here we have: $\omega_x = 2\pi \times 166.5$ Hz, $V_0 = 4.16$ nK, $T = 20$ nK, $\omega_y = 2\pi \times 10$ Hz and $\varphi = 0, \pi/2$.

component skews this average downward, and the analytical result (Eq. S25) therefore overestimates numerical and experimental amplitudes.

To correct for this, we define a cutoff in λ, λ_c, that cleanly separates the two wavepacket components near the peak of the oscillation. In particular, we choose $\lambda_c = 2J/\hbar\Delta$, because this is about half of the maximum λ coordinate at the oscillation peak (Eq. S25). Near the oscillation peak, we can then write:

$$\lambda_{\rm com} = (1-r)\lambda^{<}_{\rm com} + r\lambda^{>}_{\rm com}, \tag{S28}$$

$$r = \sum_{\lambda>\lambda_c} \rho(\lambda), \tag{S29}$$

where $\lambda^{<}_{\rm com}$ ($\lambda^{>}_{\rm com}$) is the centre of mass of the lower (upper) wavepacket respectively, and r is the amount of wavepacket above the cutoff. We can calculate r numerically and find that it is approximately constant with respect to the detuning, with an average value of $r = 0.52 \pm 0.03$, where the error bar is the standard deviation of the r values over the detunings. This value is for the low-power data, with $V_0 = 4.16$ nK, $\omega_x = 166.5 \times 2\pi$ Hz, $\omega_y = 10 \times 2\pi$ Hz and $T = 20$ nK. To make our analytical result for $\lambda_{\rm max}$ comparable to the numerics and experiment, we hence correct it as:

$$\lambda_{\rm max} = \lambda^0_{\rm com} + r\frac{4J}{\hbar\Delta}. \tag{S30}$$

This result is plotted in Fig. S9 (*red*) and compared against the maximum $\lambda_{\rm com}$ in the numerics (*blue*). We see good agreement, up to a roughly constant offset of around two synthetic lattice sites. We can also use this corrected expression for $\lambda_{\rm max}$ in our real space result (Eq. S26) to get:

$$x_{\rm max} = \sqrt{\lambda^0_{\rm com} + r\frac{4J}{\hbar\Delta} - \sigma_x^2 + \frac{1}{2}}. \tag{S31}$$

We now need to apply three further corrections to this real space result in order to compare to the experimental and numerical results including TOF.

Firstly, we need to estimate the effect of TOF expansion. To do this, we numerically calculate the ratio of the maximum of the real space oscillation including TOF (Section II) to the maximum of the oscillation without. We find that this is approximately independent of detuning, and has a value of $\alpha_{\rm tof} = 5.25 \pm 0.08$, where the error bar is the standard deviation of the $\alpha_{\rm tof}$ values over the detunings. As for r above, this is calculated for the low-power data. We then correct our real space result as:

$$x_{\rm max} \to \alpha_{\rm tof} x_{\rm max}. \tag{S32}$$

Alternatively, we can consider correcting our result analytically by calculating the COM velocity $v_{\rm com}$ at the oscillation peak. To do this, we can use the momentum space version of the λ formula (Eq. S22) to calculate $p_{\rm com}$ at the oscillation peak, including the wavepacket splitting correction, and then calculating $v_{\rm com} = p_{\rm com}/m$, to yield:

$$v_{\rm com} = \sqrt{\frac{\hbar}{m\omega_x}}\frac{1}{m}\sqrt{\lambda^0_{\rm com} + r\frac{4J}{\hbar\Delta} + \frac{1}{2} - \sigma_p^2}, \tag{S33}$$

where σ_p is calculated from the numerics and assumed constant in time, and we measure σ_p in units of $\sqrt{\hbar m\omega_x}$. We can then apply this time-of-flight correction to $x_{\max}$:

$$x_{\max} \to x_{\max} + v_{\rm com} t_{\rm tof}. \tag{S34}$$

The effect of doing this, together with the two corrections described below, is shown in Fig. S10 (*green curve*), where the blue curve is the amplitude fit parameter for the numerical simulations, and the orange points are the fit parameter for the experimental data, as discussed in Section II and the main text, and where we use the same low-power parameters as Fig. 1, 2, 3 and 4 in the main text. We see that the level of agreement between these analytics and the numerics and experiment is comparable to the method using a numerical TOF correction, although this method clearly overestimates the effect of TOF.

Next, we correct for the effect of RMS averaging. As described in Section II, the RMS average over initial driving phases to remove micromotion slightly underestimates the true size of the oscillation (Fig. S4(a)). If we model the dynamics of the COM as a beat:

$$x_{\rm com}(t) = A\sin(\omega_D t)\sin\left(\frac{\omega_B t}{2}\right), \tag{S35}$$

where ω_B is the slow Bloch oscillation frequency, we can then RMS-average out the micromotion using two initial driving phases of 0 and $\pi/2$:

$$\langle x_{\rm com}\rangle^2 = \frac{1}{2}((A\sin(\omega_D t)\sin(\omega_B t/2))^2 + (A\sin(\omega_D t+\pi/2)\sin(\omega_B t/2))^2). \tag{S36}$$

Here, we have shifted the micromotion part of the beat by $\pi/2$. Simplifying gives $\langle x_{\rm com}\rangle^2 = A^2\sin(\omega_B t/2)^2/2$. We can then calculate a scale factor between the averaged and un-averaged results, $\alpha_{\rm rms} \equiv \langle x_{\rm com}\rangle_{\max}/A = 1/\sqrt{2}$. We then apply the correction:

$$x_{\rm com} \to \alpha_{\rm rms} x_{\rm com}. \tag{S37}$$

Note that we can calculate a scale factor based on an infinite number of driving phases by doing the RMS time-average, and we find the same result. As discussed in Section II, our numerical results can be well-described by such a sinusoidal beat, so this approach works well for our data.

Our final correction is due to the fitting function used (Eq. S10). Neglecting damping, our fitting function will have a maximum value of $x_{\max} = \sqrt{2}A$, and we analytically calculate $x_{\max}$. We therefore correct our analytical result so far as:

$$x_{\max} \to \frac{1}{\sqrt{2}} x_{\max}, \tag{S38}$$

so that we can compare directly to the fit parameters obtained from the numerics and experiment. Our final analytical result for $x_{\max}$, as shown in the main text, is then:

$$x_{\max} = \frac{1}{\sqrt{2}}\alpha_{\rm rms}\alpha_{\rm tof}\left(\sqrt{\frac{\hbar}{m\omega_x}\left(\lambda^0_{\rm com} + r\frac{4J}{\hbar\Delta} + \frac{1}{2}\right) - \sigma_x^2}\right), \tag{S39}$$

where we have restored SI units. Finally, note that these same analytical results are used for the variable-power data in Fig. 3(b) in the main text, where the numerical parameters $\alpha_{\rm tof}$, J and r were re-calculated for this dataset.

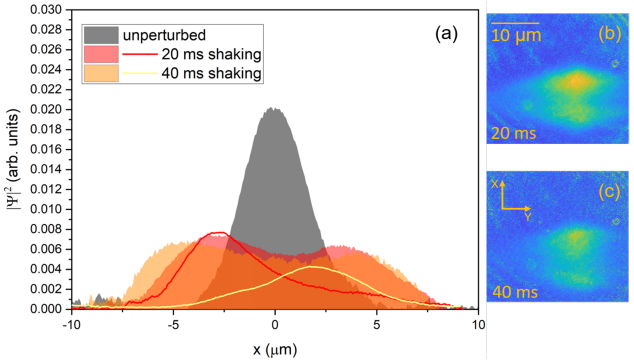

FIG. S11. (a) Column density distribution integrated along the y direction of our atomic samples after 5 ms of time of flight. The shaded areas correspond to the average of 30 experimental runs where we vary the shaking phase. The solid lines are examples of density distributions that are obtained with fixed phase. The number of atoms is $\simeq 15\times10^4$. (b) and (c) are the column densities averaged over 30 runs with different phases in the shaking potential that we observe after 5 ms of time of flight and with 20 and 40 ms of shaking time respectively.

VI. CREATION OF HIGHLY-EXCITED STATES

Bloch oscillations along the synthetic dimension offer a way to controllably populate highly-excited atomic trap states. Indeed, by stopping the shaking at a certain given time it is possible to 'freeze' the dynamics. If this is done when the Bloch oscillation is exploring high λ states, the resulting state will have a considerable admixture of highly-excited harmonic trap states. In Fig. S11 we show an example of states obtained after a 5ms TOF expansion with such a technique with $\Delta/2\pi \simeq 17$ Hz, $V_0 \simeq 1.2$ nK and stopping the Bloch evolution when the oscillation has reached the peak (40 ms) and half way (20 ms). By averaging over several different phases of the shaking potential, we can reconstruct the whole set of states that can be obtained for a given Bloch evolution time, this is shown as shaded areas in Fig. S11 (a) and the column density profiles in Fig. S11 (b) and (c). We observe that the resulting density profiles acquire the characteristic double-lobe structure typical of highly-excited harmonic trap states. Additionally, as the Bloch dynamics evolve,

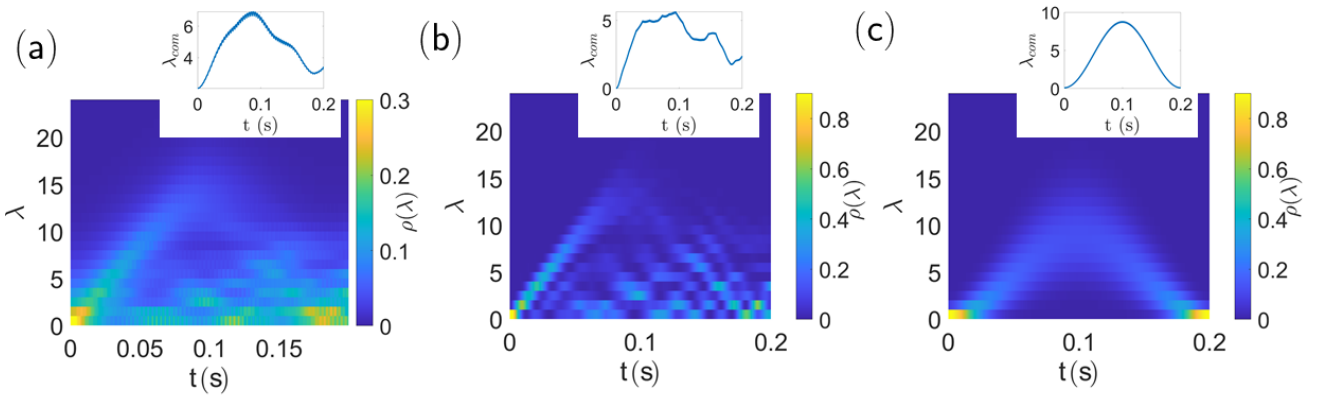

FIG. S12. (a): Time evolution of the integrated synthetic space density for a thermal cloud under our usual driving potential using typical parameters, for a detuning of $\Delta = 5 \times 2\pi$ Hz. We see significant cloud splitting and a relatively wide oscillating component. We use identical parameters to our low-power data elsewhere in this work, with $\varphi = 0$. (b): The result in (a) but with increased trapping frequency and decreased temperature, showing that the oscillating part of the cloud becomes much narrower in synthetic space. Note the different colour scale to (a). We use the same parameters as (a) but with $T = 5$ nK and $\omega_x = 2\pi \times 500$ Hz. (c): Time evolution of the integrated synthetic space density of a thermal cloud for a modified driving potential, showing that the entire cloud moves, with no split component. Note that the linear driving potential together with parameters as in (a) produces a wide oscillating cloud, so we also increase the trapping frequency and decrease the temperature here to compensate for this. We use: $\kappa x_{\rm qho} = 1$ nK, with $x_{\rm qho} = \sqrt{\hbar/m\omega_x}$, $\omega_x = 500 \times 2\pi$ Hz, $\Delta = 5 \times 2\pi$ Hz, $T = 10$ nK and $\omega_y = 10 \times 2\pi$ Hz. The insets of each panel shows the corresponding λ COM as a function of time. Note that the results for (a) and (b) are not rescaled to take into account cloud splitting.

we observe that the distance between the two lobes increases, as expected when populating increasingly higher states. Notably, by controlling the phase of the shaking potential, it is possible to accurately control the shape and position of the final state. This is shown in Fig. S11 (a), where the two solid lines correspond to averages over several runs with the same phase both for the 20 and 40 ms cases.

We have additionally measured the lifetime of the states created by measuring the number of atoms as a function of time after the Bloch evolution is stopped. We then performed an exponential decay fit, whose decay time sets the lifetime of the state. Concerning the states shown in Fig. S11 in particular, we have measured that the lifetime for the states produced after 20 ms of shaking potential is $\simeq$1 s, while for those produced after 40 ms is $\simeq$600 ms. Therefore the lifetime of these highly-excited states is sufficiently long to allow one to practically use them. As an example, they would provide a good overlap with a double-well potential enabling new possibilities for trapped atom interferometry [S6].

The fidelity of the excited states could be further improved by decreasing the proportion of the cloud that remains in the low-lying λ states, and by decreasing the width with respect to λ of the portion that does oscillate. One approach to achieving this is by a combination of using a stronger trap (i.e. increasing ω_x) and/or a lower temperature, both of which reduce the width of the initial Maxwell-Boltzmann distribution. Fig. S12(a) and (b) show the synthetic space density profile, with y-dependence integrated out, for a numerical simulation of a thermal cloud with (a) the typical parameters used elsewhere in our work, and (b) a larger trapping frequency and lower temperature, over a single Bloch oscillation period. As can be seen, in panel (b) the part of the cloud that oscillates is narrower with respect to λ than with our more typical parameters in panel (a). Note that, for a small enough temperature, a significant initial condensate fraction may also affect the dynamics. However, we have verified numerically that an initial state with the whole cloud in the $\lambda = 0$ state (i.e. a non-interacting BEC) still undergoes Bloch oscillations under the driving potential.

We also note that the width of the oscillating part of the cloud also depends upon the detuning. In Fig. S13, for the low-power parameters used in the Main Text and a detuning of $\Delta/2\pi = 2$Hz (panel (a)) and $\Delta/2\pi = 5$Hz (panel (b)), the density with respect to λ is shown close to the peak of the oscillation. The oscillating part of the cloud can be seen to have a full-width at half-maximum (FWHM) of around 8 states in (a). This width depends upon the detuning, with larger detunings yielding smaller widths. For example, in panel (b), the FWHM is around 5 states. Note that these methods to reduce the width of the cloud with respect to λ could be extended towards single-site resolution.

Another strategy for improving the fidelity is to optimize the driving potential. As an example, Fig. S12(c) shows the effect of a different driving potential, $V(x,t) = \kappa x \cos(\omega_D t)$, upon a lower-temperature thermal cloud ($T = 10$ nK), as calculated numerically using the technique described in Section I. Note that this driving po-

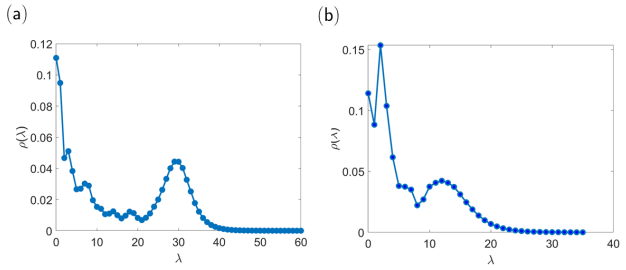

FIG. S13. Cloud density with respect to λ for the low power parameters used in the Main Text and a detuning of $\Delta/2\pi =$ 2Hz (panel (a)) and $\Delta/2\pi = 5$Hz (panel (b)). The density is extracted from close to the peak of the oscillation. We clearly see the oscillating part of the cloud, which has a full-width at half-maximum of around 8 states in (a) and around 5 states in (b).

tential is the same as that of [S4] (see Eq. 2 therein). As can be seen, the entire cloud undergoes the Bloch oscillation, with no split component. This difference is likely because for the experimental driving potential (Eq. 1 in the Main Text), there are oscillations in the Floquet Hamiltonian matrix elements (e.g. Fig. S7) at low λ, which include, for example, an effective potential minimum at $\lambda = 0$ which may trap some atoms, leading to the cloud splitting. For the linear driving potential, on the other hand, the Floquet Hamiltonian does not exhibit such oscillations, although there is then a strong λ-dependence in the hopping elements [S4]. Going further, quantum control approaches could be used to further numerically optimize the driving potential, in order to improve the fidelity of desired state preparation. Finally, another possible strategy for improving the fidelity of excited states would be to employ a two-step protocol. Firstly, the cloud could be placed into an excited trap state without using the driving potential [S7]. Secondly, the driving potential could be activated, causing Bloch oscillations in the synthetic dimension bulk.

[S1] A. Ponomarev, *Dynamics of cold Fermi atoms in one-dimensional optical lattices*, Ph.D. thesis, Albert-Ludwigs-Universität (2008).

[S2] D. Gelman, *Quantum Dynamics of Ultrafast Dissipative Processes*, Ph.D. thesis, Hebrew University of Jerusalem (2006).

[S3] C. Pethick and H. Smith, *Bose-Einstein Condensation in Dilute Gases* (Cambridge University Press, 2001).

[S4] H. Price, T. Ozawa, and N. Goldman, Phys. Rev. A **95**, 023607 (2017).

[S5] N. Goldman and J. Dalibard, Phys. Rev. X **4**, 031027 (2014).

[S6] V. Guarrera, R. Szmuk, J. Reichel, and P. Rosenbusch, New J. Phys. **17**, 083022 (2015).

[S7] T. Müller, S. Fölling, A. Widera, and I. Bloch, Phys. Rev. Lett. **99**, 200405 (2007).

CHAPTER 3

ARTIFICIAL GAUGE FIELDS IN THE T-Z MAPPING FOR OPTICAL PULSES: SPATIO-TEMPORAL WAVEPACKET CONTROL AND QUANTUM HALL PHYSICS

Chapter 3 consists of a manuscript demonstrating a novel way to engineer quantum Hall physics for photons in arrays of coupled optical waveguides, and the implications of this physics for optics. The paper contains some introductory material, but before presenting the work itself we provide a more detailed introduction in addition. In particular, we review the idea of coupled waveguide arrays for quantum simulation, indicating the key physical ideas and discussing the history of the platform. The manuscript itself then follows.

With reference to the author list on the manuscript, I carried out theoretical work under the guidance of H.M.P., I.C., S.M. and M.C.R. The project was conceived and designed by H.M.P., I.C. and M.C.R. C.O. drafted the manuscript, which was then revised by all authors.

3.1 Waveguide Arrays for Quantum Simulation

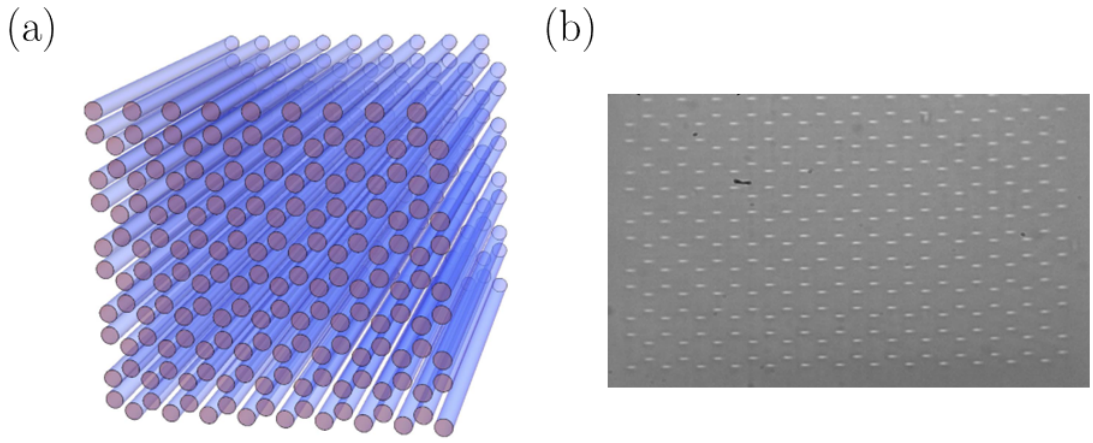

Figure 3.1: (a): Schematic and (b): image of an array of laser-written optical waveguides in a honeycomb lattice arrangement. The light propagates mostly in the z-direction, along the length of the waveguides in (a). Adapted from [13].

1D and 2D arrays of optical waveguides have been used as a platform to realise a variety of physical phenomena for many years. In this section, we review the typical theoretical and experimental approach that is often used, and give an overview of the range of

physical phemonena that have been explored. We then build on this work in the paper. References [13, 90] give an overview of the essential physics of this platform, with the latter having a particular emphasis on the topological physics that can be realised.

Fig. 3.1 shows a typical waveguide array system: a femtosecond laser is translated along the length of some optical medium, forming regions of increased material density and hence an increased refractive index (i.e. a dielectric waveguide). This is done repeatedly to form either a 1D or 2D lattice of some chosen geometry. The waveguides are not independent, but weakly coupled to each other. The mechanism for this coupling is evanescence; the waveguides do not perfectly confine light, but allow some leakage into the background optical medium. If two waveguides are sufficiently close, these evanescent tails overlap, and allow some transfer of light between waveguides. At this point, the intuitive connection to quantum simulation is clear. We can think of each waveguide as an artificial atom, with the discrete modes of each waveguide being analogous to atomic orbitals. The 'atoms' are then assembled into a lattice via the above laser writing procedure. The inter-waveguide evanescent coupling then plays the role of the overlap of atomic orbitals, leading to an analogy with the usual tight-binding picture of solid state physics. Moreover, as we discuss shortly, the paraxial propagation of light along the length of the waveguides is directly analogous to time evolution in quantum mechanics. Overall, we therefore see that the diffraction of light through a lattice of optical waveguides naturally simulates the time evolution of a 1D or 2D quantum lattice model.

More formally, the propagation of monochromatic light of frequency ω in a waveguide with refractive index $n(\mathbf{r})$ is described by the Helmholtz equation [13, 91]:

$$\left(\nabla^2 + \frac{\omega^2}{c_0^2} n(\mathbf{r})^2\right) E(\mathbf{r}) = 0, \tag{3.1}$$

where $E(\mathbf{r})$ is the electric field and c_0 is the speed of light in vacuum. If we now assume that the propagation is paraxial, meaning that it travels mostly along, say, the z-direction,

we can decompose the electric field as:

$$E(\mathbf{r}) = a(\mathbf{r})e^{i\beta z}, \tag{3.2}$$

where we assume that the envelope $a(\mathbf{r})$ depends only weakly on z, and where β is the propagation constant. Substituting this into the Helmholtz equation and neglecting a term $\sim \partial^2 a/\partial z^2$ produces:

$$\frac{\partial^2 a}{\partial x^2} + \frac{\partial^2 a}{\partial y^2} + 2i\beta\frac{\partial a}{\partial z} - \beta^2 a + \frac{\omega^2}{c_0^2}n^2 a = 0. \tag{3.3}$$

We then include the weak refractive index perturbation (i.e. the waveguide) in the problem by writing $n(\mathbf{r}) = n_0 + \Delta n(\mathbf{r})$, where n_0 is the refractive index of the unwritten medium and Δn is the small refractive index perturbation due to the waveguide, and by writing $\beta \approx \omega n_0/c_0$. This leads to:

$$i\frac{\partial a}{\partial z} = -\frac{c_0}{2n_0\omega}\left(\frac{\partial^2 a}{\partial x^2} + \frac{\partial^2 a}{\partial y^2}\right) - \frac{\omega}{c_0}\Delta n(\mathbf{r})a. \tag{3.4}$$

We therefore see that the Helmholtz equation resembles a Schrödinger equation when the monochromatic light propagates paraxially through a waveguide of the type we discussed. We see that the diffraction of the light in the $x-y$ place, perpendicular to the waveguide axis, plays the role of kinetic energy, and that the waveguide can be thought of as a potential well. Note that we adopted a continuum description of a single waveguide here; we could then include the aforementioned evanescent coupling to other waveguides via:

$$i\frac{\partial a_i}{\partial z} = -\beta a_j - C(a_{j-1} + a_{j+1}), \tag{3.5}$$

where C denotes the coupling strength between the waveguide j and its neighbours, with the electric field envelopes in each waveguide being a_i. Therefore, as advertised earlier, the propagation of the light along the z-direction is equivalent to time-evolution in quantum

mechanics.

The simple picture of waveguide arrays outlined above can naturally be extended in a number of ways, allowing for the investigation of a variety of single-particle quantum phenomena [92–99] or interacting physics if the optical medium is nonlinear [100–104]. The interacting regime can be reached by employing Kerr-nonlinear optical media, which lead to a cubic nonlinearity in the effective Schrodinger equation, much like a Gross-Pitaevskii equation for Bose-Einstein condensates.

The recent interest in exploring topological models in these waveguide array systems [13, 105] is based upon breaking the z-reversal symmetry, which corresponds to breaking time-reversal symmetry in the quantum mechanical case. Broken time-reversal symmetry then allows access to a large class of topological models as discussed in the Introduction. In practice, the z-reversal symmetry is broken by using waveguides that are helical, not straight. Note that the pitch of the helix should be large enough that the paraxial approximation is not violated, and an input mode is transported adibatically through the array [106]. It can be shown that this leads to an artificial magnetic vector potential in Eq. 3.4, which can be included at the level of the tight-binding model as a Peierls phase on the hoppings. If the lattice is chosen to be honeycomb for example, the system then maps exactly onto the Haldane model [107]. A major early achievement in this arena was in 2013 [106]. These propagating geometries have since proved themselves to be a powerful tool for studying a wide variety of topological physics, including the investigation of the interplay between nonlinearity and topology [108–110], topological physics in non-2D geometries [111–114], non-Hermitian effects in topology [115, 116], disorder [117], Thouless pumping schemes [118, 119], transport [120] and quantum walks [121].

In the manuscript comprising the rest of this chapter, we further extend the technique of waveguide arrays as a quantum simulator by considering the propagation of an optical pulse, not monochromatic light. We show that the Helmholtz equation in this case now acquires a term proportional to the second time derivative of the electric field, which, in the quantum mechanical analogy, can be thought of as a kinetic energy term along

a synthetic time dimension. We go on to show how this extra degree of freedom can be exploited to engineer quantum Hall physics in a 1D waveguide array, with a view towards fractional quantum Hall states of photons if strong-enough nonlinearities can be introduced [122, 123]. Now that we have provided some motivation and context for this work, we present the paper itself.

Artificial gauge fields in the t-z mapping for optical pulses: spatio-temporal wavepacket control and quantum Hall physics

CHRISTOPHER OLIVER[1,*], SEBABRATA MUKHERJEE[2], MIKAEL C. RECHTSMAN[3], IACOPO CARUSOTTO[4], AND HANNAH M. PRICE[1]

[1] *School of Physics and Astronomy, University of Birmingham, Edgbaston, Birmingham, UK, B15 2TT*
[2] *Department of Physics, Indian Institute of Science, Bangalore 560012, India*
[3] *Department of Physics, The Pennsylvania State University, University Park, Pennsylvania 16802, USA*
[4] *Pitaevskii BEC Center, INO-CNR and Dipartimento di Fisica, Università di Trento I-38123 Trento, Italy*
[*] *chroli.phys@gmail.com*

Abstract: We extend the $t - z$ mapping formalism of time-dependent paraxial optics by identifying configurations displaying a synthetic magnetic vector potential, leading to a non-trivial band topology in propagating geometries. We consider a 1D array of coupled optical waveguides beyond the standard monochromatic approximation, and show that the wave equation describing paraxial propagation of optical pulses can be recast in the form of a Schrödinger equation, including a synthetic magnetic field whose properties can be controlled by varying the waveguide properties across the array. We use an experimentally-motivated model of a laser-written waveguide array to demonstrate that this synthetic magnetic field can be engineered to produce interesting observable effects such as cyclotron motion, a controllable Hall drift of the wavepacket displacement in space or time and unidirectional propagation in chiral edge states. These results significantly extend the variety of physics that can be explored within propagating geometries and pave the way for exploiting this platform for higher-dimensional topological physics and strongly correlated fluids of light.

1. Introduction

A remarkable result of paraxial optics is that the electromagnetic field of paraxially-propagating classical light can be described by a Schrödinger-like equation [1]. In this equation, the usual time evolution of a wavefunction is replaced by the propagation of the electric field envelope along the optical axis, z, of the medium. In practice, a major platform for investigating paraxial propagation is arrays of coupled optical waveguides, laser-written into a substrate [2]. In general, these propagating geometries can be used to emulate a variety of single-particle quantum phenomena [3–10] or mean-field interacting physics if the medium is nonlinear [11–15]. This interacting physics includes Bose-Einstein condensates of photons, and opens the way to studies of fluids of light [16–18], with interesting perspectives towards quantum features [19].

One exciting avenue that has been explored intensively over the last 15 years is that of topological photonics [20, 21]. In this field, the physics of topological phases of matter, originally discovered within the context of electrons in solids, is applied to photonics. Propagating geometries have proven to be a very fruitful platform in this context, with a major early achievement [22] being the investigation of Floquet topological insulators, in which a honeycomb array of waveguides acquires a non-trivial topology when a helical patterning of the waveguides is introduced. Since the propagation distance z plays the role of the temporal evolution, the breaking of the translational symmetry along the z-direction of the helical waveguide system is analogous to the breaking of time-reversal symmetry in a 2D tight-binding model of electrons under a temporally periodic modulation [23]. More generally, similar propagating geometries have proven to be a powerful

tool for studying a wide variety of topological physics, including the investigation of the interplay between nonlinearity and topology [24–26], topological physics in non-2D geometries [27–30], non-Hermitian effects in topology [31,32], disorder [33,34], Thouless pumping schemes [35,36], transport [37] and quantum walks [38].

So far, most if not all works on topological photonic effects using propagating geometries have employed monochromatic light, and so do not make significant use of the temporal dynamics associated with an optical pulse. From paraxial optics [1], it is well known that the Schrödinger-like equation describing the propagation of an optical pulse in a dispersive medium also includes a second-order time derivative term, with the same structure as a kinetic energy term in quantum mechanics. This allows us to interpret time t as an additional spatial dimension in addition to the transverse x, y ones, while the coordinate z along the propagation direction plays the role of a time. This interchange of the role of space and time is known as the $t - z$ mapping and has also been investigated at the quantum level in [19,39–41].

In this work, we propose a novel configuration based on an array of coupled optical waveguides where a synthetic gauge field naturally appears when the temporal dynamics of an optical pulse is taken into account under the $t - z$ mapping. In particular, we consider propagation across a 1D array of coupled optical waveguides with slightly different properties, and show that the 2D wave equation for the classical optical field propagation in a mixed spatial j/temporal t plane has the form of a Schrödinger equation including a synthetic vector potential term as in the coupled wire model of quantum Hall physics [42–44]. A realistic configuration resulting in a sizable synthetic magnetic field and a non-trivial band topology is put forward, and experimentally accessible signatures of the magnetic effects are pointed out. These include a cyclotron motion of light wavepackets in the spatio-temporal $j - t$ plane, a Hall drift in response to additional synthetic electric fields in either the spatial or the temporal direction, as well as unidirectional propagation in chiral edge states. As compared to previous schemes [20,45] for synthetic magnetic fields and synthetic dimensions in arrays of microcavities [46,47] or waveguides [48–51], our proposal has the crucial advantage that it does not require a dynamical modulation of the system and provides a new tool for the manipulation of the spatio-temporal shape of optical wavepackets. Moreover, the local interactions in our system suggest exciting prospects for strongly-correlated fluids of photons if the interaction strength can be scaled up.

The structure of the Article is the following: Sec. 2 summarizes the mapping of the paraxial wave equation onto the Schrödinger equation with a synthetic magnetic field. The quantum Hall coupled wire model is reviewed in Sec. 3 and an experimentally realistic configuration for realizing it is presented in Sec. 4. Observable signatures of the synthetic magnetic field and the non-trivial band topology are presented in Sec. 5. Conclusions and perspectives towards quantum topological photonics and quantum fluids of light are finally sketched in Sec. 6.

2. Mapping the paraxial wave equation onto a Schrödinger equation with a synthetic magnetic field

In this first Section, we review the derivation of the well-known wave equation for the paraxial propagation of a pulse though an array of coupled waveguides [1]. For suitably designed inhomogeneous arrays, we then map the wave equation onto a Schrödinger equation for a particle in a synthetic magnetic field, where time plays the role of a synthetic spatial dimension and propagation through the array corresponds to time evolution. This equation will be our workhorse for the rest of the paper. Consider an optical pulse propagating through a 1D array of $j = 1, \ldots, N$ single-mode waveguides whose optical axis points in the z-direction, as shown schematically in Fig. 1(a). We can write the electric field in waveguide j as:

$$E_j(\mathbf{r}, t) = e_j(x, y) a_j(z, t) e^{i(\beta_{j_{\mathrm{ref}}}(\omega_0) z - \omega_0 t)}, \tag{1}$$

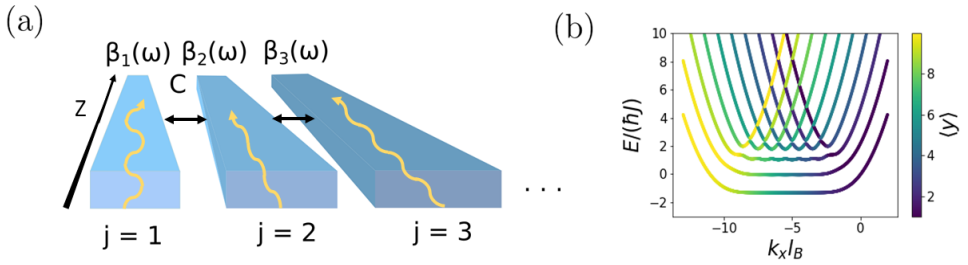

Fig. 1. (a): A schematic of our proposed setup consisting of a 1D array of coupled single-mode waveguides. Each waveguide has a propagation constant $\beta_{j=1,\ldots,N}(\omega)$ and neighbouring waveguides are coupled together evanescently with a coupling strength C. The waveguide axis lies along the z-direction. The waveguide properties (e.g. the width and refractive index) vary across the array to engineer a non-trivial synthetic magnetic field. (b): Example of the band structure of a quantum Hall coupled wire model formed by N wires with periodic boundary conditions in the continuous x-direction. For each state of the band structure, the color coding indicates its average spatial position along y. We measure k_x in units of $1/l_B$, where $l_B = \sqrt{\hbar/qB}$ is the magnetic length. The one free parameter of the Hamiltonian, the ratio of the two energy scales $r \equiv (\hbar^2/ml_B^2)/(\hbar J)$, is set to unity. We find, at low energies, dispersionless bulk Landau levels and chiral states localised on the system edge in the gaps, as is characteristic of a quantum Hall model.

where $e_j(x, y)$ is the electric field profile in the plane perpendicular to the optical axis; ω_0 is the pulse carrier frequency and $\beta_{j_{\text{ref}}}(\omega_0)$ is the carrier propagation constant in the $j = j_{\text{ref}}$ waveguide used as a reference. We choose this decomposition in order to to separate out the the envelope $a_j(z, t)$ which, within the paraxial approximation, is assumed to be slowly varying as a function of z and t. We do not consider non-trivial polarisation effects so E_j can represent any polarisation component of the electric field. We assume that the waveguides are effectively single-mode, meaning that any excited modes are well-separated from the fundamental mode in propagation constant, so that they play no role in the dynamics.

In Fourier space, the propagation of the pulse is described by the coupled equations for the field amplitudes in the different waveguides:

$$i\frac{\partial \tilde{a}_j}{\partial z} = -\left(\beta_j(\omega' + \omega_0) - \beta_{j_{\text{ref}}}(\omega_0)\right)\tilde{a}_j - C\left(\tilde{a}_{j-1} + \tilde{a}_{j+1}\right), \tag{2}$$

where $\tilde{a}_j(z, \omega')$ is the Fourier transform of $a_j(z, t)$ with respect to t in terms of the frequency variable $\omega' = \omega - \omega_0$ and C is the evanescent coupling between neighbouring waveguides. For simplicity, this is assumed to be frequency-independent in the range of interest.

We now Taylor-expand $\beta_j(\omega)$ about ω_0:

$$\beta_j(\omega) \approx \beta_j(\omega_0) + \left.\frac{d\beta_j(\omega)}{d\omega}\right|_{\omega_0}(\omega - \omega_0) + \frac{1}{2}\left.\frac{d^2\beta_j(\omega)}{d\omega^2}\right|_{\omega_0}(\omega - \omega_0)^2, \tag{3}$$

where we neglect terms $O((\omega - \omega_0)^3)$ and higher. We then identify:

$$v_g^{(j)} = \left[\left.\frac{d\beta_j}{d\omega}\right|_{\omega_0}\right]^{-1}, \qquad D_j = \left.\frac{d^2\beta_j}{d\omega^2}\right|_{\omega_0}, \tag{4}$$

as the group velocity and the group velocity dispersion in waveguide j, respectively. Substituting this expansion into Eq. 2 and Fourier-transforming back to the time domain produces the wave

equation:

$$i\frac{\partial a_j}{\partial z} = \frac{D_j}{2}\frac{\partial^2 a_j}{\partial t^2} - \frac{i}{v_g^{(j)}}\frac{\partial a_j}{\partial t} - \left(\beta_j(\omega_0) - \beta_{j_{\text{ref}}}(\omega_0)\right) a_j - C(a_{j+1} + a_{j-1}). \tag{5}$$

which can be easily mapped onto a Schrödinger equation.

To this purpose, we transform to a frame co-moving with the group velocity $v_g^{(\text{ref})} \equiv d\beta_{j_{\text{ref}}}/d\omega\big|_{\omega_0}$ in the j_{ref} reference waveguide using a Galilean transformation with space and time interchanged, $\zeta \equiv z$ and $\tau \equiv t - z/v_g^{(\text{ref})}$. After completing the square to eliminate the first time-derivative, Eq. 5 becomes:

$$i\frac{\partial a'_j}{\partial \zeta} = \frac{1}{2m_j}\left(-i\frac{\partial}{\partial \tau} - A_j^{(\tau)}\right)^2 a'_j + V_j\, a'_j - C\left(a'_{j+1} + a'_{j-1}\right), \tag{6}$$

where we have defined

$$m_j = -\frac{1}{D_j}, \qquad A_j^{(\tau)} = \frac{1}{D_j}\left(\frac{1}{v_g^{(j)}} - \frac{1}{v_g^{(\text{ref})}}\right), \qquad V_j = \frac{1}{2D_j}\left(\frac{1}{v_g^{(j)}} - \frac{1}{v_g^{(\text{ref})}}\right)^2 - \left(\beta_j(\omega_0) - \beta_{j_{\text{ref}}}(\omega_0)\right) \tag{7}$$

and where $a'_j(\zeta, \tau)$ is the electric field envelope in the co-moving frame (denoted from now on by the prime symbol).

This set of equations has the form of coupled Schrödinger equations, where propagation along the optical axis of the waveguide array plays the role of time evolution, as we expect from the $t - z$ mapping. The particle with unit charge moves in a 2D system with one discrete (j) dimension and one continuous (τ) dimension: in the former direction, the hopping amplitude is C; in the latter, the particle has a position-dependent mass m_j. On top of this, the particle experiences a magnetic vector potential in the τ-direction $A_j^{(\tau)}$ and a scalar potential V_j. Crucially, the magnetic vector potential is oriented along τ and is waveguide-dependent, so non-trivial magnetic field effects can be engineered by modulating the characteristics of the waveguides across the array. Since time-reversal is automatically broken by propagation, our proposal does not require any dynamical modulation of the system [52,53]. In contrast to models where a synthetic dimension is encoded in momentum-space quantities [52,53] or in the light frequency [45–51], our proposed topological model is based on propagation in real space-time coordinates, which is of utmost interest in the long term to integrate local nonlinearities and realize strongly interacting photon models.

We also note that, if one is not to make the Taylor expansion in Eq. 3 and wishes to keep the complete form of the waveguide dispersion $\beta_j(\omega)$, one obtains in the co-moving frame the following form of the evolution equation in Fourier space,

$$i\frac{\partial \tilde{a}'_j}{\partial \zeta} = -\left(\beta_j(\omega' + \omega_0) - \beta_{j_{\text{ref}}}(\omega_0) - \frac{\omega'}{v_g^{(\text{ref})}}\right)\tilde{a}'_j - C(\tilde{a}'_{j+1} + \tilde{a}'_{j-1})\,. \tag{8}$$

for both this and our Schrödinger equation (Eq. 6), the propagation eigenmodes of the array are then obtained by searching for stationary solutions of this equation in the form

$$\tilde{a}'_j(\zeta, \omega') = e^{i\,\Delta\beta'\,\zeta}\,\tilde{a}'_j(\omega') \tag{9}$$

where the propagation constant in the comoving frame, $\Delta\beta'$, is related to the laboratory frame one by:

$$\beta(\omega) = \beta_{j_{\text{ref}}}(\omega_0) + \frac{\omega - \omega_0}{v_g^{(\text{ref})}} + \Delta\beta'(\omega)\,. \tag{10}$$

For visualization purposes, in the following we will study the dispersion in terms of $\Delta\beta'$, where Δ highlights that we consider propagation constants relative to a reference.

Finally, we note that, in the simplest limit where the mass is constant across the array $m_j = m$, the scalar potential vanishes, and the vector potential displays a linear gradient along j, $A_j^{(\tau)} = -Bj$, with B being a uniform magnetic field, this equation reduces to the well-known quantum Hall coupled wire model that we review in the next Section. This simple model will serve us as an intuitive guide for the following developments of the paper.

3. The quantum Hall coupled wire model

In the quantum Hall coupled wire model, a charged particle is subject to a uniform magnetic field and moves within a system of N coupled wires: the particle can either freely move along each wire (as denoted by the continuous dimension, x) or hop between neighboring wires (along the discrete dimension, y) [42]. Hence, this model lies between the fully-continuous Landau levels for a particle in free space and the fully-discrete Harper-Hofstadter model for a particle on a 2D square lattice [54]. Originally, the coupled wire model was investigated in the context of the fractional quantum Hall effect [42–44]; its interest is related to the ability to control the band flatness by varying the hopping between wires. Recently, it has also been realized experimentally using the internal atomic states as a (discrete) synthetic dimension in addition to a real spatial dimension [55].

In mathematical terms, the coupled wire model is summarized by the Hamiltonian

$$\hat{\mathcal{H}} = \frac{\hbar^2}{2m}\left(\hat{k}_x + \frac{qB}{\hbar}y\right)^2 + \hbar J \sum_y (|x, y+a\rangle\langle x, y| + \text{H.C.}), \tag{11}$$

where q and m are the particle's charge and mass along x respectively, and J is the hopping between adjacent sites along the discrete dimension y, of lattice spacing a. The magnetic field is uniform and equal to B, and a Landau gauge is adopted with the vector potential oriented along the continuous x direction, $\mathbf{A} = -By\hat{e}_x$. In our $t-z$-mapped Schrödinger equation (Eq. 6), the waveguide index j corresponds to y and the time in the co-moving frame τ corresponds to x. The hopping J corresponds to the evanescent coupling C between neighbouring waveguides and the particle mass corresponds to the (reciprocal of the) group velocity dispersion. The magnetic vector potential $-By$ corresponds to our $A_j^{(\tau)}$. We note that, if we measure k_x in units of the inverse of the magnetic length $l_B \equiv \sqrt{\hbar/qB}$ and the Hamiltonian in units of $\hbar J$, there is only one free parameter, namely the ratio of the two kinetic energy scales $r \equiv (\hbar^2/ml_B^2)/(\hbar J)$.

To gain some intuition for the physics of the coupled wire model, we take periodic boundary conditions along the continuous (x) direction, as in [42]. This allows us to exploit the conserved momentum k_x to diagonalise the Hamiltonian. An example of the coupled wire model band structure calculated from the above procedure is shown in Fig. 1(b), where the colouring of the states denotes their average position with respect to the discrete dimension.

Physically, the most important features of this band structure are the existence, at low energies, of dispersionless bulk band states and of unidirectionally propagating edge states. The former are localised in the discrete bulk (*green/blue* colouring) and have an almost constant energy, corresponding to no group velocity; as such, they are a semi-discrete analog of the flat Landau levels of charged particles subject to homogeneous magnetic field in free space. The latter are localised on the edges of the system (*yellow/purple* colouring) and their k_x-dependent energy falls in the gaps between the flat levels; these states are one-way chiral edge states with non-zero group velocity and are protected by the non-trivial topology of the model, i.e. the non-zero Chern number of the bands.

Intuitively, the appearance of these two types of states can be simply understood from Eq. 11. In the absence of the inter-wire coupling J, the dispersion consists of N parabolae (corresponding

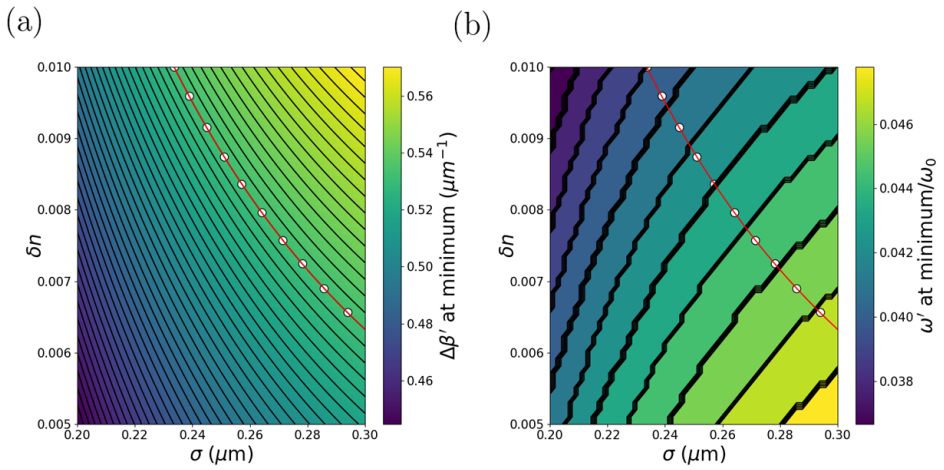

Fig. 2. Plots of (a): the co-moving frame propagation constant at the minimum of the waveguide dispersion and (b): the corresponding ω' value, each as a function of the two main model parameters. Each plot shows contour lines for each surface *(black)*, with a particular contour line of the propagation constant minimum shown in red. This red contour line is sampled to obtain the parameters for a waveguide array (white points). We use a reference waveguide with refractive index depth and width $\delta n_{\text{ref}} = 10^{-3}$ and $\sigma_{\text{ref}} = 0.1\mu$m respectively, and a carrier frequency corresponding to a wavelength of 0.5μm. Other parameters are as discussed in the Main Text.

to each of the N wires) which are equally-spaced along k_x due to the uniform magnetic field, and their minima have all the same energy. As energy increases, each parabola crosses sequentially with those of the neighbouring wires, except for the ones at the edges of the array, where neighbours are only present on one side. Turning on the inter-wire coupling J then lifts the degeneracies around the crossings, mixing states and giving rise to the bulk bands in the center of the band structure and the localised one-way states at the edges that are visible in Fig. 1(b).

In the next section we will see how this model can be naturally realized by the coupled Schrödinger equations (Eq. 6) in a suitably-designed waveguide array, and we will assess the impact of additional features such as the on-site potential V_j and position-dependent mass m_j terms.

4. An experimentally-motivated model of a laser-written waveguide array

From our discussion in the previous sections, the key ingredient to generate the synthetic magnetic field for photons is to design the j-dependence of the waveguide dispersion $\beta_j(\omega)$ in order to obtain a finite gradient along j of the group velocity. To this purpose, we consider a model of N waveguides embedded in a medium of frequency-dependent refractive index $n_0(\omega)$. Within each waveguide j, light is confined by a (frequency-independent, for simplicity) lateral spatial profile of the refractive index. More precisely,

$$n_j(x,\omega) = n_0(\omega) + \delta n_j \exp\left(-\left(\frac{x^2}{2\sigma_j^2}\right)^m\right), \tag{12}$$

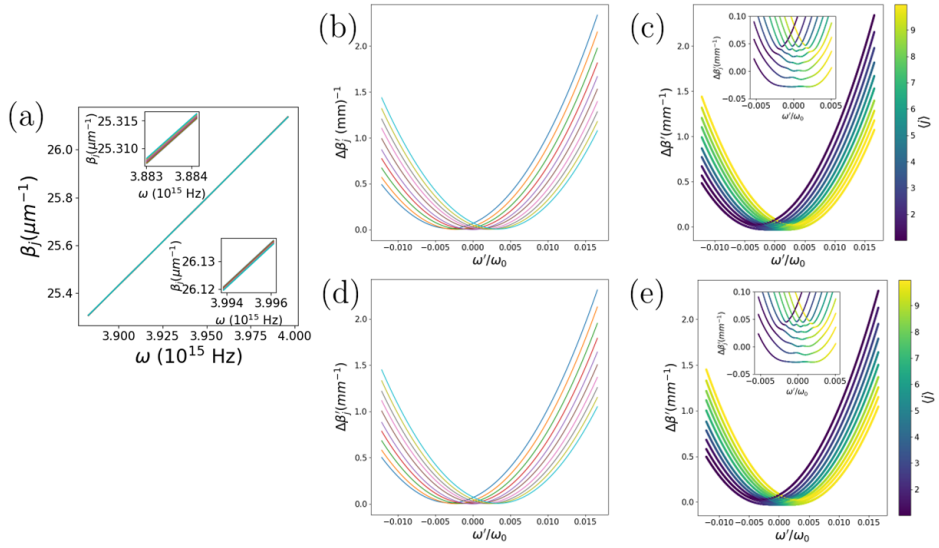

Fig. 3. (a): Propagation constants in the lab frame for an array of $N = 10$ uncoupled waveguides with refractive index profile as in Eq. 12, after the waveguide widths and refractive index perturbations have been tuned to make the co-moving frame coupled array band structure have some similar features as the quantum Hall coupled wire model. The insets show two different frequency ranges, with the order of the curves reversed between the two, showing that the curves intersect each other. (b): The uncoupled propagation constants in (a) transformed into the co-moving frame as described in the Main Text. We find minima at approximately the same propagation constant value and approximately uniform spacing in frequency. Physically, these correspond to having only a small scalar potential and a near-uniform magnetic field respectively. (c): The dispersion curves in (b) when a nearest-neighbour evanescent coupling of $C = -0.02\text{mm}^{-1}$ is included, showing avoided crossings. The colour of each state denotes the expectation value of its position with respect to the discrete direction. We see that this band structure includes bulk states (*green*) that are nearly dispersionless (see inset) and chiral edge modes (*purple/yellow*) within the gap like in the coupled wire model. (d) and (e): The uncoupled [(d)] and coupled [(e)] co-moving frame dispersions calculated from our Schrödinger equation, showing agreement with (b) and (c). Throughtout this figure, the parameters are as in Fig. 2, but for the final co-moving frame results we choose the $j = N/2$ waveguide as a reference, and a carrier frequency corresponding to the minimum of the $j = N/2$ dispersion.

where for concreteness we consider the refractive index $n_0(\omega)$ of a SCHOTT-SF glass, whose high Abbe number gives a large dispersion [56], and an experimentally motivated $m = 10$ value is taken for the super-Gaussian power of the spatial profile.

In order to obtain the synthetic magnetic field, different values of the width σ_j and the refractive index depth $\delta n_j \ll 1$ must be taken for the different waveguides. In experiments, these parameters are controlled by varying the speed at which the optical medium is translated across the beam used for writing. We calculate the dispersions $\beta_j(\omega)$ for our refractive index profile by numerically solving the Helmholtz equation for our refractive index profile [1, 20]:

$$i\frac{\partial \tilde{a}_j(x,z,\omega)}{\partial z} = -\frac{c}{2n_0(\omega)\omega}\frac{\partial^2 \tilde{a}_j(x,z,\omega)}{\partial x^2} - \frac{\omega}{c}\delta n_j \exp\left(-\left(\frac{x^2}{2\sigma_j^2}\right)^m\right)\tilde{a}_j(x,z,\omega), \tag{13}$$

which has the form of a Schrödinger equation in which the refractive index perturbation plays the role of a potential well. We write $\tilde{a}_j(x,z,\omega) = \tilde{a}_j(x,\omega)e^{i\delta\beta_j(\omega)z}$, where $\delta\beta_j(\omega)$ is the part of the propagation constant due to the waveguide itself, and we diagonalise the resulting equation. We choose the fundamental mode, and verify that the other modes are well-separated in propagation constant. This produces the total dispersion $\beta_j(\omega) \equiv n_0(\omega)\omega/c + \delta\beta_j(\omega)$. We can then employ our mapping (Eq. 10) to change to the co-moving frame.

We then need to adjust our free parameters of the array, δn_j and σ_j, to make our co-moving frame dispersion curves as close as possible to the coupled wire model (i.e. a uniform horizontal spacing between the curves corresponding to a uniform magnetic field, and the minima of the curves all being level vertically, corresponding to no on-site potential). To do this, we sweep out the $(\sigma, \delta n)$ parameter space and, for each point in the space, we find the co-moving frame dispersion $\delta\beta'(\omega')$ in the above way. Initially, we choose the co-moving frame to be defined by the reference waveguide with parameters $\delta n_{\text{ref}} = 10^{-3}$ and $\sigma_{\text{ref}} = 0.1\mu$m, and we choose a carrier frequency corresponding to a wavelength of 0.5μm. We then plot the $\Delta\beta'$ propagation constant and ω' frequency of the minimum as a function of the two model parameters. The results of this are shown in Fig. 2. To select the parameters for our array, we choose a contour of the minimum propagation constant surface in order to force all the curves to have their minima at the same value, corresponding to a vanishing on-site potential. We then sample N points from the chosen contour for an array of N waveguides (contours in red and black, with the sampled points in white). We also want the chosen parameters to correspond to frequencies of the minimum that are approximately equally-spaced, corresponding to a uniform synthetic magnetic field.

Once our array is selected, the final co-moving frame propagation constants we use are actually the result of another co-moving frame transformation, in which we now choose the reference waveguide to be the central one in the array, with $j_{\text{ref}} = N/2$, and the new carrier frequency chosen to be the frequency at the minimum of the $j_{\text{ref}} = N/2$ dispersion. This is to make our band structure as symmetric as possible about $\omega' = 0$. The end results in the lab frame are plotted in Fig. 3(a), and in the co-moving frame in Fig. 3(b).

Including the evanescent coupling C into our un-coupled dispersion and diagonalisation of the co-moving frame equation (Eq. 8) gives the eigenmodes shown in panel Fig. 3(c) and, in a magnified view, in the inset of this panel. The qualitative resemblance with the quantum Hall coupled wire model is apparent: the bottom of the dispersion forms isolated bands corresponding to almost flat Landau levels that transform into edge states on the sides of the dispersion. The color scale highlights the spatial location of the different states: as expected, Landau levels are localized in the bulk, while the chiral edge states sit on the extreme waveguides $j = 1$ (*purple*) and $j = N$ (*yellow*).

For comparison, we also calculate the band structure for the waveguide array using our Schrödinger equation (Eq. (6)). To this purpose, we use our lab frame waveguide dispersions $\beta_j(\omega)$ to calculate the effective mass, scalar on-site potential and magnetic vector potential around the reference waveguide and carrier frequency, as shown in the Supplemental Material [57]. We then diagonalize the Schrödinger equation (Eq. 6) for different values of ω' to find the propagation constants in the comoving frame. The results for no coupling ($C = 0$) and for a finite coupling C are shown in Fig. 3(d) and (e) for the same parameters as for panels (b) and (c). The agreement between the two calculations is excellent, which further confirms the power of our configuration to generate a non-trivial synthetic magnetic field and thus realize a topological quantum Hall coupled wire model. As an aside, we mention that the engineering of the photonic band structure to have quantum Hall features is not unique to this model. In the Supplemental Material, we present an analytically-solvable toy model, whose band structure we also tune to resemble the coupled wire model [57]. In the next section we will investigate observable signatures of the synthetic magnetic field on optical quantities of experimental interest.

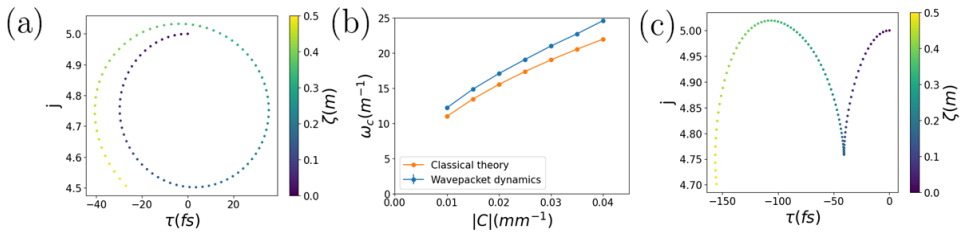

Fig. 4. (a): In our wavepacket dynamics with Eq. 9 we find cyclotron orbits, as shown here by the wavepacket center-of-mass coloured according to the position along the optical axis, ζ. (b): The frequencies of the cyclotron orbits extracted with a fit (*blue*) compared to the coupled wire model classical theory (*orange*). The small deviation between the curves is principally due to minor differences between the coupled wire model band structure and the full optical ones in Fig. 3. (c): We apply a temperature gradient across the array, corresponding to an on-site potential. Tuning the strength of this potential introduces a Hall drift into the dynamics. The parameters used are the same as Fig. 3. The example results in (a) and (c) use a coupling $C = -0.02\text{mm}^{-1}$. For the coupled-mode wavepacket dynamics, the wavepacket is prepared with an initial center-of-mass of $j_0 = 5$ and $\omega' = 0$, and with widths of $s_{\omega'} = 1/750 \times 10^{15}$Hz and $s_j = 1$. In (c) we use an electric potential of $\Delta n_j(\omega_0/c) = 0.001j\text{mm}^{-1}$.

5. Observable signatures of the synthetic magnetic field

Having engineered our waveguide band structure in the co-moving frame to resemble that of a quantum Hall coupled wire model, we now numerically demonstrate novel optical effects that result from the synthetic magnetic field. These provide the smoking gun for non-trivial topological physics in this system.

5.1. Cyclotron orbits

As a first example, we consider the optical equivalent of bulk cyclotron orbits that arise for a semiclassical charged particle in a magnetic field. As discussed above, equispaced Landau levels are present in the bulk of the coupled wire model (Fig. 1(b)). A wavepacket prepared in a suitable superposition of Landau levels will execute semiclassical cyclotron orbits, moving in a circular trajectory with the characteristic cyclotron frequency set by the level spacing and a (clockwise or anti-clockwise) direction set by the sign of the effective magnetic field. In the presence of an additional synthetic electric field, the cyclotron motion will be supplemented by a so-called 'Hall drift', that is a sideways motion perpendicular to the direction of the applied electric field.

As we now show, such orbits naturally arise for photons in our system. To this purpose, we prepare an initial Gaussian wavepacket in the $j - \omega'$ space, spatially centered in the bulk of the array and with a central frequency located in the Landau level region of the bands. The Gaussian spatial width s_j is taken of the order of the inter-waveguide spacing, while the chosen frequency-space width $s_{\omega'}$ corresponds to a Gaussian pulse duration on the order of 100fs. Such pulse durations are well within the range of standard techniques in ultrafast optics such as mode-locked lasers, and the light then has to be focussed onto the input facet of the array with the appropriate spot waist to realise the desired Gaussian spatial profile. The wavepacket is then evolved along ζ according to the Fourier-space comoving-frame evolution equation (Eq. (8)), and Fourier-transformed into $j - \tau$ space. The details of the numerical calculations throughout this section are discussed in the Supplemental Material [57].

Fig. 4(a) shows an example trajectory of the pulse center-of-mass, calculated for the waveguide array parameters used in Fig. 3. A clear cyclotron orbit is visible, where the amplitude of the

oscillations along the spatial direction j is of the order of a waveguide, so they are detectable in experiment. In order to further characterize the oscillations, we repeat these simulations for different values of the inter-waveguide coupling, which physically corresponds to varying their spacing. For each calculation, the cyclotron frequency is extracted from a fit of the ζ-evolution, the details of which are discussed in the Supplemental Material [57]. The blue line in Fig. 4(b) shows the value of the fitted cyclotron frequency as a function of the coupling C; as expected, it grows for increasing values of the coupling.

A deeper insight into the cyclotron oscillations can be obtained by comparing these numerical results with the prediction of an approximate classical calculation based on the equations of motion for a classical particle with constant, yet anisotropic masses and subject to the synthetic magnetic field according to the coupled wire model with no external potential. This calculation leads to the prediction

$$\omega_c = \frac{|\mathcal{B}|}{\sqrt{m^{(\tau)}\, m^{(j)}}} = |\mathcal{B}| \sqrt{2 \left| C\, D_{j_{\text{ref}}} \right|} \tag{14}$$

where $|m^{(\tau),(j)}| = 1/|D_{j_{\text{ref}}}|, 1/(2\,|C|)$ are the absolute values of the effective masses in the temporal and spatial directions respectively [1], and $\mathcal{B} \equiv (A^{(\tau)}_{j=10} - A^{(\tau)}_{j=1})/(N-1)$ is the approximately uniform magnetic field corresponding to our magnetic vector potential. The result of this approximate calculation is shown as an orange line in Fig. 4(b) and displays a good agreement with the numerics for the full model (*blue*). The small deviation between the two curves is principally due to the minor differences between the ideal coupled-wire model bands and our full optical results in Fig. 3. For the chosen system parameters, the typical period $\zeta_c = 2\pi/\omega_c$ of the cyclotron oscillations is of the order 10s of centimetres, and so should be accessible in experiment. It is further reduced for stronger values of the evanescent coupling and of the waveguide dispersion.

5.2. Hall drift on the pulse arrival time

We now exploit another feature of quantum Hall physics to introduce a Hall drift into the cyclotron dynamics we found above. As mentioned previously, if an additional electric field is applied to a particle in a quantum Hall system, we expect the particle to drift in the direction perpendicular to that field. We first consider applying a synthetic electric field across the array in the j-direction, which will correspond to a drift in the τ-direction. If this drift could be controlled, natural applications of the resulting delay/advance include delay lines, which have a widespread uses throughout optics, including interferometry, ultrafast optics and telecommunications.

The Hall drift can be introduced, with controllable magnitude and direction, by imposing suitable perturbations to the waveguide array, e.g. a temperature gradient along j. This induces a corresponding spatial gradient of the refractive index Δn_j along j. Formally, this can be described by including an additional term of the form:

$$i \frac{\partial \tilde{a}'_j}{\partial \zeta} = \ldots + \Delta n_j (\omega_0/c)\, \tilde{a}'_j \tag{15}$$

to the right-hand side of our model equation (Eq. 8). An elementary calculation within the coupled wire model shows that the temporal drift under a synthetic electric field $\mathcal{E}_{\text{therm}} = -(\omega_0/c)(d\Delta n_j/dj)$ in the spatial direction is equal to

$$\tau_H = -\zeta\, \frac{\mathcal{E}_{\text{therm}}}{\mathcal{B}}\,. \tag{16}$$

An example of this effect is illustrated in Fig. 4(c), where we show the appearance of the Hall drift along τ under the effect of a potential gradient as small as $\Delta n_j(\omega_0/c) = 0.001\, j\,\text{mm}^{-1}$,

[1] Depending on the relative sign of the masses in the two directions (namely of C and $D_{j_{\text{ref}}}$), the Landau levels appear for states displaying the same or opposite phases in neighboring wires.

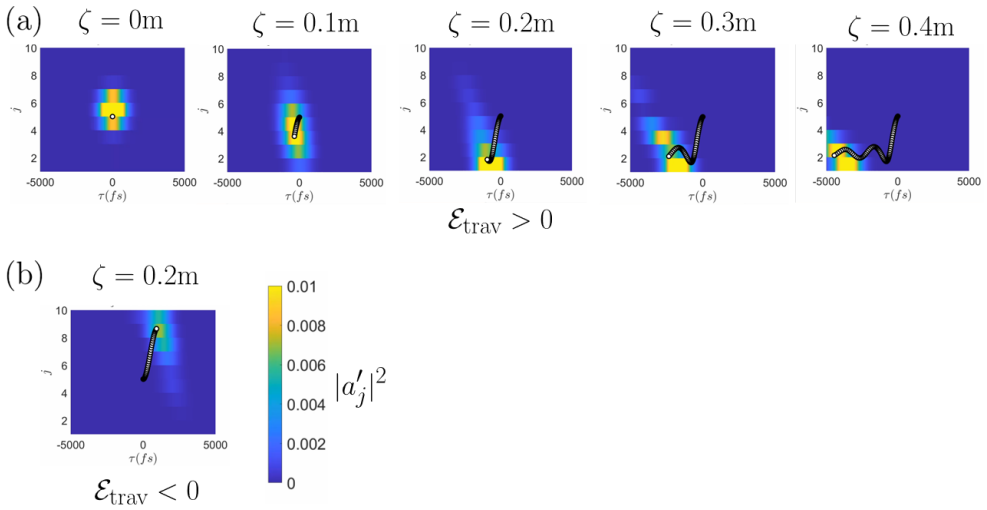

Fig. 5. (a): We apply a travelling refractive index perturbation to create an effective electric field in the τ direction, which causes a displacement of the wavepacket across the waveguides as we expect for a quantum Hall system. (b): Reversing the sign of the modulation reverses the direction of displacement. We use the same parameters as Fig. 4, but we use an electric field with magnitude $|\mathcal{E}_{\text{trav}}| = 0.0001(\text{fsmm})^{-1}$, with $\mathcal{E}_{\text{trav}} > 0$ for (a).

corresponding to a refractive index perturbation of $\sim 10^{-7}$. We note that the upper limit on the perturbation strength is due to the size of the band gap in Fig. 3(c); a perturbation of the order of or larger than the gap will introduce significant non-adiabatic effects and blur out the effect shown in Fig. 4(c).

5.3. *Hall drift in real space*

In the previous Subsection, we showed how the displacement along the τ-direction can be introduced. Now we propose a method to exploit the same quantum Hall effect to control the spatial displacement of a wavepacket across the array, i.e. along the j-direction, in response to a perturbation along the temporal τ direction.

The idea of the scheme is to implement a spatial displacement in a reconfigurable way by means of a travelling refractive index perturbation. This could be realised in experiments by means of the electro-optic or acousto-optical effects, as was recently investigated in [49, 51]. In the simplest case, we consider a refractive index perturbation that is uniform across the array and travels along the waveguides at the same speed as the reference group velocity $v_g^{(\text{ref})}$:

$$\Delta n(z,t) = \Delta\bar{n}\,\frac{z - v_g^{(\text{ref})} t}{\ell}, \tag{17}$$

where ℓ is the length of the device in z and $\Delta\bar{n}$ is the strength of the perturbation. Such a perturbation can be included in our model by adding a term of the form:

$$i\frac{\partial a'_j}{\partial \zeta} = \ldots - \mathcal{E}_{\text{trav}}\tau a'_j \tag{18}$$

to the right-hand side of the Schrödinger equation (Eq. 6), where $\mathcal{E}_{\text{trav}} = \Delta\bar{n}\,\omega_0\,v_g^{(\text{ref})}/(\ell c)$ is the synthetic electric field along the τ-direction. Two examples of light propagation under such a perturbation are shown in Fig. 5(a) and (b) for the same magnitudes of the synthetic electric field but opposite signs. We see the wavepacket, prepared in the system bulk, transported across the array towards larger or smaller j. These numerics are carried out using Eq. 9, where we include the perturbation with a term of the form $i\mathcal{E}_{\text{trav}}\partial\tilde{a}'_j/\partial\omega'$ added to the right-hand side.

We note that we could realise the same effect by instead introducing a variation of the magnetic vector potential $A_j^{(\tau)}$ in the Schrödinger equation (Eq. 6) during the evolution. According to the $t-z$ mapping, this requires us to vary the waveguide properties along the waveguide axis. Analogously to classical electrodynamics, this produces an effective synthetic electric field $\mathcal{E}_{\text{z-mod}} = -dA_j^{(\tau)}(\zeta)/d\zeta$ oriented along the τ direction which, by the quantum Hall effect, induces a drift along the orthogonal spatial direction j. As an example, this could be obtained in our setup by designing the waveguide parameters as:

$$\delta n_j(z) = \delta n_{j-wz}(z=0) \tag{19}$$

$$\sigma_j(z) = \sigma_{j-wz}(z=0) \tag{20}$$

where evaluation of the waveguide parameters at the continuous-valued $j - wz$ is obtained by interpolating their values at $z = 0$ in-between neighboring waveguides. Within the coupled wire model, this leads to

$$\mathcal{E}_{\text{z-mod}} = -\frac{dA_j^{(\tau)}(\zeta)}{d\zeta} = -w\mathcal{B}. \tag{21}$$

The corresponding Hall drift in the spatial direction can be straightforwardly evaluated to be:

$$j_H = -\zeta\,\frac{\mathcal{E}_{\text{z-mod}}}{\mathcal{B}} \tag{22}$$

Finally, we note that these two approaches are actually the same from the point of view of the band structure; both methods involve an adiabatic transport of the state along the band, corresponding to a change in the spatial position along the j-direction, as indicated by the colouring of the bands in Fig. 3(c). Note also how the displacement appears in spite of the modulation being independent of j; this further confirms its origin from the synthetic magnetic field via the quantum Hall effect.

5.4. Propagation along the edge

The plots in Fig. 5 refer to relatively short propagation distances, so that the Hall-drifted wavepackets are still within the bulk of the waveguide array. At longer propagation distances, the wavepacket can reach the spatial edge of the waveguide array at $j = 1$ or $j = N$. At this point, as is usual in topological systems under a synthetic electric field [58], the wavepacket gets converted into an edge excitation which propagates along the edge. The ensuing fast chiral motion along the spatial edge of the system is clearly visible in the plots in Fig. 5(a) as well as in the animation that is available as Supplemental Material [57]; since we are dealing with a spatial edge, the chiral motion is along the temporal τ direction, with a different sign depending on which edge the wavepacket hits. Finally, we note that we do not have an edge in the τ-direction, so any advance or delay that we see from either the temperature gradient or from this chiral edge mode propagation could be of arbitrary size.

6. Conclusions

In this work, we have demonstrated a novel framework to generate a synthetic magnetic field for light in a one-dimensional array of coupled waveguides. Based on the $t-z$ mapping of paraxial propagation of time-dependent optical pulses, a two-dimensional model is obtained in the $j-t$

plane spanned by the (discrete) waveguide index and the (continuous) temporal variable. With a suitable gradient of the waveguide properties across the array, an effective synthetic magnetic field is induced which provides an optical realization of the quantum Hall coupled wire model. Observable signatures of the synthetic magnetic effects are anticipated as a chiral cyclotron motion in the $j - t$ plane, a Hall drift in the temporal or spatial direction under the effect of a synthetic electric field directed along the array or in the temporal direction, and a fast propagation in chiral edge states.

Generalization of our scheme to physically two-dimensional waveguide arrays provides a natural way to realize three-dimensional models. Building atop available schemes for topological photonics in waveguide arrays [8, 20], this requires working with time-dependent pulses rather than monochromatic light. Future work will be devoted to the investigation of topological models involving two discrete $j_{1,2}$ coordinates and a continuous t one in our platform and the identification of observable optical signatures of the geometrical and topological properties of the band structure.

From a wider point of view, important advantages of our proposal over previous work on synthetic dimensions in photonics [20, 45] can be pointed out. Firstly, our proposal does not require any external modulation of the system and allows for a spatio-temporal manipulation of optical pulses [52, 53]. Secondly, in contrast to topological models exploiting the light frequency as a synthetic dimension [46–49] where nonlinearities would typically result in long-range interactions along the frequency direction [59], the fact that the spatial coordinates of the topological model are encoded in the waveguide index j and the temporal variable t translates a spatially local nonlinearity of the medium into local interactions in the topological model. This feature is of extreme importance [60] when one is to scale up the interaction strength and realize strongly correlated states like fractional quantum Hall liquids of light [61, 62].

7. Acknowledgements

I.C. acknowledges financial support from the Provincia Autonoma di Trento and from the Q@TN initiative. C.O. and H. M. P. are supported by the Royal Society via grants UF160112, RGF/EA/180121 and RGF/R1/180071.

References

1. R. W. Boyd, Nonlinear optics (Academic Press, London, 2008), 3rd ed.
2. A. Szameit and S. Nolte, "Discrete optics in femtosecond-laser-written photonic structures," J. Phys. B: At. Mol. Opt. Phys. **43**, 163001 (2010).
3. T. Schwartz, G. Bartal, S. Fishman, and M. Segev, "Transport and Anderson localization in disordered two-dimensional photonic lattices," Nature **446**, 52 – 55 (2007).
4. Y. Lahini, A. Avidan, F. Pozzi, M. Sorel, R. Morandotti, D. N. Christodoulides, and Y. Silberberg, "Anderson localization and nonlinearity in one-dimensional disordered photonic lattices," Phys. Rev. Lett. **100**, 013906 (2008).
5. B. Freedman, G. Bartal, M. Segev, R. Lifshitz, D. N. Christodoulides, and J. W. Fleischer, "Wave and defect dynamics in nonlinear photonic quasicrystals," Nature **440**, 1166–1169 (2006).
6. L. Levi, M. Rechtsman, B. Freedman, T. Schwartz, O. Manela, and M. Segev, "Disorder-enhanced transport in photonic quasicrystals," Science **332**, 1541–1544 (2011).
7. M. Verbin, O. Zilberberg, Y. E. Kraus, Y. Lahini, and Y. Silberberg, "Observation of topological phase transitions in photonic quasicrystals," Phys. Rev. Lett. **110**, 076403 (2013).
8. M. C. Rechtsman, J. M. Zeuner, A. Tünnermann, S. Nolte, M. Segev, and A. Szameit, "Strain-induced pseudomagnetic field and photonic Landau levels in dielectric structures," Nat. Photon **7**, 153–158 (2013).
9. S. Mukherjee, M. Di Liberto, P. Öhberg, R. R. Thomson, and N. Goldman, "Experimental observation of Aharonov-Bohm cages in photonic lattices," Phys. Rev. Lett. **121**, 075502 (2018).
10. A. Szameit, M. C. Rechtsman, O. Bahat-Treidel, and M. Segev, "$\mathcal{PT}$-symmetry in honeycomb photonic lattices," Phys. Rev. A **84**, 021806 (2011).
11. M. Segev, B. Crosignani, A. Yariv, and B. Fischer, "Spatial solitons in photorefractive media," Phys. Rev. Lett. **68**, 923–926 (1992).
12. H. S. Eisenberg, Y. Silberberg, R. Morandotti, A. R. Boyd, and J. S. Aitchison, "Discrete spatial optical solitons in waveguide arrays," Phys. Rev. Lett. **81**, 3383–3386 (1998).

13. N. K. Efremidis, S. Sears, D. N. Christodoulides, J. W. Fleischer, and M. Segev, "Discrete solitons in photorefractive optically induced photonic lattices," Phys. Rev. E **66**, 046602 (2002).
14. D. Christodoulides, F. Lederer, and Y. Silberberg, "Discretizing light behaviour in linear and nonlinear waveguide lattices," Nature **424**, 817 – 823 (2003).
15. J. W. Fleischer, M. Segev, N. K. Efremidis, and D. N. Christodoulides, "Observation of two-dimensional discrete solitons in optically induced nonlinear photonic lattices," Nature **422**, 147 – 150 (2003).
16. P.-E. Larré and I. Carusotto, "Optomechanical signature of a frictionless flow of superfluid light," Phys. Rev. A **91**, 053809 (2015).
17. Q. Fontaine, P.-É. Larré, G. Lerario, T. Bienaimé, S. Pigeon, D. Faccio, I. Carusotto, É. Giacobino, A. Bramati, and Q. Glorieux, "Interferences between Bogoliubov excitations in superfluids of light," Phys. Rev. Res. **2**, 043297 (2020).
18. M. C. Braidotti, R. Prizia, C. Maitland, F. Marino, A. Prain, I. Starshynov, N. Westerberg, E. M. Wright, and D. Faccio, "Measurement of penrose superradiance in a photon superfluid," Phys. Rev. Lett. **128**, 013901 (2022).
19. J. Steinhauer, M. Abuzarli, T. Aladjidi, T. Bienaimé, C. Piekarski, W. Liu, E. Giacobino, A. Bramati, and Q. Glorieux, "Analogue cosmological particle creation in an ultracold quantum fluid of light," Nat. Commun. **13**, 2890 (2022).
20. T. Ozawa, H. M. Price, A. Amo, N. Goldman, M. Hafezi, L. Lu, M. C. Rechtsman, D. Schuster, J. Simon, O. Zilberberg, and I. Carusotto, "Topological photonics," Rev. Mod. Phys. **91**, 015006 (2019).
21. H. Price, Y. Chong, A. Khanikaev, H. Schomerus, L. J. Maczewsky, M. Kremer, M. Heinrich, A. Szameit, O. Zilberberg, Y. Yang et al., "Roadmap on topological photonics," J. Physics: Photonics (2022).
22. M. C. Rechtsman, J. M. Zeuner, Y. Plotnik, Y. Lumer, D. Podolsky, F. Dreisow, S. Nolte, M. Segev, and A. Szameit, "Photonic Floquet topological insulators," Nature **496**, 196–200 (2013).
23. N. H. Lindner, G. Refael, and V. Galitski, "Floquet topological insulator in semiconductor quantum wells," Nat. Phys. **7**, 490–495 (2011).
24. Y. Lumer, Y. Plotnik, M. C. Rechtsman, and M. Segev, "Self-localized states in photonic topological insulators," Phys. Rev. Lett. **111**, 243905 (2013).
25. S. Mukherjee and M. C. Rechtsman, "Observation of unidirectional solitonlike edge states in nonlinear Floquet topological insulators," Phys. Rev. X **11**, 041057 (2021).
26. S. Mukherjee and M. C. Rechtsman, "Observation of Floquet solitons in a topological bandgap," Science **368**, 856–859 (2020).
27. J. Noh, S. Huang, D. Leykam, Y. D. Chong, K. P. Chen, and M. C. Rechtsman, "Experimental observation of optical Weyl points and Fermi arc-like surface states," Nat. Phys **13**, 611 – 617 (2017).
28. E. Lustig, L. J. Maczewsky, J. Beck, T. Biesenthal, M. Heinrich, Z. Yang, Y. Plotnik, A. Szameit, and M. Segev, "Three-dimensional photonic topological insulator induced by lattice dislocations," arXiv:2204.13762 [physics.optics] (2022).
29. Z. Yang, E. Lustig, Y. Lumer, and M. Segev, "Photonic Floquet topological insulators in a fractal lattice," Light Sci Appl **9** (2020).
30. Z. Fu, N. Fu, H. Zhang, Z. Wang, D. Zhao, and S. Ke, "Extended SSH model in non-Hermitian waveguides with alternating real and imaginary couplings," Appl. Sci. **10** (2020).
31. J. M. Zeuner, M. C. Rechtsman, Y. Plotnik, Y. Lumer, S. Nolte, M. S. Rudner, M. Segev, and A. Szameit, "Observation of a topological transition in the bulk of a non-Hermitian system," Phys. Rev. Lett. **115**, 040402 (2015).
32. S. Weidemann, M. Kremer, T. Helbig, T. Hofmann, A. Stegmaier, M. Greiter, R. Thomale, and A. Szameit, "Topological funneling of light," Science **368**, 311–314 (2020).
33. E. J. Meier, F. A. An, A. Dauphin, M. Maffei, P. Massignan, T. L. Hughes, and B. Gadway, "Observation of the topological Anderson insulator in disordered atomic wires," Science **362**, 929–933 (2018).
34. S. Stützer, Y. Plotnik, Y. Lumer, P. Titum, N. H. Lindner, M. Segev, M. C. Rechtsman, and A. Szameit, "Photonic topological Anderson insulators," Nature **560**, 461 – 465 (2018).
35. Y. E. Kraus, Y. Lahini, Z. Ringel, M. Verbin, and O. Zilberberg, "Topological states and adiabatic pumping in quasicrystals," Phys. Rev. Lett. **109**, 106402 (2012).
36. O. Zilberberg, S. Huang, J. Guglielmon, M. Wang, K. P. Chen, Y. E. Kraus, and M. C. Rechtsman, "Photonic topological boundary pumping as a probe of 4D quantum Hall physics," Nature **553**, 59–62 (2018).
37. M. Wimmer, H. M. Price, I. Carusotto, and U. Peschel, "Experimental measurement of the Berry curvature from anomalous transport," Nat. Phys **13**, 545 – 550 (2017).
38. T. Kitagawa, M. A. Broome, A. Fedrizzi, M. S. Rudner, E. Berg, I. Kassal, A. Aspuru-Guzik, E. Demler, and A. G. White, "Observation of topologically protected bound states in photonic quantum walks," Nat Commun **3** (2012).
39. Y. Lai and H. A. Haus, "Quantum theory of solitons in optical fibers. I. time-dependent Hartree approximation," Phys. Rev. A **40**, 844–853 (1989).
40. Y. Lai and H. A. Haus, "Quantum theory of solitons in optical fibers. II. exact solution," Phys. Rev. A **40**, 854–866 (1989).
41. P.-E. Larré and I. Carusotto, "Propagation of a quantum fluid of light in a cavityless nonlinear optical medium: General theory and response to quantum quenches," Phys. Rev. A **92**, 043802 (2015).
42. C. L. Kane, R. Mukhopadhyay, and T. C. Lubensky, "Fractional quantum Hall effect in an array of quantum wires," Phys. Rev. Lett. **88**, 036401 (2002).
43. J. C. Y. Teo and C. L. Kane, "From Luttinger liquid to non-Abelian quantum Hall states," Phys. Rev. B **89**, 085101

(2014).
44. J. C. Budich, A. Elben, M. Łącki, A. Sterdyniak, M. A. Baranov, and P. Zoller, "Coupled atomic wires in a synthetic magnetic field," Phys. Rev. A **95**, 043632 (2017).
45. L. Yuan, Q. Lin, M. Xiao, and S. Fan, "Synthetic dimension in photonics," Optica **5**, 1396–1405 (2018).
46. T. Ozawa, H. M. Price, N. Goldman, O. Zilberberg, and I. Carusotto, "Synthetic dimensions in integrated photonics: From optical isolation to four-dimensional quantum hall physics," Phys. Rev. A **93**, 043827 (2016).
47. L. Yuan, Y. Shi, and S. Fan, "Photonic gauge potential in a system with a synthetic frequency dimension," Opt. Lett. **41**, 741–744 (2016).
48. A. Dutt, L. Yuan, K. Y. Yang, K. Wang, S. Buddhiraju, J. Vučković, and S. Fan, "Creating boundaries along a synthetic frequency dimension," Nat. Commun. **13**, 3377 (2022). ArXiv:2203.11296 [cond-mat, physics:physics, physics:quant-ph].
49. K. Wang, B. A. Bell, A. S. Solntsev, D. N. Neshev, B. J. Eggleton, and A. A. Sukhorukov, "Multidimensional synthetic chiral-tube lattices via nonlinear frequency conversion," Light. Sci. & Appl. **9**, 132 (2020). Number: 1 Publisher: Nature Publishing Group.
50. Y. Hu, C. Reimer, A. Shams-Ansari, M. Zhang, and M. Loncar, "Realization of high-dimensional frequency crystals in electro-optic microcombs," Optica **7**, 1189–1194 (2020).
51. F. S. Piccioli, A. Szameit, and I. Carusotto, "Topologically protected frequency control of broadband signals in dynamically modulated waveguide arrays," Phys. Rev. A **105**, 053519 (2022).
52. T. Ozawa, "Artificial magnetic field for synthetic quantum matter without dynamical modulation," Phys. Rev. A **103**, 033318 (2021).
53. L. Nemirovsky, M.-I. Cohen, Y. Lumer, E. Lustig, and M. Segev, "Synthetic-space photonic topological insulators utilizing dynamically invariant structure," Phys. Rev. Lett. **127**, 093901 (2021).
54. D. R. Hofstadter, "Energy levels and wave functions of Bloch electrons in rational and irrational magnetic fields," Phys. Rev. B **14**, 2239–2249 (1976).
55. T. Chalopin, T. Satoor, A. Evrard, V. Makhalov, J. Dalibard, R. Lopes, and S. Nascimbene, "Probing chiral edge dynamics and bulk topology of a synthetic hall system," Nat. Phys. **16**, 1017–1021 (2020).
56. M. Polyanskiy, "Optical constants of SCHOTT - SF (Dense flint)," .
57. See Suppl. Material .
58. D. De Bernardis, F. Piccioli, P. Rabl, and I. Carusotto, "Chiral quantum optics in the bulk a photonic quantum Hall system," arXiv p. xxx (2023).
59. T. Ozawa and I. Carusotto, "Synthetic dimensions with magnetic fields and local interactions in photonic lattices," Phys. Rev. Lett. **118**, 013601 (2017).
60. T. Ozawa and H. M. Price, "Topological quantum matter in synthetic dimensions," Nat. Rev. Phys. **1**, 349–357 (2019).
61. I. Carusotto and C. Ciuti, "Quantum fluids of light," Rev. Mod. Phys. **85**, 299 (2013).
62. I. Carusotto, A. A. Houck, A. J. Kollár, P. Roushan, D. I. Schuster, and J. Simon, "Photonic materials in circuit quantum electrodynamics," Nat. Phys. **16**, 268–279 (2020).

Supplemental Material for "Artificial gauge fields in the t-z mapping for optical pulses: spatio-temporal wavepacket control and quantum Hall physics"

We cover three topics in this Supplemental Material. In Sec. 1, we discuss a simple, analytically-solvable toy model for a 1D coupled waveguide array, which we use to demonstrate that the idea of engineering the co-moving frame band structure to have quantum Hall features is quite general and not specific to the particular model chosen. For the other two sections, we return to the experimentally-motivated model introduced in the Main Text. In Sec. 2, we show the calculation of the Schrödinger equation effective mass, magnetic vector potential and on-site potential which we use in some of the results in the Main Text. Finally, in Sec. 3, we give the technical details of the wavepacket dynamics numerical simulations and data analysis that are employed in the Main Text.

1. An Analytical Toy Model for Coupled Waveguides

To further demonstrate the engineering of non-trivial magnetic field effects from tuning waveguide parameters as discussed in the Main Text, we now consider a simple, analytical model for a coupled waveguide array, consisting of metal waveguides each with a refractive index profile n_j. We can exactly solve the paraxial Helmholtz equation to find that the TE_{10} modes, which we choose for simplicity, have the dispersion [1]:

$$\beta_j(\omega) = \frac{n_j}{c}\sqrt{\omega^2 - \omega_c^{(j)2}}, \tag{S1}$$

where $\omega_c^{(j)} = \pi c/(L_x^{(j)} n_j)$ is the cutoff frequency in waveguide j, below which no modes can propagate. The cutoff frequency depends on the waveguide width $L_x^{(j)}$ which we allow one to spatially vary in order to engineer a non-trivial magnetic field. In particular, we choose $L_x^{(j)} = L_0 + \Delta L\sqrt{j}$ to ensure that the spacing between adjacent dispersion curves is approximately constant to approach the case of a uniform magnetic field.

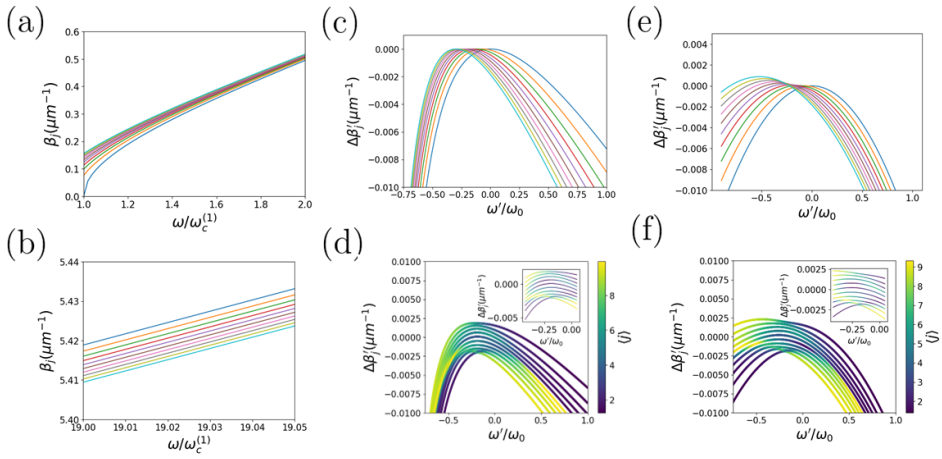

Fig. S1. (a): Propagation constants in the lab frame for our toy model. The blue labelled curve is the dispersion for waveguide $j = 1$. (b): The dispersion curves in (a) for larger frequencies, showing that the order of the curves has reversed and hence that the dispersions cross over each other. (c): Direct mapping of the dispersions in (a) to the co-moving frame using our modified Doppler shift. We see the maxima of the dispersion curves all have the same $\Delta\beta_j'$ value as we expect. (d): Results in (c) now including a coupling between neighbouring waveguides, showing avoided crossings. This results in a band structure resembling the coupled wire model, including bulk Landau levels (c.f. inset) and chiral edge modes in the gap. (e): Propagation constants in the co-moving frame for this model calculated using our Schödinger equation without any coupling, showing qualitative agreement with our analytical results in (c). (f): Results in (e) including a coupling between neighbouring waveguides. Throughout, we use $N = 10$ waveguides with $L_0 = 10\mu$m, $\Delta L = 1\mu$m and $n_1 = 1.5$, and we take $\omega_0 = 10\omega_c^{(1)}$. We take the coupling to be $C = 10^3\mu\text{m}^{-1}$.

We can now transform the dispersion into the co-moving frame using the mapping in the Main Text (Eq. 10). Note that, in the co-moving frame, we actually plot $\Delta\beta_j'(\omega') = \beta_j'(\omega') - \beta_{\text{ref}}'(0)$ for consistency with our definition of propagation constants in our Schrödinger equation. In this model, we choose the reference waveguide to be the $j = 1$ waveguide in the array. We can then use the transformed dispersions to tune the refractive index n_j such that the maxima of the dispersions in the co-moving frame all take the same value, which makes the resultant band structure as similar as possible to the coupled wire model (discussed in the Main Text). We tune our refractive index profile as:

$$n_j = \frac{n_1}{\sqrt{1 + \left(\frac{\omega_c^{(1)}}{\omega_0}\right)^2 \left(\left(\frac{L_x^{(j)}}{L_x^{(1)}}\right)^2 - 1\right)}} \tag{S2}$$

which we calculate by differentiating our transformed propagation constants with respect to ω' and enforcing that the maxima are all equal in $\Delta\beta_j'$. The resulting dispersions in both frames are shown in Fig. S1(a), (b) and (c). In the lab frame, we see a set of dispersion curves that cross over each other (c.f. the reversed order of the curves in (a) vs. (b)). In the co-moving frame, we have a set of curves with maxima that are all at the same $\Delta\beta_j'$ value as expected from our chosen refractive index profile (c.f. panel (c)). Introducing a coupling between neighbouring waveguides results in avoided crossings (Fig. S1(d)), and we see a band structure that resembles

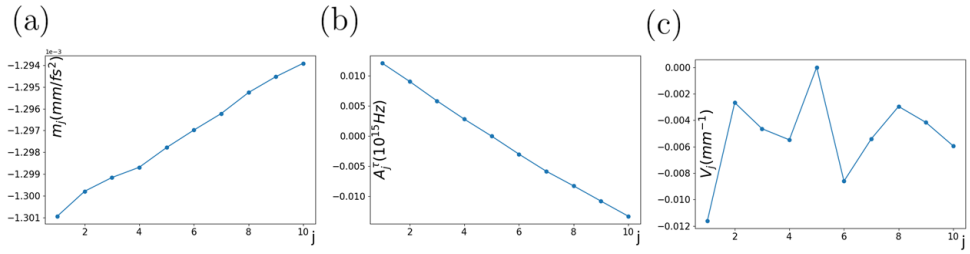

Fig. S2. Effective mass, magnetic vector potential and on-site potential in panels (a), (b) and (c) respectively for our Schrödinger equation, calculated from data in Fig. 3 in the Main Text. We see a weakly-varying effective mass, near-linear magnetic vector potential (corresponding to a uniform magnetic field) and a small residual on-site potential.

that of the quantum Hall coupled wire model (c.f. Fig. 1(b) in the Main Text). In particular, we see flat Landau level states in the bulk and chiral edge states in the gap, which is characteristic of quantum Hall systems.

We can also calculate the band structure from our Schrödinger equation (Eq. 6 in the Main Text) by using our propagation constants (Eq. S1) to calculate m_j, $A_j^{(\tau)}$ and V_j, and then writing $a'_j(\zeta,\omega') = a'_j(\omega')e^{i(\beta'\zeta-\omega'\tau)}$ and diagonalising the resulting Hamiltonian. Example results are shown in Fig S1(e) and (f), without and with an inter-waveguide coupling respectively. Comparing to the corresponding exact results in (c) and (d), we see that, as expected, the Schrödinger equation captures the dispersions very well close to $\omega' = 0$ because the truncated Taylor expansion is most accurate there. Moving away from $\omega' = 0$ in either direction leads to disagreement between the two approaches, most notably in the heights of the maxima not being identical in (e), leading to dispersion even in the flat Landau level states in (f). Finally, we note that the bands we find for this model are inverted relative to the bands for the experimentally-motivated model we consider in the Main Text (i.e. the bands for the toy model have stationary points that are maxima, not minima). This is because the group velocity dispersions in the two models have opposite signs. Overall, these results therefore demonstrate that we do not require a complex model to engineer the kind of physics we find here.

2. Schrödinger equation effective mass, magnetic vector potential and on-site potential

In this section, we show the results of using the waveguide dispersions calculated in the Main Text to find the effective mass, magnetic vector potential and on-site potential in the Schrödinger equation, which we then use to calculate some of the results in Fig. 3. We use the lab-frame propagation constants (Fig. 3(a)) and evaluate the three quantities using Eq. 7 in the Main Text. The results are shown in Fig. S2. We see a near-constant effective mass (with variation on the order 1% across the array), a magnetic vector potential that is very close to linear in j (corresponding to a uniform magnetic field), and a very small on-site potential.

3. Details of Wavepacket Dynamics Simulations

As discussed in the Main Text, we use wavepacket dynamics simulations to investigate bulk cyclotron orbits and other physical observables. We prepare a Gaussian wavepacket of the form:

$$\tilde{a}'_j(\zeta=0,\omega') = Ae^{ik_j(j-j_0)}e^{-\frac{(j-j_0)^2}{2s_j^2}} \times (j \to \omega'), \tag{S3}$$

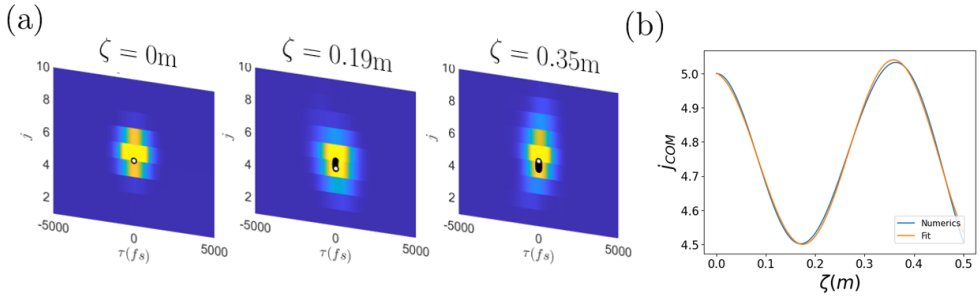

Fig. S3. (a): Example wavepacket density in the co-moving frame time domain for a Gaussian wavepacket prepared in the bulk. We see part of a cyclotron orbit with a Hall drift. (b): Plot of the center-of-mass of the wavepacket in (d) in the discrete direction as a function of ζ together with a fit to Eq. S6, showing that the fitting function captures our data very well, and can be used to extract the cyclotron frequency. We use the same parameters as the wavepacket dynamics simulations in Fig. 4 in the Main Text, with a coupling $C = -0.02\text{mm}^{-1}$.

where A is a normalisation constant; k_j is the wavepacket momentum in the j direction; j_0 is the initial center-of-mass position and s_j is the wavepacket width along j. $(j \to \omega')$ indicates we use the same form for the ω' part of the wavepacket. We choose the wavepacket to be localised in the j-bulk and to have an initial frequency in the bulk part of the bands in order to target Landau level states. We then numerically propagate the wavepacket through the array by discretising the ω' dimension into $M \gg 1$ points and hence representing our initial wavepacket as an NM-component column vector $\underline{a}(\zeta = 0)$. We then evolve the initial vector via:

$$\underline{a}(\zeta + \delta\zeta) = e^{-iH\delta\zeta}\underline{a}(\zeta), \tag{S4}$$

where $\delta\zeta$ is our small 'timestep' and H is the $NM \times NM$ matrix representing the right-hand side of the coupled mode equation (Eq. 8 in the Main Text) in our finite difference basis. More precisely, we have:

$$H = H_{\text{diag}} - \begin{pmatrix} 0 & C & 0 & \cdots & 0 \\ C & \ddots & \ddots & \ddots & \vdots \\ 0 & \ddots & & & 0 \\ \vdots & \ddots & & & C \\ 0 & \cdots & 0 & C & 0 \end{pmatrix} \otimes I_{\omega'}, \tag{S5}$$

where H_{diag} is a diagonal matrix formed by placing (-1 times) the discretised co-moving frame propagation constants $\beta_j(\omega) - \beta_{j_{\text{ref}}}(\omega_0) - \omega'/v_g^{(\text{ref})}$ along the main diagonal. The second term, representing the coupling between neighbouring waveguides, is an $N \times N$ tridiagonal matrix with the couplings inserted on to the two diagonals either side of the main diagonal. We then Fourier transform the state with respect to ω' to map it into τ-space, and consider the corresponding $j - \tau$ density as a function of ζ. An example of the wavepacket density for the optical model is shown in Fig. S3(a), corresponding to the center-of-mass trajectory in Fig. 4 in the Main Text. We use this density to calculate the wavepacket center-of-mass as a function of ζ, $j_{\text{COM}}(\zeta)$ and $\tau_{\text{COM}}(\zeta)$.

When investigating bulk cyclotron orbits, we fit to the $j_{\text{COM}}(\zeta)$ trajectory using the function:

$$f(\zeta) = A\sin(\omega_c\zeta + \phi)e^{-g\zeta} + B, \tag{S6}$$

and extract the cyclotron frequency ω_c, an example of which is shown in Fig. S3(b). We choose this function because we expect cyclotron orbits to be circular trajectories in (j, τ). We include an exponential damping factor to take into account the small damping seen in some of our numerics. We see that the fit captures our numerical data well. We note that, for large coupling, the wavepacket trajectory becomes more elongated along the j-direction, which introduces some edge effects into the dynamics. However, the frequency of the cyclotron orbit can still be well-obtained with our above fitting function.

As discussed in the Main Text, besides the bulk cyclotron orbits, we also investigate two other physical observables. The first is a travelling refractive index perturbation. We model this with a term of the form $i\mathcal{E}_{\text{trav}}\partial\tilde{a}'_j/\partial\omega'$ which corresponds, in the Schrödinger equation, to an effective electric field along the τ direction, $-\mathcal{E}_{\text{trav}}\tau a'_j$. We include this term within our numerical scheme by representing the $\partial/\partial\omega'$ operator by a standard $M \times M$ finite difference first derivative matrix $d_{\omega'}$. We hence include the term in our total finite difference matrix as $H \rightarrow H + i\mathcal{E}_{\text{trav}} I_j \otimes d_{\omega'}$, where I_j is the $N \times N$ identity matrix. Finally, we also consider applying a temperature gradient across the array, which we model with a term of the form $\Delta n_j(\omega_0/c)\tilde{a}'_j$, where we choose $\Delta n_j = Uj$. We include this in our numerical scheme by $H \rightarrow H + UJ \otimes I_{\omega'}$, where $J = \text{diag}(1, ..., N)$ and $I_{\omega'}$ is the $M \times M$ identity matrix.

References

1. I. Grant and W. Phillips, *Electromagnetism* (Wiley, Chicester, 2004), 2nd ed.

CHAPTER 4

QUANTUM SIMULATION USING ELECTRIC CIRCUITS OF COAXIAL CABLES

In this final main chapter, we present a proposal to use electric circuits of coaxial cables as a quantum simulator. We begin by motivating this idea by appealing to established circuit QED techniques. We then introduce our system of interest, namely a 2D brick wall lattice formed from coaxial cables and T-shaped connector elements. We explain in detail the physics of wave propagation in such a lattice, and present a calculation of the Bloch wave dispersion. We then demonstrate techniques to control the interesting features of this dispersion by altering the properties of some of the coaxial cables in each unit cell, and indicate some of the interesting physics that could then be realised with this.

4.1 Motivation via Circuit QED

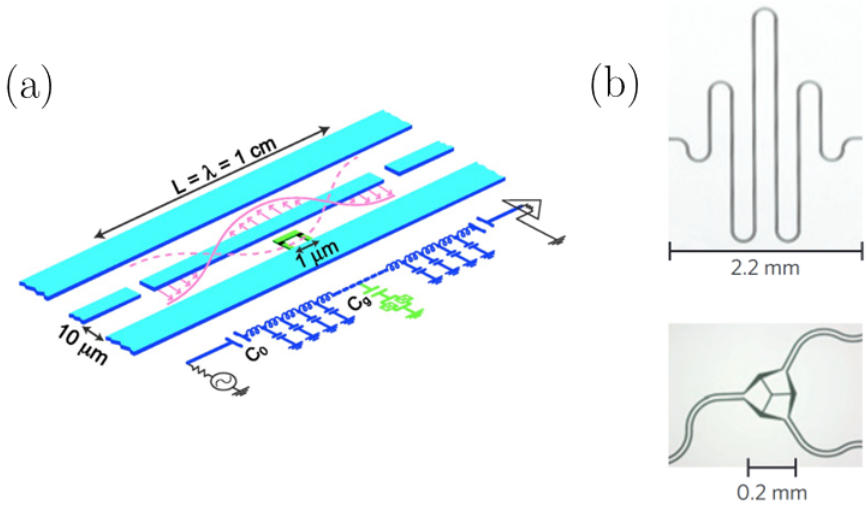

Figure 4.1: (a): Schematic of a co-planar waveguide resonator, consisting of a single-wavelength (λ) section of superconducting co-planar waveguide (*turquoise*), together with a superconducting qubit (*green*) which mediates interactions between the microwave photons. The corresponding lumped-element circuit is also shown. (b): Experimental images of a resonator (top) and capacitive coupling of resonator endpoints (bottom). Panel (a) adapted from [124] and panel (b) adapted from [125].

Circuit QED is a major sub-field of quantum simulation and quantum information, which is concerned with the quantum electrodynamics (QED) of microwave photons in electric circuits [126]. We begin by briefly outlining the idea of circuit QED from the quantum simulation point of view. At the theoretical level, the photons are the quanta of the

electromagnetic field in lumped LC circuits, where we can neglect dissipation due to the system being cooled to superconducting temperatures, as will become relevant momentarily. We will also discuss the details of the concrete experimental realisation of such LC circuits shortly. The individual LC resonators can then be coupled via capacitances. This setup can then be exploited to realise a tight-binding model of microwave photons hopping via the capacitive coupling in a chosen lattice geometry.

Crucially, strong photon-photon interactions can then be engineered by the introduction of superconducting Josephson tunnel junction elements owing to the very strong coupling between the microwave photons and the Josephson elements. In this way, circuit QED platforms have been exploited in beautiful experiments to realise materials made from photons ('photonic materials') [12]. Note that all this is in stark contrast to the behaviour of light in free space, since free-space photons have no mass or charge, and do not interact with each other (at least practically). As an aside, we highlight that we took a point of view that focuses on the microwave photons themselves for quantum simulation applications, but circuit QED has also emerged as a leading platform in digital quantum computing [127]. This side of the field focuses instead on the superconducting elements, which behave as artificial atoms with a set of discrete energy levels. These elements can therefore be thought of as qubits and used to store quantum information, and are manipulated and measured by the microwave photons.

To motivate the work we present in this final chapter, we now focus on the experimental details of the LC oscillator components of circuit QED systems. One experimental approach is to fabricate microwave co-planar waveguide (CPW) resonators, which can be thought of as the 2D equivalent of coaxial cables [126, 128–131]. A typical resonator is shown both schematically and physically in Fig. 4.1. The lattice is formed when the resonators are brought into contact at their endpoints (Fig. 4.1(b)), introducing a capacitive coupling. A Hamiltonian for the lattice can then be derived:

$$\hat{H} = \sum_i \omega_0 a_i^\dagger a_i + \frac{1}{2}\omega_0 C \sum_{\text{endpoints}} \Phi^- \Phi^+, \tag{4.1}$$

where $a_i^\dagger$ is the creation operator for a microwave photon in the resonator i with resonant frequency ω_0, C is the capacitance coupling between the resonator endpoints and $\Phi^\pm$ are the generalised fluxes (related to to the voltage) on either side of the capacitance. This can be re-written explicitly as a tight-binding Hamiltonian:

$$\hat{H}_{TB} = \sum_i \omega_0 a_i^\dagger a_i - \sum_{\langle i,j \rangle} (t_{ij} a_i^\dagger a_j + \text{H.C.}), \tag{4.2}$$

where the hopping $t_{ij} = -\frac{1}{2}\omega_0 C \phi_i^{(\text{end})} \phi_j^{(\text{end})}$, where $\phi_i^{(\text{end})}$ is the wavefunction in resonator i evaluated at the endpoint. A crucial property of such systems is that the resonant frequencies and hoppings do not depend on the precise geometry of the system itself, in stark contrast to, for example, electrons in a tight-binding solid. This property allows for the engineering of more exotic models with complicated connectivities by simply changing the wiring of the circuit.

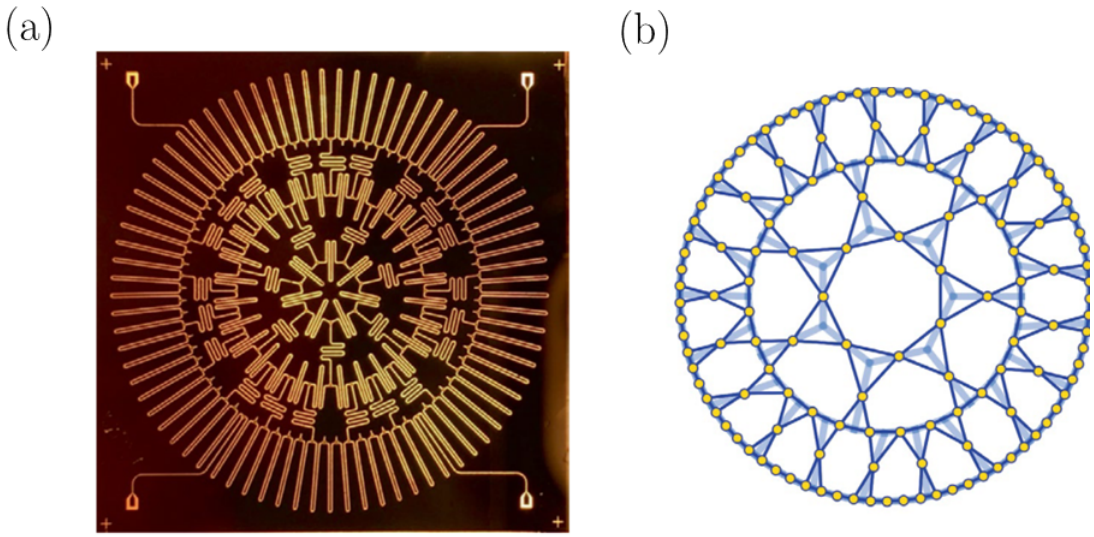

Figure 4.2: (a): Experimental image and (b): schematic diagram of a heptagonal honeycomb lattice of co-planar waveguides (CPWs) with capacitive couplings. In (b), the layout lattice corresponding to the device in (a), with edges representing the CPWs, is shown in light blue. The modal or line-graph lattice, where lattice sites are associated with the CPWs and edges are inserted according to the capacitive couplings, is shown in dark blue (edges) and yellow (sites). Figure adapted from [12].

For example, CPW lattices allow the global topology of the system of interest to be

controlled, for example by introducing periodic boundary conditions [132]. The link between the global topology of the space and the ground state degeneracy of systems such as fractional quantum Hall fluids, and the connections between these strongly-correlated fluids and topological quantum computing, make this an exciting prospect for both fundamental physics and applications [24]. Complex connectivities can also be exploited to engineer models in which the particles effectively live in non-Euclidean geometries, which have connections to the study of quantum field theories in curved spacetimes. In some of these geometries, the particles also experience destructive interference, leading to the emergence of flat bands in which particles have no kinetic energy, so that interaction effects dominate [133, 134], provided that the flat band is energetically isolated from any dispersive bands. A famous example of a CPW lattice realising a tight-binding model on a curved geometry is shown in Fig. 4.2 [128], with the physical device shown in panel (a) and the lattice shown in panel (b) (discussed in more detail below).

The physics of CPW lattices can, in the Euclidean case, be investigated by diagonalising the Hamiltonian and hence finding the dispersion of Bloch waves in the usual way [129]. However, the lattices admit a beautiful graph-theoretic description which allows the dispersion to be calculated in a simple way, and which also applies to non-Euclidean geometries for which there is no Bloch band theory, as we now discuss. As suggested in the description above, the lattice naturally formed by the connected CPW resonators (which we refer to as the layout lattice) is not the lattice whose dispersion we actually want. The CPW resonators form the edges of the layout lattice, and the connection points form the sites. However, the modes which are capacitively coupled 'live' on the CPW resonators, i.e. on the edges of the physical lattice. This suggests that we should construct a new lattice whose sites are the edges of the layout lattice and whose edges are inserted according to the capacitive coupling in the layout lattice. We refer to this second lattice as the 'modal' lattice, and we want to find the dispersion of Bloch waves propagating in it. The two types of lattice are exemplified in Fig. 4.2(b), where the layout lattice is shown in light blue, and the sites and edges of the modal lattice are

denoted by the yellow points and dark blue lines respectively. This idea can be formalised using the language of graph theory [129]. We associate a graph X with the layout lattice in the natural way, by associating vertices with the lattice sites and edges with the edges in the lattice. The graph corresponding to the modal lattice is known in the graph theory literature as the line graph of the graph X, denoted by $L(X)$. A theorem then relates the Bloch wave dispersions on the two lattices:

$$E_{L(X)} = \begin{cases} d - 2 + E_X \\ -2 \end{cases} , \tag{4.3}$$

where E_X and $E_{L(X)}$ denote the energies for the layout lattice and modal lattice respectively, and d is the coordination number of the layout lattice X. In other words, we simply shift the dispersion of the layout lattice and insert a flat band. If the lattice is carefully chosen, the flat band may be energetically isolated, making it useful for simulation interacting models as mentioned above. For example, the flat band that emerges in the Kagome lattice is not isolated, but the heptagonal honeycomb lattice in Fig. 4.2 does feature an isolated flat band.

The CPW resonator lattices, whilst extremely powerful, do have some limitations. In particular, the circuits are fabricated using a relatively complicated lithographic procedure, which also fixes the lattice geometry and precludes any dynamical changes to the structure on-the-fly. They also need to be cooled to superconducting temperatures before they can be used. In short, the CPW lattices suffer from some practical experimental difficulties. Given that CPWs are 2D analogs of coaxial cables, a natural question to ask is whether we could investigate similar physics by constructing lattices formed by standard, commercially-available coaxial cables connected by standard connector elements. Such a system could have the major advantage of the CPW lattices, namely the decoupling of the relevant physical parameters from the circuit geometry, without the practical limitations listed above. Although, we note that we would not be working in the strongly-correlated quantum regime, which would preclude the investigation of physics such as the fractional

quantum Hall effect.

As an aside, we note an alternative approach is to use classical electric circuits to simulate lattice models. One can consider lattices formed from inductors, resistors and capacitors (LRC circuits), in which the circuit Laplacian plays the role of a Hamiltonian for a lattice model, which can be engineered to target some chosen system [135]. Such lattices have been used to realise topological models such as the SSH model [135, 136] (in this context, they are known as 'topolectrical circuits'). This approach also has the advantage of the effective Hamiltonian (the circuit Laplacian in this case) not depending on the geometry of the circuit itself, only the connectivity. These lattices can therefore also be used to explore models of higher dimensionality [137–139], or models on spaces that are curved and/or have non-trivial global topology. We also note that there are a small number of works from around 20 years ago that consider the properties of coaxial cable lattices (where they are known as 'photonic crystals', but are distinct from photonic crystals in which the microscopic structure of the material is engineered to give desired optical properties) [140–144]. These works consider, for instance, the effect of nonlinearities and defects in lattices of this type, but they are more focused on applications in photonics, as opposed to the simulation of physics models.

In the remainder of this chapter, we present an early foray into using lattices of coaxial cables for quantum simulation, inspired by circuit QED as discussed above. We first present the relevant theory of signal propagation in coaxial cables, namely the transmission line equation. We then consider a simple but non-trivial brick wall lattice of coaxial cables and three-port T-shaped connector elements. We present a general technique to find the dispersion of Bloch waves in lattices of coaxial cables, and demonstrate it on the brick wall lattice. Note that the calculation of the dispersion is achievable in the CPW case using standard tools, because the lattice is naturally in the tight-binding limit. We do not have such a Hamiltonian description in our coaxial cable systems, so we need an alternative way to find the dispersion, which allows us to understand whether we are in the tight-binding or nearly-free limit, and to generally characterise the physics of the

system. We find that the dispersion includes a flat band and two dispersive bands, and that the dispersive bands touch at two Dirac points. The aforementioned graph theory description partially motivates our choice of the brick wall lattice; the line graph lattice for this system is the Kagome lattice, whose dispersion includes a flat band. If such a flat band were present in our lattice and could be gapped, it would be an excellent way to study interacting physics, because the kinetic energy has been quenched. The other reason we choose this lattice is more practical; the brick wall lattice is relatively simple and natural to engineer in experiment using commercial coaxial cables and T-connectors. We note that this work complements two recent works on realising the SSH model in 1D coaxial cable lattices [145, 146].

Once we find the dispersion of Bloch waves in our chosen lattice, we move on to consider tuning the lattice parameters, in particular the impedance of the cables. We show that this provides a natural and simple way to control the features of the band structure. In particular, we show that the aforementioned Dirac points can be gapped and shifted around the Brillouin zone, suggesting connections to the theory of strained graphene and the artificial magnetic fields that can be engineered there. We also show that a family of energetically-isolated flat bands can be engineered, suggesting that the effects of nonlinearities would be of interest. We therefore demonstrate the potential of this platform to engineer rich physics.

4.2 A Brick Wall Lattice of Identical Coaxial Cables

We begin by reviewing the relevant physics of wave propagation in isolated coaxial cables [147]. We model a coaxial cable as a lossless transmission line, where we have two long, parallel conductors with no resistance separated by an insulator. We take the line to have a capacitance per unit length κ and a self-inductance per unit length λ. We write the current flowing through the conductors and voltage across them at position x along the line and time t as $I(x,t)$ and $V(x,t)$ respectively. The geometry of the transmission

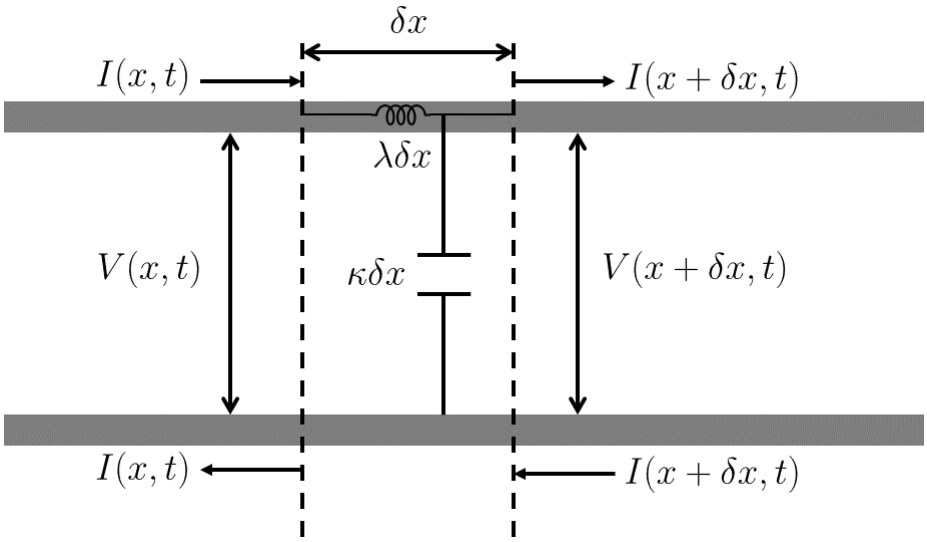

Figure 4.3: Diagram of a section of lossless transmission line, with the two parallel conductors in grey. We consider a short length of line of size δx, and derive equations describing the propagation of current and voltage waves $I(x,t)$ and $V(x,t)$. The lumped-circuit elements representing the inductance and capacitance of the short section, important in the derivation, are also shown.

line is shown in Fig. 4.3. Over some small length of transmission line δx we have:

$$V(x+\delta x,t) - V(x,t) \approx \frac{\partial V}{\partial x}\delta x = -\lambda\delta x\frac{\partial I}{\partial t}, \tag{4.4}$$

using the definition of the self-inductance. Taking the limit $\delta x \to 0$, this leads to:

$$\frac{\partial V}{\partial x} = -\lambda\frac{\partial I}{\partial t}. \tag{4.5}$$

We can also write an expression for the current flow in the short segment:

$$I(x+\delta x,t) - I(x,t) \approx \frac{\partial I}{\partial x}\delta x = -\kappa\delta x\frac{\partial V}{\partial t}, \tag{4.6}$$

which follows from the definition of capacitance. Again, taking the limit $\delta x \to 0$, this leads to:

$$\frac{\partial I}{\partial x} = -\kappa\frac{\partial V}{\partial t}. \tag{4.7}$$

Differentiating the above two equations with respect to x and t respectively and combining the results leads to:

$$\frac{1}{\kappa\lambda}\frac{\partial^2 V}{\partial x^2} = \frac{\partial^2 V}{\partial t^2}. \tag{4.8}$$

We therefore find the 1D wave equation, with the speed of the waves being $v = 1/\sqrt{\kappa\lambda}$. Note that an identical equation holds for $I(x,t)$ also. This means that we can write the general solution for waves in the transmission line as:

$$V(x,t) = f(x-vt) + g(x+vt),\ \ I(x,t) = \frac{1}{Z}(f(x-vt) - g(x+vt)), \tag{4.9}$$

where Z is the cable impedance and where f and g are arbitrary functions describing waves propagating in the $+x$ and $-x$ directions respectively.

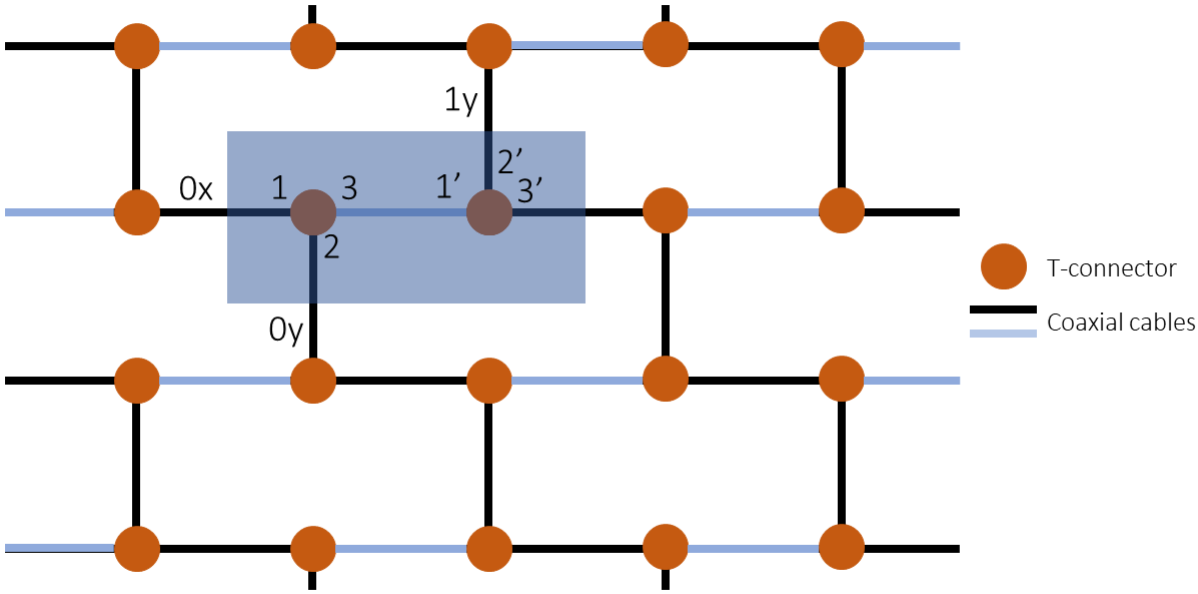

Figure 4.4: Diagram of the brick wall lattice of coaxial cables (black/blue lines) and T-connector elements (orange circles), with a unit cell marked in blue. The labels on the unit cell denote the various modes we use in the calculation of the dispersion. In this simple case, all cables have identical impedance and length. In later cases, the central cable in each unit cell, coloured blue, may have either a different impedance of length relative to the other cables.

We now move on to consider a brick wall lattice formed by coaxial cables and T-

connector elements (Fig. 4.4), where all the cables have the same length l and impedance Z, and where the T-connectors play the role of lattice sites, with the cables as the bonds between them. We work with the unit cell shown by the blue rectangle in Fig. 4.4. The approach to finding the band structure is to consider the propagation of waves of some frequency ω through the unit cell, taking into account the phase picked up by propagation along the cables and the scattering at the two T-connectors. We represent this propagation with a 4×4 scattering matrix connecting the in- and out-going modes to the unit cell. We then impose periodic boundary conditions to include the lattice. This leads to the dispersion $\omega(k_x, k_y)$.

We begin by deriving the scattering matrix for a single T-connector. We focus on the left-hand connector in the unit cell, but the same result applies to both. We can define the 3×3 scattering matrix S connecting the in- and out-going modes to/from the connector (I_i and O_i respectively) as:

$$\begin{pmatrix} I_1 \\ I_2 \\ I_3 \end{pmatrix} = S \begin{pmatrix} O_1 \\ O_2 \\ O_3 \end{pmatrix} \equiv \begin{pmatrix} r_1 & t_{12} & t_{13} \\ t_{21} & r_2 & t_{23} \\ t_{31} & t_{32} & r_3 \end{pmatrix} \begin{pmatrix} O_1 \\ O_2 \\ O_3 \end{pmatrix} \tag{4.10}$$

where S is unitary as we have no loss, and r_i and t_{ij} are the reflection and transmission coefficients respectively (t_{ij} is the transmission coefficient from cable j to i). The numbering convention for the different modes is shown in Fig. 4.4. We can now calculate these coefficients explicitly. Consider cables 2 and 3 as a load on cable 1, and write the total impedance of 2 and 3, Z_{23}, as:

$$\frac{1}{Z_{23}} = \frac{1}{Z} + \frac{1}{Z}, \tag{4.11}$$

giving $Z_{23} = Z/2$. Via the transmission line equations derived above, we can write the general solution for the current and voltage in cable 1 as:

$$V_1(x,t) = f(x - vt) + g(x + vt), \; I_1(x,t) = \frac{1}{Z}(f(x - vt) - g(x + vt)). \tag{4.12}$$

Taking, without loss of generality, $x = 0$ to be the location of the connector, we can write:

$$r_1 = \frac{g(vt)}{f(-vt)}, \tag{4.13}$$

and:

$$Z_{23} = \frac{f(-vt) + g(vt)}{\frac{1}{Z}(f(-vt) - g(vt))}. \tag{4.14}$$

These two relations then lead to:

$$r_1 = -\frac{1}{3}. \tag{4.15}$$

By symmetry, we have $r_1 = r_2 = r_3$. Choosing, without loss of generality, the transmission coefficients to be real, we also have $t_{ij} = t_{ji} \equiv t$, where all transmission coefficients are equal by symmetry. Since S must be unitary for the zero-loss case, we find $r_1^2 + 2t^2 = 1$, leading to $t = 2/3$. We therefore find the scattering matrix:

$$S = \frac{1}{3}\begin{pmatrix} -1 & 2 & 2 \\ 2 & -1 & 2 \\ 2 & 2 & -1 \end{pmatrix}. \tag{4.16}$$

We can check that $S^{-1} = S^\dagger$, so S is unitary as we expect. We also see that S is Hermitian.

We now write down the following equations describing wave propagation at frequency ω between the left- and right-hand sides of the unit cell. The naming conventions for the modes are shown in Fig. 4.4, and we denote the in- and out-going modes for a given connector by I and O respectively, as we did above. For the left-hand T-connector, we have:

$$\begin{pmatrix} I_1 \\ O_1 \end{pmatrix} = U_{l/2}\begin{pmatrix} I_{0x} \\ O_{0x} \end{pmatrix} \equiv \begin{pmatrix} e^{i\frac{\omega}{c}\frac{l}{2}} & 0 \\ 0 & e^{-i\frac{\omega}{c}\frac{l}{2}} \end{pmatrix}\begin{pmatrix} I_{0x} \\ O_{0x} \end{pmatrix}, \tag{4.17}$$

and:

$$\begin{pmatrix} I_2 \\ O_2 \end{pmatrix} = U_{l/2}\begin{pmatrix} I_{0y} \\ O_{0y} \end{pmatrix} \tag{4.18}$$

describing the propagation of the modes at the left-hand edges towards the connector. These modes then scatter at the connector, which is described by the scattering matrix we derived previously, with:

$$\begin{pmatrix} I_1 \\ I_2 \\ I_3 \end{pmatrix} = S \begin{pmatrix} O_1 \\ O_2 \\ O_3 \end{pmatrix}. \tag{4.19}$$

We then describe the propagation of the modes along the central cable:

$$\begin{pmatrix} I_{1'} \\ O_{1'} \end{pmatrix} = U_l \begin{pmatrix} O_3 \\ I_3 \end{pmatrix}. \tag{4.20}$$

We also have the same scattering matrix for the right-hand connector:

$$\begin{pmatrix} I_{1'} \\ I_{2'} \\ I_{3'} \end{pmatrix} = S \begin{pmatrix} O_{1'} \\ O_{2'} \\ O_{3'} \end{pmatrix}, \tag{4.21}$$

and, finally, we relate the modes at the right-hand unit cell edge to these scattered modes:

$$\begin{pmatrix} I_{1y} \\ O_{1y} \end{pmatrix} = U_{l/2}^{-1} \begin{pmatrix} I_{2'} \\ O_{2'} \end{pmatrix} \tag{4.22}$$

and:

$$\begin{pmatrix} I_{1x} \\ O_{1x} \end{pmatrix} = U_{l/2}^{-1} \begin{pmatrix} I_{3'} \\ O_{3'} \end{pmatrix}. \tag{4.23}$$

We now need to use these various results to derive a 4×4 scattering matrix Σ for the whole unit cell:

$$\begin{pmatrix} I_{0x} \\ I_{0y} \\ I_{1x} \\ I_{1y} \end{pmatrix} = \Sigma \begin{pmatrix} O_{0x} \\ O_{0y} \\ O_{1x} \\ O_{1y} \end{pmatrix}. \tag{4.24}$$

We first define, for symmetry reasons, the modes at the mid-point of the central cable as:

$$\begin{pmatrix} I_M \\ O_M \end{pmatrix} \equiv U_{l/2}^{-1} \begin{pmatrix} I_3 \\ O_3 \end{pmatrix}. \tag{4.25}$$

We hence eliminate the 1, 2 and 3 modes in Eq. 4.19 to arrive at:

$$\begin{pmatrix} I_{0x} \\ I_{0y} \\ I_M \end{pmatrix} = e^{-i\frac{\omega}{c}l} S \begin{pmatrix} O_{0x} \\ O_{0y} \\ O_M \end{pmatrix}. \tag{4.26}$$

We next do a similar calculation for the right-hand connector to get:

$$\begin{pmatrix} O_M \\ I_{1y} \\ I_{1x} \end{pmatrix} = e^{-i\frac{\omega}{c}l} S \begin{pmatrix} I_M \\ O_{1y} \\ O_{1x} \end{pmatrix}. \tag{4.27}$$

We next do a lengthy but straightforward calculation to eliminate the M-modes from these last two equations, which leads directly to the scattering matrix Σ:

$$\Sigma = \begin{pmatrix} \Sigma_1 & \Sigma_2 & \Sigma_3 & \Sigma_3 \\ \Sigma_2 & \Sigma_1 & \Sigma_3 & \Sigma_3 \\ \Sigma_3 & \Sigma_3 & \Sigma_1 & \Sigma_2 \\ \Sigma_3 & \Sigma_3 & \Sigma_2 & \Sigma_1 \end{pmatrix}, \tag{4.28}$$

with:

$$\Sigma_3 \equiv \frac{4}{3} \frac{e^{-i\frac{\omega}{c}l}}{3e^{i\frac{\omega}{c}l} - \frac{1}{3}e^{-i\frac{\omega}{c}l}}, \tag{4.29}$$

and $\Sigma_1 \equiv (1/3)e^{-i\frac{\omega}{c}l}(-1-\Sigma_3)$ and $\Sigma_2 \equiv (1/3)e^{-i\frac{\omega}{c}l}(2-\Sigma_3)$.

Now that we have described the propagation of waves in a single unit cell, we impose

the periodic boundary conditions:

$$\begin{pmatrix} I_{1x} \\ O_{1x} \end{pmatrix} = e^{2ik_x l} \begin{pmatrix} O_{0x} \\ I_{0x} \end{pmatrix}, \tag{4.30}$$

and:

$$\begin{pmatrix} I_{1y} \\ O_{1y} \end{pmatrix} = e^{i(k_x+k_y)l} \begin{pmatrix} O_{0y} \\ I_{0y} \end{pmatrix}, \tag{4.31}$$

where we introduce the Bloch momenta k_x and k_y. We use these to eliminate the '1' modes in Eq. 4.24 (i.e. the right-hand side of the unit cell) to arrive at:

$$\begin{pmatrix} I_{0x} \\ I_{0y} \\ O_{0x} \\ O_{0y} \end{pmatrix} = P_{BC}^{-1} \Sigma P_{BC} \begin{pmatrix} 0 & \mathbb{1}_2 \\ \mathbb{1}_2 & 0 \end{pmatrix} \begin{pmatrix} I_{0x} \\ I_{0y} \\ O_{0x} \\ O_{0y} \end{pmatrix}, \tag{4.32}$$

where we define:

$$P_{BC} \equiv \begin{pmatrix} 1 & 0 & 0 & 0 \\ 0 & 1 & 0 & 0 \\ 0 & 0 & e^{2ik_x l} & 0 \\ 0 & 0 & 0 & e^{i(k_x+k_y)l} \end{pmatrix} \tag{4.33}$$

and where $\mathbb{1}_2$ is the 2×2 identity matrix. We can then demand non-trivial solutions to this equation with the condition:

$$\det \left(P_{BC}^{-1} \Sigma P_{BC} \begin{pmatrix} 0 & \mathbb{1}_2 \\ \mathbb{1}_2 & 0 \end{pmatrix} - \mathbb{1}_4 \right) = 0, \tag{4.34}$$

where $\mathbb{1}_4$ is the 4×4 identity matrix. We can now use the block matrix structure of Σ to

simplify the expression for the determinant in Eq. 4.34. In particular, we write:

$$\Sigma = \begin{pmatrix} A & B \\ B & A \end{pmatrix}, \tag{4.35}$$

where:

$$A = \begin{pmatrix} \Sigma_1 & \Sigma_2 \\ \Sigma_2 & \Sigma_1 \end{pmatrix}, B = \begin{pmatrix} \Sigma_3 & \Sigma_3 \\ \Sigma_3 & \Sigma_3 \end{pmatrix}. \tag{4.36}$$

We can then find that:

$$P_{BC}^{-1} \Sigma P_{BC} \begin{pmatrix} 0 & \mathbb{1}_2 \\ \mathbb{1}_2 & 0 \end{pmatrix} - \mathbb{1}_4 = \begin{pmatrix} BU - \mathbb{1}_2 & A \\ U^{-1}AU & U^{-1}B - \mathbb{1}_2 \end{pmatrix}, \tag{4.37}$$

where we define:

$$U = \begin{pmatrix} e^{2ik_x l} & 0 \\ 0 & e^{i(k_x + k_y)l} \end{pmatrix} \tag{4.38}$$

We can then use an identity to write that:

$$\det \begin{pmatrix} BU - \mathbb{1}_2 & A \\ U^{-1}AU & U^{-1}B - \mathbb{1}_2 \end{pmatrix} = \det(BU - \mathbb{1}_2) \det(U^{-1}B - \mathbb{1}_2 - U^{-1}AU(BU - \mathbb{1}_2)^{-1}A), \tag{4.39}$$

provided that neither $BU - \mathbb{1}_2$ nor $U^{-1}B - \mathbb{1}_2$ are singular, which we can check is not generally true. Requiring that this determinant vanishes then produces the equation:

$$\left(\Sigma_3 - u_1 - \Gamma + \frac{u_1\Sigma_1^2 + u_2\Sigma_2^2}{\Delta}\right)\left(\Sigma_3 - u_2 - \Gamma + \frac{u_2\Sigma_1^2 + u_1\Sigma_2^2}{\Delta}\right) - \left(\Sigma_3 + \Gamma + \frac{(u_1 + u_2)\Sigma_1\Sigma_2}{\Delta}\right)^2 = 0, \tag{4.40}$$

where, for convenience, we introduce the variables $u_1 \equiv e^{2ik_x l}$ and $u_2 \equiv e^{i(k_x + k_y)l}$, and where $\Delta \equiv 1 - \Sigma_3(u_1 + u_2)$ and $\Gamma \equiv \frac{\Sigma_3 u_1 u_2}{\Delta}(\Sigma_1 - \Sigma_2)^2$. This equation can be solved using

a symbolic algebra package to obtain $\omega(k_x, k_y)$. From now on, we set $l = c = 1$.

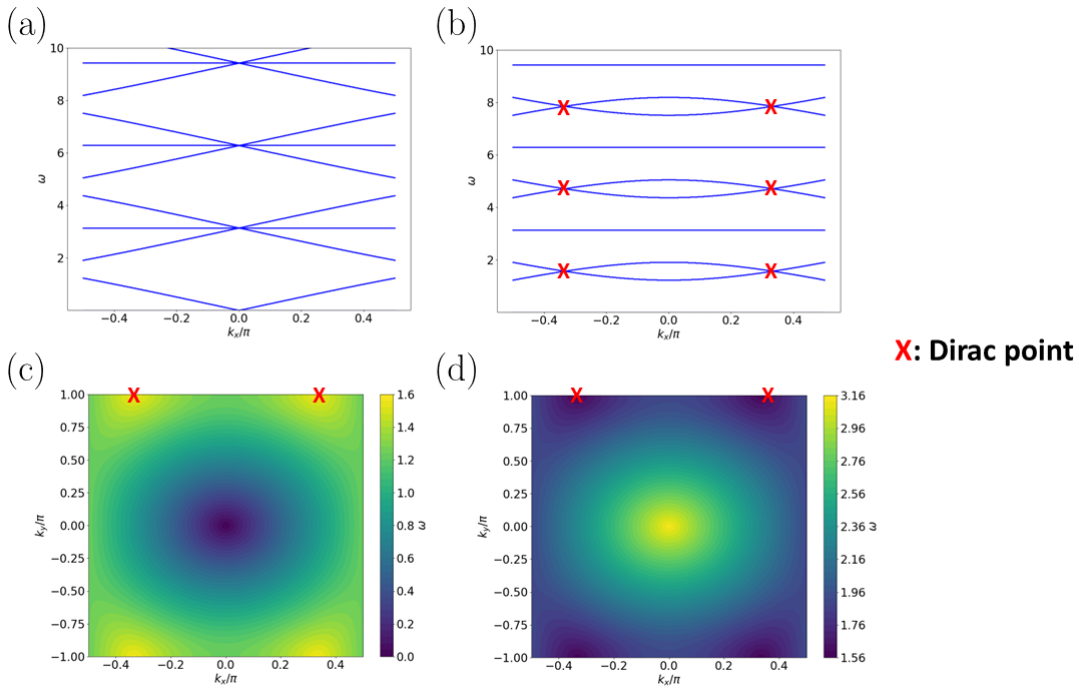

Figure 4.5: Band structure for the brick wall lattice with all cables identical. (a) and (b): Cuts of the bands at $k_y = 0$ and $k_y = \pi$ respectively, showing the flat bands at $\omega = n\pi$ $(n = 0, 1, 2, ...)$ and the two repeated dispersive bands. The dispersive bands meet at gapless Dirac points (red) with momenta $(\pm\pi/3, \pi)$. (c) and (d): Contour plots of the two dispersive bands in the interval $[0, \pi]$, with free-photon-like cone dispersions close to the origin and two gapless Dirac points (red) at the Brillouin zone boundary.

Solving for ω leads to three principal bands in the interval $\omega_{PV} \in [0, \pi]$. We have a flat band with $\omega = \pi$, and two dispersive bands beneath. This set of three is then repeated periodically in ω as $\omega = \omega_{PV} + n\pi$, for $n = 0, 1, 2, ...$ The resultant bands are plotted in Fig. 4.5. We find that the dispersive bands are given explicitly by:

$$\cos(2\omega) = \frac{1}{9}(-3 + 4(\cos(2k_x) + 2\cos(k_x)\cos(k_y))), \tag{4.41}$$

and these are plotted as contour plots in Fig. 4.5(c) and (d). (a) and (b) show cuts of these bands, as well as the $\omega = n\pi$ flat bands, through $k_y = 0$ and $k_y = \pi$ respectively. Due to the properties of cosine, the two principal dispersive bands are mirror images of each other in the plane $\omega = \pi/2$. We see that the lower dispersive band has a conical

dispersion close to the origin, before rolling over to touch the upper dispersive band at two gapless Dirac points at the Brillouin zone boundary, with coordinates $(\pm\pi/3, \pi)$. The cone of the upper dispersive band touches the flat band at the origin. Due to the conical shape of the dispersion close to the origin, we can think of the lattice as being in the nearly-free limit.

4.3 Controlling the Dirac Points by Detuning the Central Cable Impedance

Now that we have characterised the simplest case of the brick wall lattice, with identical cables, we now show how to control the properties of the Dirac points we found. In particular, we consider detuning the impedance of the central cable running between the two T-connectors in each unit cell (highlighted in light blue in Fig. 4.4). Our general approach is the same as in the uniform case. We start by finding the scattering matrix for the left-hand connector using identical arguments to the previous section, but now including the modified impedance and hence different reflection and transmission in that cable. We find:

$$S = \begin{pmatrix} r & t' & t \\ t' & r & t \\ t & t & r' \end{pmatrix}, \tag{4.42}$$

where:

$$r = -\frac{1}{1+2\zeta}, \tag{4.43}$$

$$r' = \frac{1-2\zeta}{1+2\zeta}, \tag{4.44}$$

$$t^2 = \frac{1}{2}(1-r'^2), \tag{4.45}$$

$$t'^2 = 1 - r^2 - t^2, \tag{4.46}$$

where $\zeta \equiv Z_2/Z_1$ is the ratio of impedances, with the central cable now having impedance Z_2, and the other cables have impedance Z_1. We then have:

$$\begin{pmatrix} I_1 \\ I_2 \\ I_3 \end{pmatrix} = S \begin{pmatrix} O_1 \\ O_2 \\ O_3 \end{pmatrix}, \tag{4.47}$$

and:

$$\begin{pmatrix} I_{3'} \\ I_{2'} \\ I_{1'} \end{pmatrix} = S \begin{pmatrix} O_{3'} \\ O_{2'} \\ O_{1'} \end{pmatrix}. \tag{4.48}$$

All other equations from the first section describing the phases acquired as the waves move through the unit cell are identical. Similarly to before, equations 4.47 and 4.48 lead to:

$$\begin{pmatrix} I_{0x} \\ I_{0y} \\ I_M \end{pmatrix} = e^{-i\frac{\omega}{c}l} S \begin{pmatrix} O_{0x} \\ O_{0y} \\ O_M \end{pmatrix}, \tag{4.49}$$

for the left-hand connector, and:

$$\begin{pmatrix} I_{1x} \\ I_{1y} \\ O_M \end{pmatrix} = e^{-i\frac{\omega}{c}l} S \begin{pmatrix} O_{1x} \\ O_{1y} \\ I_M \end{pmatrix}, \tag{4.50}$$

for the right-hand connector. Similarly to the uniform case, we now eliminate the M-modes to calculate the 4×4 scattering matrix for the whole unit cell, defined identically

to the uniform case. This leads to:

$$\Sigma = \begin{pmatrix} \Sigma_1 & \Sigma_2 & \Sigma_3 & \Sigma_3 \\ \Sigma_2 & \Sigma_1 & \Sigma_3 & \Sigma_3 \\ \Sigma_3 & \Sigma_3 & \Sigma_1 & \Sigma_2 \\ \Sigma_3 & \Sigma_3 & \Sigma_2 & \Sigma_1 \end{pmatrix}, \tag{4.51}$$

with:

$$\Sigma_1 = rz + \frac{r't^2z^3}{1 - r'^2z^2}, \tag{4.52}$$

$$\Sigma_2 = t'z + \frac{r't^2z^3}{1 - r'^2z^2}, \tag{4.53}$$

$$\Sigma_3 = \frac{t^2z^2}{1 - r'^2z^2}, \tag{4.54}$$

where we now define $z = \exp(-i\omega l/c)$.

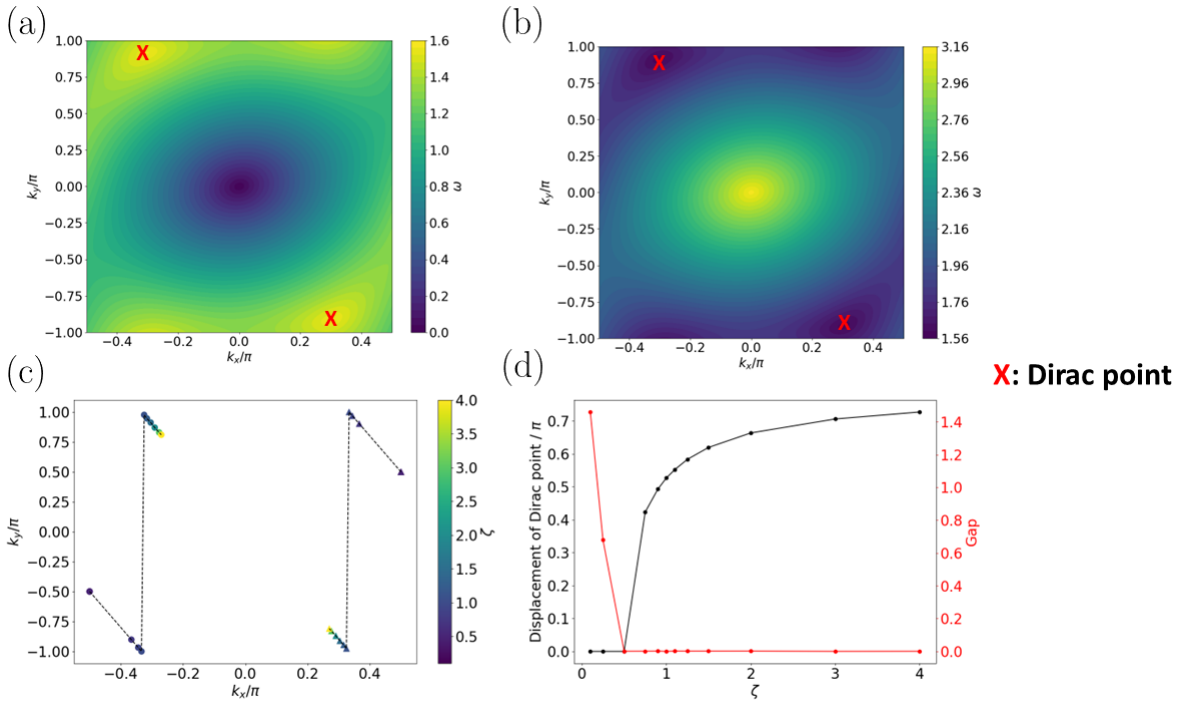

Figure 4.6: Results for the brick wall lattice with the central cable impedance detuned in each unit cell. (a) and (b): contour plots of the two dispersive bands for the case where $\zeta = 1.5$, with free-photon-like cone dispersions close to the origin and the two Dirac points (red) displaced by the detuning. The flat bands still exist at the same frequency as the uniform case and remain gapless at the origin. (c): trajectories taken by the two Dirac points (circles and triangles) around the Brillouin zone as ζ is varied. The dashed line is a guide to the eye. As $\zeta \to 0$, the Dirac points become fixed at $(\pm\pi/2, \pm\pi/2)$. (d): The size of the displacement from $(\pm\pi/2, \pm\pi/2)$ of the Dirac points as ζ varies (black curve, left axis). Also shown is the gap between the Dirac points as a function of ζ (red curve, right axis), showing a gap opening as $\zeta \to 0$.

We see that the scattering matrix has an identical structure to that in the previous section (Eq. 4.28), but with Σ_1, Σ_2 and Σ_3 now dependent on ζ. We also impose the same periodic boundary conditions to those in the previous section. We therefore solve the same equation (Eq. 4.40), but now as a function of ζ. An example set of results for $\zeta = 1.5$ is shown in Fig. 4.6(a) and (b). Generally, we find that $\zeta \neq 1$ moves the two Dirac points around the Brillouin zone, with the points becoming fixed at $(\pm\pi/2, \pm\pi/2)$ as $\zeta \to 0$, and that a gap opens between the Dirac points as $\zeta \to 0$. The band-crossing point between the second and third band at the origin remains gapless. The displacement of the Dirac points suggests connections to the theory of artificial magnetic fields in strained graphene

to this system [148], in which a strain applied the the honeycomb lattice displaces the Dirac points in the Brillouin zone, meaning that Dirac electrons experience an artificial gauge field whose strength relates to the size of the strain. We therefore plot the trajectory and magnitude of the displacement of the Dirac points, as well as the band gap at the Dirac points, in Fig. 4.6 (c) and (d).

4.4 Introducing Isolated Flat Bands by Detuning the Central Cable Length

We now show that we can gain even more control over the features of the bands by tuning the central cable length, rather than the impedance. The equation that we need to solve (discussed below) likely cannot be solved analytically for arbitrary values of the lengths. We therefore consider a particular case, and solve the equation analytically to demonstrate the crucial result that the band structure now includes a family of isolated flat bands, suggesting that the future study of nonlinearities in the system should be of interest.

The basic method is the same as in the prior two calculations, in that we derive equations describing the propagation of waves through the unit cell, which leads to a 4×4 scattering matrix. This scattering matrix will turn out to have the same block matrix structure as the other cases, but with different functional forms for the matrix elements. The following steps are therefore identical to the uniform case; we apply periodic boundary conditions and produce an equation to solve to find $\omega(k_x, k_y)$. More precisely, we consider the usual unit cell shown in Fig. 4.4, with the blue central cables having a length l_2, and the other cables having length l_1. We write down the following equations describing the propagation of the modes:

$$\begin{pmatrix} I_1 \\ O_1 \end{pmatrix} = U_{l_1/2} \begin{pmatrix} I_{0x} \\ O_{0x} \end{pmatrix} \equiv \begin{pmatrix} e^{i\frac{\omega}{c}\frac{l_1}{2}} & 0 \\ 0 & e^{-i\frac{\omega}{c}\frac{l_1}{2}} \end{pmatrix} \begin{pmatrix} I_{0x} \\ O_{0x} \end{pmatrix}, \tag{4.55}$$

and:

$$\begin{pmatrix} I_2 \\ O_2 \end{pmatrix} = U_{l_1/2} \begin{pmatrix} I_{0y} \\ O_{0y} \end{pmatrix} \tag{4.56}$$

describing the propagation of the modes at the left-hand edges towards the connector. These modes then scatter at the connector, which is described by the scattering matrix we derived in the uniform case (Eq. 4.16), with:

$$\begin{pmatrix} I_1 \\ I_2 \\ I_3 \end{pmatrix} = S \begin{pmatrix} O_1 \\ O_2 \\ O_3 \end{pmatrix}. \tag{4.57}$$

We then describe the propagation of the modes along the central cable:

$$\begin{pmatrix} I_{1'} \\ O_{1'} \end{pmatrix} = U_{l_2} \begin{pmatrix} O_3 \\ I_3 \end{pmatrix}. \tag{4.58}$$

We also have the same scattering matrix for the right-hand connector:

$$\begin{pmatrix} I_{1'} \\ I_{2'} \\ I_{3'} \end{pmatrix} = S \begin{pmatrix} O_{1'} \\ O_{2'} \\ O_{3'} \end{pmatrix}, \tag{4.59}$$

and, finally, we relate the modes at the right-hand unit cell edge to these scattered modes:

$$\begin{pmatrix} I_{1y} \\ O_{1y} \end{pmatrix} = U^{-1}_{l_1/2} \begin{pmatrix} I_{2'} \\ O_{2'} \end{pmatrix} \tag{4.60}$$

and:

$$\begin{pmatrix} I_{1x} \\ O_{1x} \end{pmatrix} = U^{-1}_{l_1/2} \begin{pmatrix} I_{3'} \\ O_{3'} \end{pmatrix}. \tag{4.61}$$

We have essentially the same results as in the uniform case, but with different phase

factors that depend on the different cable lengths. Following the same procedure as the uniform case produces the 4×4 scattering matrix, defined by:

$$\begin{pmatrix} I_{0x} \\ I_{0y} \\ I_{1x} \\ I_{1y} \end{pmatrix} = \Sigma \begin{pmatrix} O_{0x} \\ O_{0y} \\ O_{1x} \\ O_{1y} \end{pmatrix}. \tag{4.62}$$

In our case, we find:

$$\Sigma = \begin{pmatrix} \Sigma_1 & \Sigma_2 & \Sigma_3 & \Sigma_3 \\ \Sigma_2 & \Sigma_1 & \Sigma_3 & \Sigma_3 \\ \Sigma_3 & \Sigma_3 & \Sigma_1 & \Sigma_2 \\ \Sigma_3 & \Sigma_3 & \Sigma_2 & \Sigma_1 \end{pmatrix}, \tag{4.63}$$

where:

$$\Sigma_3 \equiv \frac{4}{3} \frac{z^\lambda}{\frac{3}{z} - \frac{z}{3}}, \tag{4.64}$$

where we define $z \equiv \exp(-i\omega l_2)$ (setting $c = 1$ from now on), $\lambda \equiv l_1/l_2$, and $\Sigma_1 \equiv (1/3)(-z^\lambda - z\Sigma_3)$ and $\Sigma_2 \equiv (1/3)(2z^\lambda - z\Sigma_3)$. As mentioned above, the scattering matrix has the same structure as in the uniform case, but with different matrix elements.

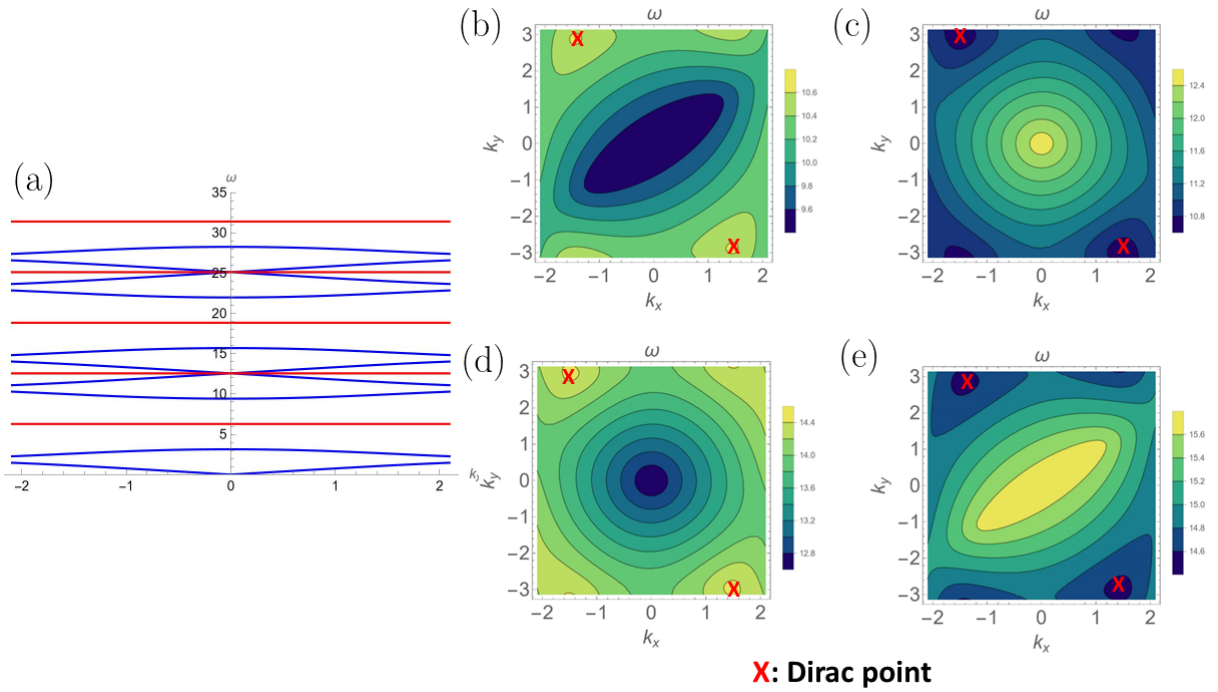

Figure 4.7: (a): Cut of the $\lambda = 2$ length-detuned brick wall lattice dispersion through $k_y = 0$, showing the first few periods of the bands. We see a family of dispersive bands that is periodic in ω (blue) and a family of flat bands interleaved with these (red). A subset of these flat bands are energetically isolated ($\omega = 2\pi, 6\pi, 10\pi, ...$, i.e. odd multiples of 2π), which can be seen by checking the whole band structure. (b) - (e): Contour plots of the four dispersive bands. More precisely, here we show the four bands in the $n = 1$ sector, with $\omega = \omega_{PV} + 4\pi n$. The panels are ordered in increasing ω, so panel (a) corresponds to the bottom $n = 1$ band, etc. Dirac points are marked with a red cross.

The equation we have to solve is therefore the same also (Eq. 4.40) but where, now, our boundary condition phase variables are $u_1 \equiv e^{ik_x(l_1+l_2)}$ and $u_2 \equiv e^{i(k_x l_2 + k_y l_1)}$. The equation likely cannot be solved analytically for arbitrary $\lambda \in (0, \infty)$, so we focus on the simplest non-trivial case (i.e. $\lambda \neq 1$), namely $\lambda = 2$, corresponding physically to the central cable having half the length of the others. We choose units such that $c = 1$ and $l_1 = 1$ and $l_2 = 1/2$. We solve this equation using a symbolic algebra package to find that we still have flat band solutions, now with $e^{-i\omega/2} = \pm 1$, and some dispersive bands whose dispersion is given by the equation:

$$9\cos(2\omega) + 8\cos(\omega) - 8\cos\left(\frac{\omega}{2}\right)\left(\cos\left(\frac{3k_x}{2}\right) + \cos\left(\frac{k_x}{2} + k_y\right)\right) + 3 - 4\cos(k_x - k_y) = 0. \tag{4.65}$$

The first equation yields flat bands for $\omega = 2\pi n$ for $n = 1, 2, 3, ...$, and the second equation can be solved via a symbolic algebra package to produce four distinct dispersive bands in the interval $\omega_{PV} \in [-\pi, \pi]$, which are then repeated as $\omega = \omega_{PV} + 4\pi n$, with $n = 0, 1, 2, ...$ The overall interleaved structure of the bands is shown in the cut in Fig. 4.7(a), and Fig. 4.7(b) - (e) shows the structure of the dispersive bands in detail. From Fig. 4.7, we can see that a subset of the flat band family are energetically isolated from the other bands (this can be checked properly by examination of the band structure over the entire Brillouin zone). Specifically, these are the bands $\omega = 2\pi, 6\pi, 10\pi, ...$, i.e. odd multiples of 2π. We also note that we still seem to find Dirac point features within each set of dispersive bands (red crosses), with bands 1 and 2 touching, as well as bands 3 and 4, within a given set of four.

In this final thesis chapter, we motivated the idea of using lattices of commercially-available coaxial cables and connector elements to engineer lattice models. We then introduced the relevant theory of wave propagation in coaxial cables before calculating the band structure for a brick wall lattice of cables and T-connectors, using a general method that does not depend on having access to a Hamiltonian. We showed that we find one gapless flat band, and two dispersive bands that touch at two Dirac points. This set of three principal bands is then repeated periodically in frequency. The dispersive bands demonstrate that the lattice is in the nearly-free limit, because the bands have a conical dispersion close to the Brillouin zone origin. We then showed that we can control some of these features by modification of the cable impedances and lengths. In particular, we can gap the Dirac points and move them around the Brillouin zone, which suggests connections to the theory of artificial magnetic fields in strained graphene. We can also isolate an infinite family of flat bands, which suggests exciting prospects when nonlinearities are introduced.

In the short term, the natural next steps are to more deeply understand some of the results presented here, particularly by connecting the brick wall lattice symmetries to the existence of gapless band-crossing points, which may give more insight into how to control

them [149]. A natural longer-term goal would be to introduce effective interactions into the system by the inclusion of nonlinear circuit elements. An isolated flat band would lead to the interaction effects dominating, making this a natural avenue to explore. Otherwise, the physics of the artificial magnetic field could be investigated further, perhaps with a view to engineering topological models which break time reversal symmetry. This could be extended further by the inclusion of gain elements into the circuit, which could lead to topological lasing [20, 21].

CHAPTER 5

CONCLUSIONS

In this thesis, we presented three different works in the field of quantum simulation. In the first of these, discussed in Chapter 2, we experimentally demonstrated the realisation of a synthetic dimension formed from the energy eigenstates of a harmonic trap, and characterised the system using the well-known phenomenon of Bloch oscillations. In the second work, discussed in Chapter 3, we presented an experimental proposal for using the paraxial propagation of an optical pulse in a 1D array of waveguides to engineer novel optical effects, which we interpreted in terms of the quantum Hall effect. The physics here could also be thought of in terms of synthetic dimensions, with the time experienced by the pulse in a particular reference frame playing the role of a continuous spatial dimension. Finally, in Chapter 4, we proposed using lattices formed from commercially-available coaxial cables as a quantum simulator. We considered a simple but non-trivial 2D lattice, and demonstrated that the dispersion of Bloch waves has interesting features, and we discussed some ways to control these features. Having summarised our results very briefly, we now review them in detail.

In Chapter 2, we experimentally demonstrated for the first time a synthetic dimension formed from the energy eigenstates of a harmonic trap. We first summarised the scheme, in which an ultracold gas is confined in a harmonic trap, which is then driven by a time-periodic external potential. We showed, using the tools of Floquet theory, that,

for a sufficiently high-frequency drive, we could describe the dynamics using a Floquet Hamiltonian with a very simple structure. In particular, we found nearest-neighbour hoppings between the trap states with a near-constant energy, and that the detuning between the trap and driving frequencies played the role of a constant force along the dimension of trap states. This combination of a 1D tight-binding lattice and a constant force immediately suggests that Bloch oscillations up-and-down the ladder of trap states should be accessible. We then demonstrated experimentally that such Bloch oscillations can be observed in the real-space dynamics of the atomic cloud. We took measurements for several values of the detuning, and used a fit to extract the real space oscillation amplitude and frequency. We confirmed that these measured values agreed well with those from both numerical and semiclassical analytical theory. These theoretical results both made use of a conversion formula which we derived to 'translate' between the real space cloud centre-of-mass and width and the centre-of-mass with respect to the synthetic dimension. We then demonstrated additional control over the scheme by instead varying the strength of the driving potential for a fixed detuning. Finally, we extended the data analysis further to 'project' the experimental results into the synthetic dimension to directly probe how many trap states the cloud explores. We found that we realised a very long synthetic dimension of tens of sites.

Now that we have experimentally demonstrated and characterised the shaken harmonic trap synthetic dimension scheme, we can consider concrete physical models to explore, and make some technical improvements to the current implementation. A natural class of model to explore with our scheme is that of 2D quantum Hall systems, in which the motion along the discrete synthetic dimension can be combined with motion along a real spatial dimension to form an effectively 2D system. This can be achieved very naturally in our setup by considering the motion of the cloud along the weak trapping direction. An artificial gauge field for the charge-neutral atoms can then be realised by modulation of the phase of the driving potential with position along the real, weakly-trapped dimension, which translates to a position-dependent hopping phase in the Floquet Hamiltonian.

This can be interpreted as a Peierls phase and associated with a magnetic field threading our effective 2D system. This is an implementation of the quantum Hall coupled wire model. In parallel, there are number of technical improvements to the current scheme that may aid in realising this 2D physics. These include refining the choice of driving potential to engineer out certain features in the current work which complicate the dynamics and the analysis, and modifying the trapping potential to create an upper edge in the synthetic dimension, which will be important for observing genuine 2D effects. Finally, the measurement and data analysis could be extended towards single-site resolution along the synthetic dimension, and methods better-suited to fully understanding the more complicated 2D dynamics. All of these points are being addressed as part of on-going experimental and theoretical work.

The successful realisation of the quantum Hall coupled wire model in this system will be a significant step forward in the field, and would offer several advantages over quantum Hall models in other platforms. It will offer practical improvements, such as not being dependent upon the details of internal atomic states or upon the atomic species used. It would also overcome some limitations of other approaches, such as the relatively short synthetic lattices. In terms of the physics that can be accessed from the quantum Hall system, our setup is well-suited to measuring the quantised Hall conductivity and, particularly excitingly, there is the prospect of accessing 2D correlated states of matter, such as fractional quantum Hall states, owing to the fact that the interactions are expected to decay with the distance along the synthetic dimension.

In Chapter 3, we experimentally proposed using the propagation of an optical pulse through a 1D array of waveguides as a quantum simulator. We began by reviewing the derivation of the well-known wave equation describing the paraxial propagation of a narrow optical pulse in a 1D waveguide array. We showed that, when we map this equation into a chosen reference frame, it had the form of a Schrödinger equation in which the time evolution of a wavefunction is replaced by the propagation of the electric field envelope along the optical axis of the array. The Schrödinger equation describes a particle with a

position-dependent effective mass, that experiences both a scalar on-site potential and a non-trivial magnetic vector potential whose properties can, in principle, be controlled by spatially modulating the array. This result suggests that the essential physics is, again, that of a quantum Hall coupled wire model. We then considered an experimentally-inspired model of a waveguide array fabricated by laser-writing and numerically found the propagation constants for it. By making use of a Doppler shift to transform these into the co-moving frame, we tuned the parameters of the model to make the co-moving frame dispersion have the same key features as the coupled wire model, namely dispersionless bulk Landau levels, with chiral edge modes in the gaps.

Having shown that the co-moving frame dispersion of a 1D array of waveguides can be tuned to include some of the key features of a quantum Hall model, we went on to explore some specific observable effects that may arise from these features. We first considered bulk cyclotron orbits. We performed numerical simulations in which we prepared a Gaussian wavepacket to target a superposition of the bulk Landau levels. Semiclassically, we expect the wavepacket to execute cyclotron orbits with a characteristic cyclotron frequency, which depends on the particle mass and magnetic field. We did indeed observe these orbits in our numerics. We extracted the frequency of the cyclotron orbits via a fit and compared to classical theory, finding good agreement. We then showed that a Hall drift can be introduced along the time-direction by spatial modulation of the refractive index across the array. We also considered two other physical effects. We considered modulating the waveguide refractive index along the optical axis and across the array, and observed in our numerical simulations that the wavepacket was displaced along the discrete direction, despite the modulation being uniform across the waveguides. Within our Schrödinger equation, this modulation corresponds to an electric field along the continuous direction, leading to a perpendicular displacement along the discrete direction. We also considered a travelling refractive index perturbation that is uniform across the array. In the co-moving frame, this also corresponds to a force along the continuous direction, and hence also produces displacement of the wavepacket across the array. In either

case, the wavepacket couples cleanly into a chiral edge mode which then propagates along the end waveguides.

The theoretical work presented in Chapter 3 can be naturally extended to study the interplay between nonlinearity and topology in photonic systems. Interactions at the mean-field level can readily be included by using a nonlinear optical medium, and a particularly exciting possibility in this system is the study of density-dependent gauge fields, which are an important step on the way to simulating fully dynamical gauge fields, of huge significance in both condensed matter and high-energy physics. More precisely, our effective magnetic vector potential depends upon the refractive index of the medium, and, in a Kerr-nonlinear material, this becomes dependent upon the intensity of the light, which corresponds to the density of photons in a quantum picture. Going beyond this, a key feature of our scheme, in contrast to synthetic frequency dimensions for instance, is that a spatially-local nonlinearity will translate into local interactions in our 2D topological model. If the interaction strength could then be scaled up beyond the mean field level, this would be a route towards strongly-correlated photonic states, such as fractional quantum Hall fluids.

Chapter 4 presents the final work in this thesis, in which we proposed using lattices of coaxial cables as a quantum simulator, motivated by the significant advantages of lattices of coplanar waveguides in circuit QED. We considered a relatively simple but non-trivial 2D system, consisting of a brick wall lattice of identical cables, in which the cables form the edges between the lattice sites, which are three-port T-shaped connector elements. We began by finding the dispersion for Bloch waves moving in this lattice by first modelling the wave propagation within a single unit cell, taking into account the phases acquired by propagation through the cables and the scattering at the connector elements. We then imposed periodic boundary conditions and introduced Bloch momenta. By requiring non-trivial solutions to the resultant set of equations, we calculated the dispersion. We found three principal bands; two of these are dispersive and meet at two Dirac points. Close to the origin, the lower dispersive band has a conical shape, indicating that our model has

nearly-free-photon-like properties. The third band is flat, but not isolated, touching the second band at the origin. These three bands are then repeated periodically in frequency.

We moved on to consider a method to control some of the above features of the dispersion. We detuned the impedance of one of the cables in each unit cell from the other cables, and showed that this led to a displacement of the Dirac points around the Brillouin zone, as well as a gap opening between them in a certain limit. This displacement of the Dirac points suggests connections to the theory of strained graphene, in which the Dirac electrons experience an effective magnetic field when strain is applied to a graphene sample. We also showed that instead detuning the length of the central cable leads to a family of energetically-isolated flat bands, together with a rich structure of dispersive bands and Dirac cones which are again displaced relative to the uniform cable case.

This final work is an early venture into a new experimental quantum simulation platform, and as such it has a number of exciting future directions. In the near-term, the variety of results that we already have can be more deeply interpreted in terms of the symmetries of the brick wall lattice, in order to explain the number of bands we find, and the opening and closing of band gaps when the central cable impedance and length are changed. The apparent robustness of the gapless Dirac points may also have a topological origin, which will be interesting to explore.

In the longer term, the controllable features of our Bloch wave dispersions could be exploited to realise specific physical models. For instance, the magnetic physics that is suggested by the controllable Dirac points could be fully exploited by investigating specific physical effects such as topological physics. Such topological models could then be combined with gain circuit elements to investigate topological lasing, in which the edge modes of a 2D topological model are made to lase. The energetically-isolated flat bands that naturally emerge when the cable lengths are detuned could also provide an excellent opportunity to study the effect of nonlinear circuit elements in these coaxial cable systems, as the excitations from the flat bands will have suppressed kinetic energy, leading to the nonlinear effects dominating.

BIBLIOGRAPHY

[1] I. M. Georgescu, S. Ashhab, and F. Nori. "Quantum simulation". In: *Rev. Mod. Phys.* 86 (1 2014), pp. 153–185. URL: https://link.aps.org/doi/10.1103/RevModPhys.86.153.

[2] J. Preskill. "Lecture notes for Physics 219/Computer Science 219 Quantum Computation". In: Online (Accessed 24/02/2023, 2022). URL: http://theory.caltech.edu/~preskill/ph219/index.html#lecture.

[3] F. Schäfer et al. "Tools for quantum simulation with ultracold atoms". In: *Nat Rev Phys* 2 (2020), pp. 411–425. URL: https://doi.org/10.1038/s42254-020-0195-3.

[4] C. Gross and I. Bloch. "Quantum simulations with ultracold atoms in optical lattices". In: *Science* 357.6355 (2017), pp. 995–1001. URL: https://www.science.org/doi/abs/10.1126/science.aal3837.

[5] "The Hubbard model at half a century". In: *Nature Phys* 523 (2013). URL: https://doi.org/10.1038/nphys2759.

[6] E. Altman et al. "Quantum Simulators: Architectures and Opportunities". In: *PRX Quantum* 2 (1 2021), p. 017003. URL: https://link.aps.org/doi/10.1103/PRXQuantum.2.017003.

[7] R. Blatt and C. Roos. "Quantum simulations with trapped ions". In: *Nature Phys* 8 (2012), pp. 277–284. URL: https://doi.org/10.1038/nphys2252.

[8] H. Bernien et al. "Probing many-body dynamics on a 51-atom quantum simulator". In: *Nature* 551 (2017), pp. 579–584. URL: https://doi.org/10.1038/nature24622.

[9] L. D. Carr et al. "Cold and ultracold molecules: science, technology and applications". In: *New Journal of Physics* 11.5 (2009), p. 055049. URL: https://dx.doi.org/10.1088/1367-2630/11/5/055049.

[10] C. Noh and D. G. Angelakis. "Quantum simulations and many-body physics with light". In: *Reports on Progress in Physics* 80.1 (2016), p. 016401. URL: https://dx.doi.org/10.1088/0034-4885/80/1/016401.

[11] L. Clark et al. "Observation of Laughlin states made of light". In: *Nature* 582 (2020), pp. 41–45. URL: https://doi.org/10.1038/s41586-020-2318-5.

[12] I. Carusotto et al. "Photonic materials in circuit quantum electrodynamics". In: *Nat. Phys.* 16 (2020), pp. 268–279. URL: https://www.nature.com/articles/s41567-020-0815-y.

[13] T. Ozawa et al. "Topological photonics". In: *Rev. Mod. Phys.* 91 (1 2019), p. 015006. URL: https://link.aps.org/doi/10.1103/RevModPhys.91.015006.

[14] C. Oliver. "Exploiting Time as a 'Synthetic Spatial Dimension' for Topological Photonics". In: Unpublished Mid-Course Assessment (2019).

[15] K. v. Klitzing, G. Dorda, and M. Pepper. "New Method for High-Accuracy Determination of the Fine-Structure Constant Based on Quantized Hall Resistance". In: *Phys. Rev. Lett.* 45 (6 1980), pp. 494–497. URL: https://link.aps.org/doi/10.1103/PhysRevLett.45.494.

[16] B. Bernevig and T. Hughes. *Topological Insulators and Topological Superconductors*. Princeton, New Jersey: Princeton University Press, 2013.

[17] H. Price and T. Ozawa. "Lecture notes for Introduction to Topological Phases of Matter". In: Online (Accessed 24/02/2023). URL: https://topologicalphases.wordpress.com/course-structure/.

[18] J. Cardy. *Scaling and Renormalization in Statistical Physics*. Cambridge Lecture Notes in Physics. Cambridge University Press, 1996.

[19] T. Ozawa et al. "Synthetic dimensions in integrated photonics: From optical isolation to four-dimensional quantum Hall physics". In: *Phys. Rev. A* 93 (4 2016), p. 043827. URL: https://link.aps.org/doi/10.1103/PhysRevA.93.043827.

[20] G. Harari et al. "Topological insulator laser: Theory". In: *Science* 359.6381 (2018), eaar4003. URL: https://www.science.org/doi/abs/10.1126/science.aar4003.

[21] M. A. Bandres et al. "Topological insulator laser: Experiments". In: *Science* 359.6381 (2018), eaar4005. URL: https://www.science.org/doi/abs/10.1126/science.aar4005.

[22] B. Mendelson. *Introduction to Topology*. New York: Dover Publications, 1990.

[23] S. Girvin. "The Quantum Hall Effect: Novel Excitations and Broken Symmetries". In: *arXiv:cond-mat/9907002* (1999). URL: https://arxiv.org/abs/cond-mat/9907002.

[24] D. Tong. "Lectures on the Quantum Hall Effect". In: *arXiv:1606.06687 [hep-th]* (2016). URL: https://arxiv.org/abs/1606.06687.

[25] J. Schurr et al. "The width of AC quantum Hall plateaus". In: *IEEE Transactions on Instrumentation and Measurement* 53.3 (2004), pp. 826–829. URL: https://ieeexplore.ieee.org/document/1299148.

[26] M. V. Berry. "Quantal Phase Factors Accompanying Adiabatic Changes". In: *Proceedings of the Royal Society of London. Series A, Mathematical and Physical Sciences* 392.1802 (1984), pp. 45–57. URL: http://www.jstor.org/stable/2397741.

[27] S. Pancharatnam. "Generalized theory of interference, and its applications". In: *Proc. Indian Acad. Sci.* 44 (1954), pp. 247–262. URL: https://doi.org/10.1007/BF03046050.

[28] D. J. Thouless et al. "Quantized Hall Conductance in a Two-Dimensional Periodic Potential". In: *Phys. Rev. Lett.* 49 (6 1982), pp. 405–408. URL: https://link.aps.org/doi/10.1103/PhysRevLett.49.405.

[29] N. R. Cooper, J. Dalibard, and I. B. Spielman. "Topological bands for ultracold atoms". In: *Rev. Mod. Phys.* 91 (1 2019), p. 015005. URL: https://link.aps.org/doi/10.1103/RevModPhys.91.015005.

[30] H. Lignier et al. "Dynamical Control of Matter-Wave Tunneling in Periodic Potentials". In: *Phys. Rev. Lett.* 99 (22 2007), p. 220403. URL: https://link.aps.org/doi/10.1103/PhysRevLett.99.220403.

[31] C. Weitenberg and J. Simonet. "Tailoring quantum gases by Floquet engineering". In: *Nat. Phys.* 17 (2021), 1342—1348. URL: https://doi.org/10.1038/s41567-021-01316-x.

[32] A. Celi et al. "Synthetic Gauge Fields in Synthetic Dimensions". In: *Phys. Rev. Lett.* 112 (4 2014), p. 043001. URL: https://link.aps.org/doi/10.1103/PhysRevLett.112.043001.

[33] S.-C. Zhang and J. Hu. "A Four-Dimensional Generalization of the Quantum Hall Effect". In: *Science* 294.5543 (2001), pp. 823–828. URL: https://www.science.org/doi/abs/10.1126/science.294.5543.823.

[34] J. Fröhlich and B. Pedrini. "New applications of the chiral anomaly". In: *Mathematical Physics 2000* (2000), pp. 9–47. URL: https://doi.org/10.1142/9781848160224_0002.

[35] J.-B. Bouhiron et al. "Realization of an atomic quantum Hall system in four dimensions". In: *arXiv:2210.06322 [cond-mat.quant-gas]* (2022). URL: https://arxiv.org/abs/2210.06322.

[36] M. Mancini et al. "Observation of chiral edge states with neutral fermions in synthetic Hall ribbons". In: *Science* 349.6255 (2015), pp. 1510–1513. URL: https://www.science.org/doi/abs/10.1126/science.aaa8736.

[37] B. K. Stuhl et al. "Visualizing edge states with an atomic Bose gas in the quantum Hall regime". In: *Science* 349.6255 (2015), pp. 1514–1518. URL: https://www.science.org/doi/abs/10.1126/science.aaa8515.

[38] B. Gadway. "Atom-optics approach to studying transport phenomena". In: *Phys. Rev. A* 92 (4 2015), p. 043606. URL: https://link.aps.org/doi/10.1103/PhysRevA.92.043606.

[39] E. Meier et al. "Observation of the topological Anderson insulator in disordered atomic wires". In: *Science* 362.6417 (2018), pp. 929–933. URL: https://www.science.org/doi/10.1126/science.aat3406.

[40] E. Meier, F. An, and B. Gadway. "Atom-optics simulator of lattice transport phenomena". In: *Phys. Rev. A* 93 (5 2016), p. 051602. URL: https://link.aps.org/doi/10.1103/PhysRevA.93.051602.

[41] E. Meier, F. An, and B. Gadway. "Observation of the topological soliton state in the Su–Schrieffer–Heeger model". In: *Nat. Commun.* 7 (2016), p. 13986. URL: https://www.nature.com/articles/ncomms13986.

[42] F. An, E. Meier, and B. Gadway. "Direct observation of chiral currents and magnetic reflection in atomic flux lattices". In: *Science Advances* 3.4 (2017), e1602685. URL: https://www.science.org/doi/abs/10.1126/sciadv.1602685.

[43] F. An et al. “Correlated Dynamics in a Synthetic Lattice of Momentum States”. In: *Phys. Rev. Lett.* 120 (4 2018), p. 040407. URL: https://link.aps.org/doi/10.1103/PhysRevLett.120.040407.

[44] H. Price, T. Ozawa, and N. Goldman. “Synthetic dimensions for cold atoms from shaking a harmonic trap”. In: *Phys. Rev. A* 95 (2 2017), p. 023607. URL: https://link.aps.org/doi/10.1103/PhysRevA.95.023607.

[45] G. Salerno et al. “Quantized Hall Conductance of a Single Atomic Wire: A Proposal Based on Synthetic Dimensions”. In: *Phys. Rev. X* 9 (4 2019), p. 041001. URL: https://link.aps.org/doi/10.1103/PhysRevX.9.041001.

[46] C. Oliver et al. “Bloch Oscillations Along a Synthetic Dimension of Atomic Trap States”. In: *arXiv:2112.10648 [cond-mat.quant-gas]* (2021). URL: https://arxiv.org/abs/2112.10648.

[47] B. Sundar, B. Gadway, and K. Hazzard. “Synthetic dimensions in ultracold polar molecules.” In: *Sci. Rep.* 8 (2018), p. 3422. URL: https://www.nature.com/articles/s41598-018-21699-x.

[48] B. Sundar et al. “Strings of ultracold molecules in a synthetic dimension”. In: *Phys. Rev. A* 99 (1 2019), p. 013624. URL: https://link.aps.org/doi/10.1103/PhysRevA.99.013624.

[49] L. F. Livi et al. “Synthetic Dimensions and Spin-Orbit Coupling with an Optical Clock Transition”. In: *Phys. Rev. Lett.* 117 (22 2016), p. 220401. URL: https://link.aps.org/doi/10.1103/PhysRevLett.117.220401.

[50] S. Kolkowitz et al. “Spin–orbit-coupled fermions in an optical lattice clock”. In: *Nature* 542 (2017), pp. 66 –70. URL: https://www.nature.com/articles/nature20811.

[51] T. Chalopin et al. “Probing chiral edge dynamics and bulk topology of a synthetic Hall system.” In: *Nat. Phys.* 16 (2020), 1017–1021. URL: https://www.nature.com/articles/s41567-020-0942-5.

[52] S. K. Kanungo et al. “Realizing topological edge states with Rydberg-atom synthetic dimensions”. In: *Nat Commun* 13.972 (2022). URL: https://doi.org/10.1038/s41467-022-28550-y.

[53] V. Lienhard et al. “Realization of a density-dependent Peierls phase in a synthetic, spin-orbit coupled Rydberg system”. In: *Phys. Rev. X* 10.2 (2020), p. 021031. URL: https://journals.aps.org/prx/abstract/10.1103/PhysRevX.10.021031.

[54] E. Lustig and M. Segev. “Topological photonics in synthetic dimensions”. In: *Advances in Optics and Photonics* 13.2 (2021), pp. 426–461. URL: https://www.nature.com/articles/s41586-019-0943-7/.

[55] L. Yuan et al. “Synthetic dimension in photonics”. In: *Optica* 5.11 (2018), pp. 1396–1405.

[56] Z. Yang et al. “Mode-locked topological insulator laser utilizing synthetic dimensions”. In: *Phys. Rev. X* 10.1 (2020), p. 011059. URL: https://journals.aps.org/prx/abstract/10.1103/PhysRevX.10.011059.

[57] X.-F. Zhou et al. "Dynamically Manipulating Topological Physics and Edge Modes in a Single Degenerate Optical Cavity". In: *Phys. Rev. Lett.* 118 (8 2017), p. 083603. URL: https://link.aps.org/doi/10.1103/PhysRevLett.118.083603.

[58] L. Yuan, Y. Shi, and S. Fan. "Photonic gauge potential in a system with a synthetic frequency dimension". In: *Opt. Lett.* 41.4 (2016), pp. 741–744. URL: https://www.osapublishing.org/ol/abstract.cfm?uri=ol-41-4-741.

[59] L. Yuan and S. Fan. "Bloch oscillation and unidirectional translation of frequency in a dynamically modulated ring resonator". In: *Optica* 3.9 (2016), pp. 1014–1018. URL: https://www.osapublishing.org/optica/abstract.cfm?uri=optica-3-9-1014.

[60] A. Dutt et al. "A single photonic cavity with two independent physical synthetic dimensions". In: *Science* 367.6473 (2020), pp. 59–64. URL: https://www.science.org/doi/10.1126/science.aaz3071.

[61] A. Dutt et al. "Experimental band structure spectroscopy along a synthetic dimension". In: *Nat. commun.* 10.1 (2019), pp. 1–8. URL: https://www.nature.com/articles/s41467-019-11117-9.

[62] E. Lustig et al. "Photonic topological insulator in synthetic dimensions". In: *Nature* 567.7748 (2019), pp. 356–360. URL: https://www.nature.com/articles/s41586-019-0943-7/.

[63] C. Chen et al. "Observation of Topologically Protected Edge States in a Photonic Two-Dimensional Quantum Walk". In: *Phys. Rev. Lett.* 121 (10 2018), p. 100502. URL: https://link.aps.org/doi/10.1103/PhysRevLett.121.100502.

[64] C. Oliver et al. "Artificial gauge fields in the t-z mapping for optical pulses: spatio-temporal wavepacket control and quantum Hall physics". In: *In preparation* (2023).

[65] T. Ozawa and I. Carusotto. "Synthetic Dimensions with Magnetic Fields and Local Interactions in Photonic Lattices". In: *Phys. Rev. Lett.* 118 (1 2017), p. 013601. URL: https://link.aps.org/doi/10.1103/PhysRevLett.118.013601.

[66] N. Goldman and J. Dalibard. "Periodically Driven Quantum Systems: Effective Hamiltonians and Engineered Gauge Fields". In: *Phys. Rev. X* 4 (3 2014), p. 031027. URL: https://link.aps.org/doi/10.1103/PhysRevX.4.031027.

[67] M. S. Rudner and N. H. Lindner. "The Floquet Engineer's Handbook". In: *arXiv:2003.08252 [cond-mat.mes-hall]* (2020). URL: https://arxiv.org/abs/2003.08252.

[68] L. Maczewsky et al. "Observation of photonic anomalous Floquet topological insulators". In: *Nat Commun* 8 (13756 2017). URL: https://doi.org/10.1038/ncomms13756.

[69] P. G. Harper. "Single Band Motion of Conduction Electrons in a Uniform Magnetic Field". In: *Proceedings of the Physical Society. Section A* 68.10 (1955), p. 874. URL: https://dx.doi.org/10.1088/0370-1298/68/10/304.

[70] D. R. Hofstadter. "Energy levels and wave functions of Bloch electrons in rational and irrational magnetic fields". In: *Phys. Rev. B* 14 (6 1976), pp. 2239–2249. URL: https://link.aps.org/doi/10.1103/PhysRevB.14.2239.

[71] F. Bloch. "Über die quantenmechanik der elektronen in kristallgittern". In: *Zeitschrift für physik* 52.7 (1929), pp. 555–600.

[72] M. Ben Dahan et al. "Bloch Oscillations of Atoms in an Optical Potential". In: *Phys. Rev. Lett.* 76 (24 1996), pp. 4508–4511. URL: https://link.aps.org/doi/10.1103/PhysRevLett.76.4508.

[73] A. R. Kolovsky, A. V. Ponomarev, and H. J. Korsch. "Damped Bloch oscillations of cold atoms in optical lattices". In: *Phys. Rev. A* 66 (5 2002), p. 053405. URL: https://link.aps.org/doi/10.1103/PhysRevA.66.053405.

[74] A. R. Kolovsky and H. J. Korsch. "Bloch oscillations of cold atoms in two-dimensional optical lattices". In: *Phys. Rev. A* 67 (6), p. 063601. URL: https://link.aps.org/doi/10.1103/PhysRevA.67.063601.

[75] A. Buchleitner and A. Kolovsky. "Interaction-Induced Decoherence of Atomic Bloch Oscillations". In: *Phys. Rev. Lett.* 91 (25 2003), p. 253002. URL: https://link.aps.org/doi/10.1103/PhysRevLett.91.253002.

[76] D. M. Gangardt and A. Kamenev. "Bloch Oscillations in a One-Dimensional Spinor Gas". In: *Phys. Rev. Lett.* 102 (7 2009), p. 070402. URL: https://link.aps.org/doi/10.1103/PhysRevLett.102.070402.

[77] C. Gaul et al. "Stable Bloch Oscillations of Cold Atoms with Time-Dependent Interaction". In: *Phys. Rev. Lett.* 102 (25 2009), p. 255303. URL: https://link.aps.org/doi/10.1103/PhysRevLett.102.255303.

[78] A. Kolovsky, H. Korsch, and E.-M. Graefe. "Bloch oscillations of Bose-Einstein condensates: Quantum counterpart of dynamical instability". In: *Phys. Rev. A* 80 (2 2009), p. 023617. URL: https://link.aps.org/doi/10.1103/PhysRevA.80.023617.

[79] K. Kudo and T. S. Monteiro. "Theoretical analysis of super–Bloch oscillations". In: *Phys. Rev. A* 83 (5 2011), p. 053627. URL: https://link.aps.org/doi/10.1103/PhysRevA.83.053627.

[80] B. P. Venkatesh and D. H. J. O'Dell. "Bloch oscillations of cold atoms in a cavity: Effects of quantum noise". In: *Phys. Rev. A* 88 (1 2013), p. 013848. URL: https://link.aps.org/doi/10.1103/PhysRevA.88.013848.

[81] Y. Kartashov et al. "Bloch Oscillations in Optical and Zeeman Lattices in the Presence of Spin-Orbit Coupling". In: *Phys. Rev. Lett.* 117 (21 2016), p. 215301. URL: https://link.aps.org/doi/10.1103/PhysRevLett.117.215301.

[82] Z. Geiger et al. "Observation and Uses of Position-Space Bloch Oscillations in an Ultracold Gas". In: *Phys. Rev. Lett.* 120 (21 2018), p. 213201. URL: https://link.aps.org/doi/10.1103/PhysRevLett.120.213201.

[83] J. Höller and A. Alexandradinata. "Topological Bloch oscillations". In: *Phys. Rev. B* 98 (2 2018), p. 024310. URL: https://link.aps.org/doi/10.1103/PhysRevB.98.024310.

[84] W. Ji et al. "Bloch oscillations of spin-orbit-coupled cold atoms in an optical lattice and spin-current generation". In: *Phys. Rev. A* 99 (2 2019), p. 023604. URL: https://link.aps.org/doi/10.1103/PhysRevA.99.023604.

[85] Z. Pagel et al. "Symmetric Bloch oscillations of matter waves". In: *Phys. Rev. A* 102 (5 2020), p. 053312. URL: https://link.aps.org/doi/10.1103/PhysRevA.102.053312.

[86] H. Chen et al. "Real-time observation of frequency Bloch oscillations with fibre loop modulation". In: *Light: Science & Applications* 10.1 (2021), pp. 1–9. URL: https://www.nature.com/articles/s41377-021-00494-w.

[87] C. Bersch, G. Onishchukov, and U. Peschel. "Experimental observation of spectral Bloch oscillations". In: *Opt. Lett.* 34.15 (2009), pp. 2372–2374. URL: https://www.osapublishing.org/ol/abstract.cfm?URI=ol-34-15-2372.

[88] J. Feldmann et al. "Optical investigation of Bloch oscillations in a semiconductor superlattice". In: *Phys. Rev. B* 46 (11 1992), pp. 7252–7255. URL: https://link.aps.org/doi/10.1103/PhysRevB.46.7252.

[89] K. Leo et al. "Observation of Bloch oscillations in a semiconductor superlattice". In: *Solid State Communications* 84.10 (1992), pp. 943–946. URL: https://www.sciencedirect.com/science/article/pii/003810989290798E.

[90] A. Szameit and S. Nolte. "Discrete optics in femtosecond-laser-written photonic structures". In: *Journal of Physics B: Atomic, Molecular and Optical Physics* 43.16 (2010), p. 163001. URL: https://iopscience.iop.org/article/10.1088/0953-4075/43/16/163001.

[91] R. W. Boyd. *Nonlinear Optics*. 4th ed. 2020.

[92] T. Schwartz et al. "Transport and Anderson localization in disordered two-dimensional photonic lattices". In: *Nature* 446 (2007), pp. 52 –55. URL: https://www.nature.com/articles/nature05623.

[93] Y. Lahini et al. "Anderson Localization and Nonlinearity in One-Dimensional Disordered Photonic Lattices". In: *Phys. Rev. Lett.* 100 (1 2008), p. 013906. URL: https://link.aps.org/doi/10.1103/PhysRevLett.100.013906.

[94] B. Freedman et al. "Wave and defect dynamics in nonlinear photonic quasicrystals". In: *Nature* 440 (2006), 1166–1169. URL: https://www.nature.com/articles/nature04722.

[95] L. Levi et al. "Disorder-Enhanced Transport in Photonic Quasicrystals". In: *Science* 332.6037 (2011), pp. 1541–1544. URL: https://www.science.org/doi/abs/10.1126/science.1202977.

[96] M. Verbin et al. "Observation of Topological Phase Transitions in Photonic Quasicrystals". In: *Phys. Rev. Lett.* 110 (7 2013), p. 076403. URL: https://link.aps.org/doi/10.1103/PhysRevLett.110.076403.

[97] M. C. Rechtsman et al. "Strain-induced pseudomagnetic field and photonic Landau levels in dielectric structures". In: *Nature Photon* 7 (2013), 153–158. URL: https://www.nature.com/articles/nphoton.2012.302/.

[98] S. Mukherjee et al. "Experimental Observation of Aharonov-Bohm Cages in Photonic Lattices". In: *Phys. Rev. Lett.* 121 (7 2018), p. 075502. URL: https://link.aps.org/doi/10.1103/PhysRevLett.121.075502.

[99] A. Szameit et al. "$\mathcal{PT}$-symmetry in honeycomb photonic lattices". In: *Phys. Rev. A* 84 (2 2011), p. 021806. URL: https://journals.aps.org/pra/abstract/10.1103/PhysRevA.84.021806.

[100] M. Segev et al. "Spatial solitons in photorefractive media". In: *Phys. Rev. Lett.* 68 (7 1992), pp. 923–926. URL: https://link.aps.org/doi/10.1103/PhysRevLett.68.923.

[101] H. S. Eisenberg et al. "Discrete Spatial Optical Solitons in Waveguide Arrays". In: *Phys. Rev. Lett.* 81 (16 1998), pp. 3383–3386. URL: https://link.aps.org/doi/10.1103/PhysRevLett.81.3383.

[102] N. K. Efremidis et al. "Discrete solitons in photorefractive optically induced photonic lattices". In: *Phys. Rev. E* 66 (4 2002), p. 046602. URL: https://link.aps.org/doi/10.1103/PhysRevE.66.046602.

[103] D. Christodoulides, F. Lederer, and Y. Silberberg. "Discretizing light behaviour in linear and nonlinear waveguide lattices". In: *Nature* 424 (2003), pp. 817 –823. URL: https://www.nature.com/articles/nature01936.

[104] J. W. Fleischer et al. "Observation of two-dimensional discrete solitons in optically induced nonlinear photonic lattices". In: *Nature* 422 (2003), pp. 147 –150. URL: https://www.nature.com/articles/nature01452/.

[105] H. Price et al. "Roadmap on topological photonics". In: *Journal of Physics: Photonics* (2022). URL: https://iopscience.iop.org/article/10.1088/2515-7647/ac4ee4.

[106] M. C. Rechtsman et al. "Photonic Floquet topological insulators". In: *Nature* 496 (2013), 196–200. URL: https://www.nature.com/articles/nature12066.

[107] F. D. M. Haldane. "Model for a Quantum Hall Effect without Landau Levels: Condensed-Matter Realization of the "Parity Anomaly"". In: *Phys. Rev. Lett.* 61 (18 1988), pp. 2015–2018. URL: https://link.aps.org/doi/10.1103/PhysRevLett.61.2015.

[108] Y. Lumer et al. "Self-Localized States in Photonic Topological Insulators". In: *Phys. Rev. Lett.* 111 (24 2013), p. 243905. URL: https://link.aps.org/doi/10.1103/PhysRevLett.111.243905.

[109] S. Mukherjee and M. C. Rechtsman. "Observation of Unidirectional Solitonlike Edge States in Nonlinear Floquet Topological Insulators". In: *Phys. Rev. X* 11 (4 2021), p. 041057. URL: https://link.aps.org/doi/10.1103/PhysRevX.11.041057.

[110] S. Mukherjee and M. C. Rechtsman. "Observation of Floquet solitons in a topological bandgap". In: *Science* 368.6493 (2020), pp. 856–859. URL: https://www.science.org/doi/abs/10.1126/science.aba8725.

[111] J. Noh et al. "Experimental observation of optical Weyl points and Fermi arc-like surface states". In: *Nature Phys* 13 (2017), pp. 611 –617. URL: https://www.nature.com/articles/nphys4072/.

[112] E. Lustig et al. "Three-dimensional photonic topological insulator induced by lattice dislocations". In: *arXiv:2204.13762 [physics.optics]* (2022).

[113] Z. Yang et al. "Photonic Floquet topological insulators in a fractal lattice". In: *Light Sci Appl* 9 (128 2020). URL: https://www.nature.com/articles/s41377-020-00354-z.

[114] Z. Fu et al. "Extended SSH Model in Non-Hermitian Waveguides with Alternating Real and Imaginary Couplings". In: *Applied Sciences* 10.10 (2020). URL: https://www.mdpi.com/2076-3417/10/10/3425.

[115] J. M. Zeuner et al. "Observation of a Topological Transition in the Bulk of a Non-Hermitian System". In: *Phys. Rev. Lett.* 115 (4 2015), p. 040402. URL: https://link.aps.org/doi/10.1103/PhysRevLett.115.040402.

[116] S. Weidemann et al. "Topological funneling of light". In: *Science* 368.6488 (2020), pp. 311–314. URL: https://www.science.org/doi/abs/10.1126/science.aaz8727.

[117] S. Stützer et al. "Photonic topological Anderson insulators". In: *Nature* 560 (2018), pp. 461 –465. URL: https://www.nature.com/articles/s41586-018-0418-2.

[118] Y. E. Kraus et al. "Topological States and Adiabatic Pumping in Quasicrystals". In: *Phys. Rev. Lett.* 109 (10 2012), p. 106402. URL: https://link.aps.org/doi/10.1103/PhysRevLett.109.106402.

[119] O. Zilberberg et al. "Photonic topological boundary pumping as a probe of 4D quantum Hall physics". In: *Nature* 553.7686 (2018), pp. 59–62. URL: https://www.nature.com/articles/nature25011.

[120] M. Wimmer et al. "Experimental measurement of the Berry curvature from anomalous transport". In: *Nature Phys* 13 (2017), pp. 545 –550. URL: https://www.nature.com/articles/nphys4050.

[121] T. Kitagawa et al. "Observation of topologically protected bound states in photonic quantum walks". In: *Nat Commun* 3 (882 2012). URL: https://www.nature.com/articles/ncomms1872.

[122] Q. Fontaine et al. "Observation of the Bogoliubov Dispersion in a Fluid of Light". In: *Phys. Rev. Lett.* 121 (18 2018), p. 183604. URL: https://link.aps.org/doi/10.1103/PhysRevLett.121.183604.

[123] J. Steinhauer et al. "Analogue cosmological particle creation in an ultracold quantum fluid of light". In: *Nat Commun* 13 (2022). URL: https://doi.org/10.1038/s41467-022-30603-1.

[124] A. Blais et al. "Cavity quantum electrodynamics for superconducting electrical circuits: An architecture for quantum computation". In: *Phys. Rev. A* 69 (6 2004), p. 062320. URL: https://link.aps.org/doi/10.1103/PhysRevA.69.062320.

[125] A. Houck, H. Türeci, and J. Koch. "On-chip quantum simulation with superconducting circuits". In: *Nature Physics* 8 (2012). URL: http://www.nature.com/doifinder/10.1038/nphys2251.

[126] S. Girvin. "Circuit QED: Superconducting Qubits Coupled to Microwave Photons". In: *Online, Accessed 02/03/2023* (Accessed 02/03/2023 2011). URL: https://girvin.sites.yale.edu/lectures.

[127] A. Blais, S. Girvin, and W. Oliver. "Quantum information processing and quantum optics with circuit quantum electrodynamics". In: *Nat. Phys.* 16 (2020), pp. 247–256. URL: https://www.nature.com/articles/s41567-020-0806-z/.

[128] A. Kollár, M. Fitzpatrick, and A. Houck. "Hyperbolic lattices in circuit quantum electrodynamics". In: *Nature* 571 (2019), pp. 45–50. URL: https://www.nature.com/articles/s41586-019-1348-3.

[129] A. Kollár et al. "Line-Graph Lattices: Euclidean and Non-Euclidean Flat Bands, and Implementations in Circuit Quantum Electrodynamics". In: *Commun. Math. Phys.* 376 (2020), pp. 1909–1956. URL: https://link.springer.com/article/10.1007/s00220-019-03645-8.

[130] I. Boettcher et al. "Quantum simulation of hyperbolic space with circuit quantum electrodynamics: From graphs to geometry". In: *Phys. Rev. A* 102 (3 2020), p. 032208. URL: https://link.aps.org/doi/10.1103/PhysRevA.102.032208.

[131] P. Bienias et al. "Circuit Quantum Electrodynamics in Hyperbolic Space: From Photon Bound States to Frustrated Spin Models". In: *Phys. Rev. Lett.* 128 (1 2022), p. 013601. URL: https://link.aps.org/doi/10.1103/PhysRevLett.128.013601.

[132] J. Ningyuan et al. "Time- and Site-Resolved Dynamics in a Topological Circuit". In: *Phys. Rev. X* 5 (2 2015), p. 021031. URL: https://link.aps.org/doi/10.1103/PhysRevX.5.021031.

[133] D. L. Bergman, C. Wu, and L. Balents. "Band touching from real-space topology in frustrated hopping models". In: *Phys. Rev. B* 78 (12 2008), p. 125104. URL: https://link.aps.org/doi/10.1103/PhysRevB.78.125104.

[134] D. Leykam, A. Andreanov, and S. Flach. "Artificial flat band systems: from lattice models to experiments". In: *Advances in Physics: X* 3.1 (2018), p. 1473052. URL: https://doi.org/10.1080/23746149.2018.1473052.

[135] C. Lee et al. "Topolectrical Circuits". In: *Commun Phys* 1 (39 2018). URL: https://www.nature.com/articles/s42005-018-0035-2.

[136] W. P. Su, J. R. Schrieffer, and A. J. Heeger. "Solitons in Polyacetylene". In: *Phys. Rev. Lett.* 42 (25 1979), pp. 1698–1701. URL: https://link.aps.org/doi/10.1103/PhysRevLett.42.1698.

[137] H. M. Price. "Four-dimensional topological lattices through connectivity". In: *Phys. Rev. B* 101 (20 2020), p. 205141. URL: https://link.aps.org/doi/10.1103/PhysRevB.101.205141.

[138] R. Yu, Y. X. Zhao, and A. P. Schnyder. "4D spinless topological insulator in a periodic electric circuit". In: *National Science Review* 7.8 (2020), pp. 1288–1295. URL: https://doi.org/10.1093/nsr/nwaa065.

[139] Y. Wang et al. "Circuit implementation of a four-dimensional topological insulator". In: *Nat Commun* 11 (2356 2020). URL: https://doi.org/10.1038/s41467-020-15940-3.

[140] L. Dobrzynski et al. "Giant gaps in photonic band structures". In: *Phys. Rev. B* 57 (16 1998), R9388–R9391. URL: https://link.aps.org/doi/10.1103/PhysRevB.57.R9388.

[141] L. Poirier and A. Haché. "Nonlinear coaxial photonic crystal". In: *Applied Physics Letters* 78.18 (2001), pp. 2626–2628. URL: https://aip.scitation.org/doi/abs/10.1063/1.1367296.

[142] G. Schneider et al. "Defect modes in coaxial photonic crystals". In: *JOURNAL OF APPLIED PHYSICS* 90.6 (2001), pp. 2642–2649. URL: https://aip.scitation.org/doi/10.1063/1.1391220.

[143] A Hache and L Poirier. "Anomalous dispersion and superluminal group velocity in a coaxial photonic crystal: Theory and experiment". In: *PHYSICAL REVIEW E* 65.3, 2B (2002). URL: https://journals.aps.org/pre/abstract/10.1103/PhysRevE.65.036608.

[144] A Hache and A Slimani. "A model coaxial photonic crystal for studying band structures, dispersion, field localization, and superluminal effects". In: *AMERICAN JOURNAL OF PHYSICS* 72.7 (2004), pp. 916–921. URL: https://aapt.scitation.org/doi/10.1119/1.1707016.

[145] A. Balduzzi. "Topoelectric circuits". In: *Bachelors Thesis* (2022).

[146] D. Nabari. "Unidimensional topolectric circuit". In: *Bachelors Thesis* (2022).

[147] I. Grant and W. Phillips. *Electromagnetism*. 2nd ed. Chicester: Wiley, 2004.

[148] M. Vozmediano, M. Katsnelson, and F. Guinea. "Gauge fields in graphene". In: *Physics Reports* 496.4 (2010), pp. 109–148. URL: https://www.sciencedirect.com/science/article/pii/S0370157310001729.

[149] J. Hou and W. Chen. "Hidden symmetry and protection of Dirac points on the honeycomb lattice". In: *Sci Rep* 5.17571 (2015). URL: https://doi.org/10.1038/srep17571.